Investigations in Crack Detection and Monitoring Based on

PPP-BOTDA Distributed Sensing Technology

BY

DEWEI MENG
M.S., Tongji University, Shanghai, China, 2010
B.S., Tongji University, Shanghai, China, 2007

Thesis

Submitted in partial fulfillment of the requirements
for the degree of Doctor of Philosophy in Civil Engineering
in the Graduate College of the
University of Illinois at Chicago, 2016

Chicago, Illinois

Defense Committee:

Farhad Ansari, Chair and Advisor

Michael Stroscio, Electrical and Computer Engineering

Eduard Karpov

Craig Foster

Didem Ozevin

This thesis is dedicated to my father and mother for their endless love to me.

ACKNOWLEDGEMENTS

I would like to thank my advisor Dr. Farhad Ansari for his endless support during my Ph.D. study and research. My research would not be a success without his guidance.

I would like to thank my committee members, Dr. Michael Stroscio, Dr. Eduard Karpov, Dr. Craig Foster and Dr. Didem Ozevin for spending valuable time in reviewing my work.

Thanks my fellows in the lab, Todd Taylor, Saeed, Abraham, Guina Wang, Junfan Yan, Jingnan Yang, Dr.Weifeng Tian and Dr. Zhigang Yin for all the help they provided in my research.

TABLE OF CONTENTS

LIST OF TABLES

LIST OF FIGURES

LIST OF FIGURES (Continued)

LIST OF FIGURES (Continued)

LIST OF ABBREVIATIONS

BFS	Brillouin Frequency Shift
BGS	Brillouin Gain Spectrum
BGSWD	Width Difference of Brillouin Gain Spectrum
BOCDA	Brillouin Optial Correlation Domain Analysis
BOTDA	Brillouin Optical Time Domain Analysis
BOTDR	Brillouin Optical Time Domain Reflector
COD	Crack Opening Displacement
FBG	Fiber Bragg Grating
FEA	Finite Element Analysis
PPP-BOTDA	Pre-pump-pulse Brillouin Optical Time Domain Analysis
RC	Reinforced Concrete
SBS	Stimulated Brillouin Scattering
SHM	Structural Health Monitoring
SMF	Single Mode Fiber
SR	Spatial Resolution

SUMMARY

Report shows that the nation's bridge structures are going through serious aging and deterioration problems. Cracking is a common phenomenon in the structural members experiencing these problems. As a result, structural health monitoring (SHM) based on crack detection and monitoring plays an important role in safety evaluation of the structures. Sensors based on different technologies have been employed in crack detection and monitoring. Compared to point-style sensors, fiber optic distributed sensors have the advantage of performing ubiquitous sensing, which can locate the cracks directly. Brillouin scattering in optical fibers is sensitive to strain and temperature variations. One key factor affecting the performance of a Brillouin distributed sensing system is the spatial resolution (SR). Pre-pump-pulse Brillouin optical time domain analysis (PPP-BOTDA) is developed and capable of distributed strain/temperature sensing with centimeter-level SR.

In this research, the capability of PPP-BOTDA in crack detection and monitoring is studied both theoretically and experimentally. Appearance of a crack in the structural member would create an extra strain distribution in the sensing fiber. The changes in Brillouin gain spectrum (BGS) induced by the extra strain are analyzed by numerical simulation and validated by a plate-crack test. The changes in BGS are characterized by Brillouin frequency shift (BFS) and the width difference of BGS (BGSWD). Overall, results from the test matched with calculation from numerical simulation. It showed that a crack can be successfully detected as a peak from BFS and BGSWD. The development of the crack can be monitored by the amplitude of the peak.

Tests on structural members showed that the SR employed will affect the performance of the sensing system in crack detection. In order to study the capability of PPP-BOTDA sensing system in differentiating neighboring cracks, theoretical analysis was performed and followed by experimental tests for a series of dual-crack cases considering different crack spacing. Based on results from numerical simulation and experimental tests, it is concluded that PPP-BOTDA can differentiate neighboring cracks when the SR employed is smaller than the crack spacing. The conclusion from the dual-crack cases was validated by results from load tests of reinforced concrete (RC) beams.

Based on the theoretical analysis and experimental research, better understanding of the results from the tests is achieved, and general guidance is provided for crack detection and monitoring based on PPP-BOTDA distributed sensors.

1. INTRODUCTION

1.1 Background

Based on data provided by FHWA in 2012, more than 30% of the nation's bridges had exceeded their designed life. 11% of the bridges were classified as structurally deficient, and 15% were defined as functionally obsolete (1). On one hand, the structurally deficient and functionally obsolete bridges need to be replaced by new bridges. On the other hand, measures should be taken to make sure the safety of the bridges in operation, and structural health monitoring (SHM) is a very important part in this process.

The major objective of SHM is to detect and characterize damages in civil structures (2)(3). Damages can be reflected as deterioration in the material and/or geometric properties of the structures, and bring negative effects to structural performance. Damages can be accumulated during the regular service life or just caused by extreme events. SHM during the service life of structures are usually performed periodically in a long term (4). Performances of structures are evaluated based on data periodically collected from SHM systems, and compared with the intended performances from healthy structures to acquire information on structural aging and degradation (5). After extreme events such as earthquakes or floods, SHM can be performed to provide information regarding integrity of the structures so that further measures can be taken (6).

Cracking is a very popular damage to bridge girders and decks. It could be caused by excessive loads resulting from other damages such as movement of the foundation or failure of the expansion/contraction joints, or it just happens as a result of aging. Cracks in steel structures may raise the stress intensity in structural members and lead to fatigue failure (7). Cracks in reinforced concrete members may pave the way for the corrosion of reinforcement, jeopardizing the integrity of the structural members. As a result, crack detection and monitoring plays a very important role in SHM.

Different technologies and methods have been developed to detect and monitor structural cracks. The most direct way is visual inspections. Periodically, well-trained inspectors examine the structural members and evaluate their conditions. The evaluation could be appropriate and effective, but evaluation of similar conditions can vary widely from inspector to inspector due to the subjectivity (8). Recently, visual inspections have been replaced by digital images captured by cameras (9) (10) (11) and other graphic technologies (12). Installing a measurer or displacement sensor across a crack is one objective way to monitor the crack opening (13) (14). Ultrasonic method can be employed to monitor the development of a crack (15) (16) (17). Other technologies such as impact echo method (18) (19) (20) (21) and ground-penetrating-radar (22) (23) can help detect cracking damages beneath the structural surfaces.

In addition to direct inspections, damage identification algorithms can be developed based on data collected from different sensors such as strain gauges and accelerometers in an SHM system. Many algorithms are based on modal analysis (24) (25) (26) (27). Usually many sensors are needed to obtain a better accuracy in modal analysis, which would create a large sensor network (28) (29) and increase the budget.

Fiber optic sensing technologies was fast developing in the last 20 years (30) (31) (32). Compared to electrical sensors, fiber optic sensors have many advantages such as immunity to electromagnetic interference, resistance to corrosion and broad bandwidth for multiplexing (33). Many sensors were developed based on fiber Bragg grating (FBG) due to its sensitive to strain and temperature variations (34) (35) (36) (37) (38). FBG sensors with different wavelength can be multiplexed in a single channel, which can reduce the channels needed by a large sensing network (39).

Recently, fiber optic distributed sensing technologies are developing based on different optical phenomena in optical fibers (40) (41). Distributed sensing is ubiquitous and supposed to detect damages along the sensors' paths. As a result, fewer sensors would be involved to create a sensing network.

1.2 Principles of PPP-BOTDA

1.2.1 Scatterings in optical fibers

Rayleigh scattering, Raman scattering and Brillouin scattering are physical phenomena in optical fibers that have been utilized in distributed sensing technologies (42). The schema of the three scatterings is shown in Figure 1.

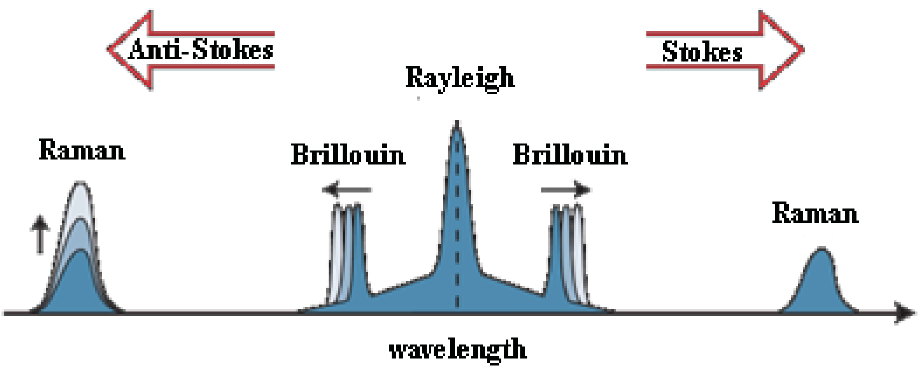

Figure 1. Scatterings in optical fibers

Rayleigh scattering is caused by random fluctuations in the refractive index along the fiber. The backscattered light has the same frequency with the incident light. The optical fiber can be modeled as a long weak FBG with a random period. The change in temperature and strain will shift the reflected Rayleigh scattering spectrum, which can be found by correlating the spectra of the scattered light and the incident light (43). Rayleigh scattering has been used to measure disturbance in temperature and strain in optical fibers (44) (45) (46) (47) (48).

Raman scattering is a processes due to intra-molecular vibrations and rotations. A linear relationship exists between changes in the power of anti-Stokes signal and temperature variations (49). Ramen scattering can be employed in distributed temperature sensing (50) (51) (52).

Brillouin scattering is due to the interaction between light waves (photons) and acoustic waves (phonons) in optical fibers (53). The acoustic waves work as a moving FBG. Due to the Doppler effects, the scattered light has a frequency shift from the incident light. Brillouin frequency shift (BFS) equals to the frequency of the phonons in the optical fiber, which are related to the strain and temperature variation in the fiber (54) (55) (56).

1.2.2 Brillouin scattering in optical fibers

Compared to the incident light, the Brillouin backscattered signal in a single mode optical fiber (SMF) has a frequency downshift given by Equation 1.1 (57).

$$\nu_B = \frac{2n_{eff}(z)V_a}{\lambda} \tag{1.1}$$

where n_{eff} is the effective mode refractive index, V_a is the velocity of sound wave, and λ is the wavelength of the incident light in vacuum. Variations in strain and/or temperature will cause changes in the local acoustic velocity and refractive index, and induce a shift in Brillouin frequency. A linear relationship exists between BFS and variations in strain and/or temperature, which is expressed by Equation 1.2 (58).

$$\nu_B = C_\varepsilon \Delta\varepsilon + C_T \Delta T \tag{1.2}$$

where C_ε and C_T are Brillouin strain factor and temperature factor, and can be obtained from calibration (59). For single mode fiber, $C_\varepsilon \approx 0.05\mathrm{MHz}/\mu\varepsilon$ and $C_T \approx 1\mathrm{MHz}/°\mathrm{C}$.

1.2.3 Spontaneous and stimulated Brillouin scattering

Spontaneous Brillouin scattering is caused by collective acoustic oscillations of the fiber materials in the natural state. The back-scattered light is usually weak, and can propagate tens of kilometers in optical fibers without significant attenuation (60) (61) (62). Brillouin optical time domain reflector (BOTDR) is based on spontaneous Brillouin scattering (63) (64).

Stimulated Brillouin scattering (SBS) takes place when an intense light beam is travelling in optical fiber (65) (66). The electrical field of the light beam creates acoustic vibrations in the optical fiber through electrostriction (67), and the resultant scattering is much stronger than spontaneous Brillouin scattering (68). SBS is initiated from spontaneous Brillouin scattering (69) and is a nonlinear phenomenon only happening when the intense of the light is above a threshold value (70). Brillouin optical time domain analysis (BOTDA) (71) and Brillouin optial correlation domain analysis (BOCDA) (72) are sensing technologies based on SBS.

Different Brillouin sensing technologies have their own scopes of application. BOTDR usually has a low spatial resolution (a few meters) and a long sensing distance (up to tens of kilometers). BOCDA can achieve very high spatial resolution (up to a few millimeters), but only have a short sensing distance (tens of meters). With pre-pump pulse (73) (74) (75) (76) and/or differential pulse pair (77) (78) (79) (80) technologies, BOTDA can achieve centimeter level spatial resolution, and the sensing distance can be up to a few kilometers.

1.2.4 BOTDA system

The schema of the BOTDA system is shown in Figure 2. The sensing fiber is connected to BOTDA at both ends. The pump light and pulse light are counter propagating in the optical fiber (71) (81). The location along the distributed sensor is recognized through the receiving time of the probe/backscattered light. The pump light is a short pulse, and the probe light is a continuous wave. Usually, the frequency of the pump light is a constant, while the frequency of the probe light is sweeping in a given range. When the probe light is at the Stokes frequency, energy transfers from the pump light to the probe light, creating a Brillouin gain in the probe light. The highest power of the pump light is limited by the nonlinear effect in the optical fiber (82).

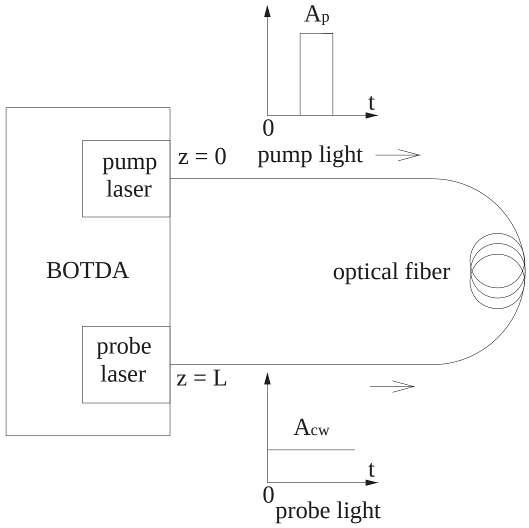

Figure 2. Schema of BOTDA system

The pump light $\tilde{E}_P(z,t)$, probe light $\tilde{E}_{CW}(z,t)$, and the acoustic wave $\tilde{\rho}(z,t)$ are expressed in Equations 1.3-1.5.

$$\tilde{E}_P(z,t) = \frac{1}{2}E_P(z,t)e^{i(k_P z - \omega_P t)} + c.c. \tag{1.3}$$

$$\tilde{E}_{CW}(z,t) = \frac{1}{2}E_{CW}(z,t)e^{i(-k_{CW} z - \omega_{CW} t)} + c.c. \tag{1.4}$$

$$\tilde{\rho}(z,t) = \frac{1}{2}\rho(z,t)e^{i(k_A z - \omega_A t)} + c.c. \tag{1.5}$$

where $E_P(z,t)$, $E_{CW}(z,t)$ and $\rho(z,t)$ are the amplitudes of the pump, probe and acoustic wave, respectively. They are functions of time t and position z along the fiber. k and ω are the angular frequency and the wave number. The SBS in the optical fiber can be expressed as the coupled Equations 1.6-1.8 (83).

$$\left(\frac{\partial}{\partial t} + v_g\frac{\partial}{\partial z}\right)E_P = i\kappa_1 E_{CW}\rho \tag{1.6}$$

$$\left(\frac{\partial}{\partial t} - v_g\frac{\partial}{\partial z}\right)E_{CW} = i\kappa_1 E_P\rho^* \tag{1.7}$$

$$\left(\frac{\partial}{\partial t} + \frac{\Gamma_B}{2} + i(\Omega_\mathrm{B}(\mathrm{z}) - \Omega)\right)\rho = i\kappa_3 E_P E_{CW}^* \tag{1.8}$$

where v_g is the group velocity of light. $\Omega_B(z)$ is the BFS at position z. Ω is the frequency difference between the pump light and the probe light, i.e. $\Omega = \omega_P - \omega_{CW}$. Γ_B is related to the natural Brillouin linewidth $\Delta\nu_B$ as $\Gamma_B = 2\pi\Delta\nu_B$, and $\Delta\nu_B = 35MHz$ (84). The coupling coefficients κ_1 and κ_3 are given by Equations 1.9-1.10 (85).

$$\kappa_1 = \frac{\pi v_g \gamma_e}{2n\lambda\rho_0} \tag{1.9}$$

$$\kappa_3 = \frac{\pi n \varepsilon_0 \gamma_e}{4\lambda v_a} \tag{1.10}$$

where γ_e is the elasto-optic coefficient, n is the refractive index, λ is the wavelength in vacuum, ρ_0 is the density of the fiber core, ε_0 is the permittivity in vacuum and v_a is the acoustic veloctiy.

The coupled Equations 1.6-1.8 can be solved with perturbation method, and the probe light received at the pump end is expressed by Equation 1.11 (73).

$$E_{CW}(0,t) = A_{CW}[1 + \gamma H^*(t,\Omega)] \tag{1.11}$$

where $\gamma = \frac{2\kappa_1\kappa_3}{\Gamma_B}$, and $H(t,\Omega)$ is the term for SBS, which is given by Equation 1.12.

$$H(t,\Omega) = \int_0^L A\left(t - \frac{2z}{v_g}\right) \int_0^\infty h(z,s) A\left(t - s - \frac{2z}{v_g}\right) ds dz \tag{1.12}$$

where $A(t)$ is the amplitude of pump light at the pump end. $h(z,s)$ is the phonon at position z which decays with time s exponentially and given by Equation 1.13.

$$h(z,s) = \Gamma \mathrm{e}^{-(\Gamma + \mathrm{i}(\Omega_B(z) - \Omega))s} \tag{1.13}$$

where $\Gamma = \frac{\Gamma_B}{2}$. The Brillouin gain spectrum $V(t,\Omega)$ received at the pump end is expressed by Equation 1.14.

$$V(t,\Omega) = \frac{1}{2}|E_{CW}(0,t)|^2 - \frac{1}{2}{A_{CW}}^2 = \frac{1}{2}\gamma {A_{CW}}^2 H(t,\Omega) + c.c. \tag{1.14}$$

1.2.5 Pre-pump pulse BOTDA (PPP-BOTDA)

The spatial resolution of BOTDA can be improved by a shorter pump light. However, pump light shorter than phonon lifetime (about 10 ns in silica fiber) results in broadening of the measured Brillouin gain spectrum. The width of the measured BGS could be a few hundred MHz, which is much larger than the natural Brillouin line width (~30MHz) (86). Accuracy of the measurement is reduced due to a low SNR, and it is difficult to capture the BFS from BGS. As a result, the spatial resolution of BOTDA cannot be better than 1 meter (87).

In order to improve the spatial resolution of BOTDA, new technologies have been developed in time domain (73) (74) (88) and frequency domain (72) (89). Pre-pump pulse BOTDA (PPP-BOTDA) is developed by introducing a pulse before the pump light. The duration of the pre-pump pulse is long enough to develop acoustic wave with a natural Brillouin spectrum width. Then a very short pump light (less than 10ns) can interact with the developed acoustic wave. With this method, centimeter level spatial resolution can be achieved.

For PPP-BOTDA, the pump light can be expressed by Equation 1.15 (73).

$$A(t) = \begin{cases} A_p + C_p & D_{pre} - D \le t \le D_{pre} \\ C_p & 0 \le t \le D_{pre} - D \\ 0 & elsewhere \end{cases} \tag{1.15}$$

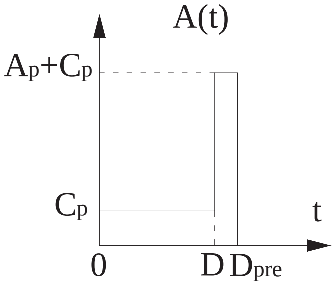

Figure 3. Pre-pump pulse and pump light

According to the shape of $A(t)$ shown in Figure 3, the integral given by Equation 1.12 can be divided to four parts, which are given by Equations 1.16-1.19 (90).

$$H_1(t,\Omega) = {A_p}^2 \int_{v_g(t-D_{pre})/2}^{v_g(t-D_{pre}+D)/2} \int_0^{t-D_{pre}+D-2z/v_g} h(z,s)dsdz \qquad (1.16)$$

$$H_2(t,\Omega) = A_p C_p \int_{v_g(t-D_{pre})/2}^{v_g(t-D_{pre}+D)/2} \int_0^{t-2z/v_g} h(z,s)dsdz \qquad (1.17)$$

$$H_3(t,\Omega) = A_p C_p \int_{v_g(t-D_{pre})/2}^{v_g(t-D_{pre}+D)/2} \int_0^{t-D_{pre}+D-2z/v_g} h(z,s)dsdz \qquad (1.18)$$

$$H_4(t,\Omega) = {C_p}^2 \int_{v_g(t-D_{pre})/2}^{v_g t/2} \int_0^{t-2z/v_g} h(z,s)dsdz \qquad (1.19)$$

1.2.6 Brillouin scattering based crack detection

Structural cracks on the path of a distributed sensor would induce additional strains in the distributed sensor, which can be measured as Brillouin frequency shift by BOTDA/R. Many experimental researches regarding crack detection with BOTDA/R system were based on this idea (91) (92) (93) (94) (95). Generally, SR is the most important factor for crack detection. The strain induced by a crack decays very fast with distance from the crack location in the optical fiber. With a low SR, the strain induced by a crack would be immersed by the background strain, and cannot be recognized until the crack is wide enough (91). One option is to take the point-fixation style instead of the overall-bonding style for sensor installation (96). The segment between two neighboring fixed-points should be longer than the SR. In this method, the distributed sensor is actually consisted of a series of discrete sensors. A linear relationship exists between the measured BFS (strain) and the varying distance between two fixed points. However, multiple cracks within one segment cannot be differentiated.

Crack detection and monitoring based on Brillouin scattering could be improved by using a higher SR. Recently, PPP-BOTDA with centimeter SR has been applied in crack detection based on distributed strain sensing (97) (98) (99). Lab tests were carried out and the results were claimed successful. However, the researches only focused on experimental results and were lack of theoretical analysis.

1.3 Research methodology

The objective of the research presented in this dissertation is to study the capability of PPP-BOTDA in crack detection and monitoring based on theoretical analysis and experimental tests, so that the results from tests can be fully understood and guidance for further application could be provided.

In Chapter 2, changes in BGS due to crack-induced strain are studied theoretically and experimentally for a distributed optical sensor crossing over a crack on the structural surface. The crack-induced strain in the optical sensor is analyzed based on strain transfer mechanism and works as the input of numerical simulation. Numerical simulation is performed based on the principles introduced in Section 1.2. Experimental research is carried out through the plate-crack test. Result from numerical simulation and experimental research are characterized by Brillouin frequency shift (BFS) and the width difference of Brillouin gain spectrum (BGSWD). The effects of SR and COD on the results are discussed.

In Chapter 3, load tests of structural members including one steel beam and three reinforced concrete beams are employed for crack detection and monitoring with PPP-BOTDA system. Cracks would develop in the members during the load and are expected to be detected and monitored by BFS and BGSWD measured by the surface-installed distributed sensor.

In Chapter 4, the study on capability of PPP-BOTDA in differentiating neighboring cracks is introduced. Similar to the single-crack case, both numerical simulation and experimental research are performed. The effects of SR on differentiating neighboring cracks are considered for different crack spacing. General guidance is provided for crack detection and monitoring with PPP-BOTDA distributed sensors.

In Chapter 5, load tests of two RC beams are introduced for crack detection and monitoring with an improved SR. Multiple cracks are expected to be detected and monitored from the measured BFS and BGSWD.

In Chapter 6, contributions of the study presented in this dissertation are summarized. Existing issues in the research and possible improvements for further research are discussed.

2. CRACK- INDUCED CHANGES IN BGS

2.1 Crack-induced strain in distributed sensors

2.1.1 Strain transfer mechanism

Strain is transferred from the structure to the distributed sensor by deformations of surrounding materials such as protective layers of the fiber and the adhesive (100). The mechanism of strain transferring from the structural surface to a surface-installed fiber optic sensor has been studied by some scholars. Ansari et al. (101) introduced a shear transfer model to analyze the development length of a fiber optic sensor. The analysis was based on a few assumptions such as linear elastic behavior for the fiber materials, prefect bonds between all interfaces, and same mechanical properties for the core and cladding. For a sensor with gauge length of 2L, the strain distribution in the optical fiber is given by Equation 2.1.

$$\varepsilon_g(x) = \varepsilon_m \left[1 - \frac{\sinh(kx)}{\sinh(kL)}\right] \tag{2.1}$$

where ε_g is the strain in the fiber core, ε_m is the strain in the structure, k is the factor accounting for the shear lag effect from the buffering layers, x is the distance from the center of the sensor, and L is half of the gauge length.

Wan, et al. (102) employed 3D finite element modeling to analyze the strain in a surface – mounted FBG sensor. The effects of geometric parameters of the adhesive such as the side width, top thickness, bond length and bottom thickness on the strain transfer was investigated. It was revealed that the bond length and the bottom thickness are dominant factors. It was also concluded that the analytical strain transfer model was only valid for small shear lag factors.

2.1.2 Crack-induced strain

A crack will cause discontinuity of the displacement field in the structure, while the displacement field in the sensor is still continuous. Feng et al. (103) analyzed the crack-induced strain in the distributed sensor based on the strain transfer mechanism. The problem is depicted in Figure 4. The displacement field of the structure can be expressed by

$$u_m(x) = \varepsilon_m x + \delta \tag{2.2}$$

where $u_m(x)$ is the displacement field in the structure, ε_m is the constant strain in the structure, x is the distance from the crack, and δ is half the width of the crack. For elastic analysis, the strain distribution in the sensing fiber is expressed by

$$\varepsilon_f(x) = -\beta C_1 \exp[\beta(L-x)] + \beta C_2 \exp[\beta(L+x)] + \varepsilon_m \tag{2.3}$$

where β is the shear lag factor, C_1 and C_2 are two constants given by Equations 2.4-2.5.

$$C_1 = -\frac{\delta \exp(2\beta L)}{\exp(\beta L)+\exp(3\beta L)} \tag{2.4}$$

$$C_2 = -\frac{\delta}{\exp(\beta L)+\exp(3\beta L)} \tag{2.5}$$

In addition to the elastic analysis, Feng also considered an ideal elasto-plastic model for the polymeric coating of the fiber, which was developed for cases with large crack opening displacements (CODs).

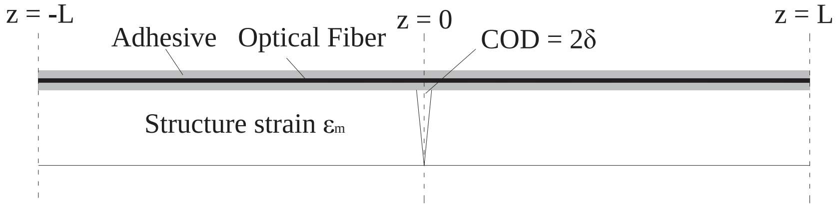

Figure 4. Optical fiber sensor of length 2L traversing a single crack

Different elasto-plastic models were considered for the polymeric coating by other scholars. Imai et al (104) introduced a sudden softening model for the surrounding materials including the polymeric coating of optical fiber and the adhesive. The maximal strain in the surrounding materials and the debonding-initiated crack width were determined experimentally.

Even though plastic deformation may take place in the fiber coating and the adhesive layer, the elasto-plastic model is lack of support from experimental facts, since test data concerning the stress-strain relationship for the polymeric coating was not available. In addition, plastic deformation and debonding between different materials are not obvious when the COD is small. Under these considerations, elastic analysis is reasonable and feasible for the theoretical research.

2.1.3 Theoretical analysis

The details of the elastic analysis for the single-crack problem was introduced in (103), and major equations were cited in this section only for completeness. According to Figure 4, the distributed sensor is bonded to the surface of the structure from $z = -L$ to $z = L$. The COD 2δ is located at $z = 0$. Since the structural strain is released at the crack location, it is supposed that $\varepsilon_m = 0$ within the crack vicinity. The strain distribution $\varepsilon_f(z)$ in the optical fiber was derived from the equilibrium of force and compatibility of the displacement field. A segment of the optical fiber together with the adhesive layer is taken out and shown in Figure 5.

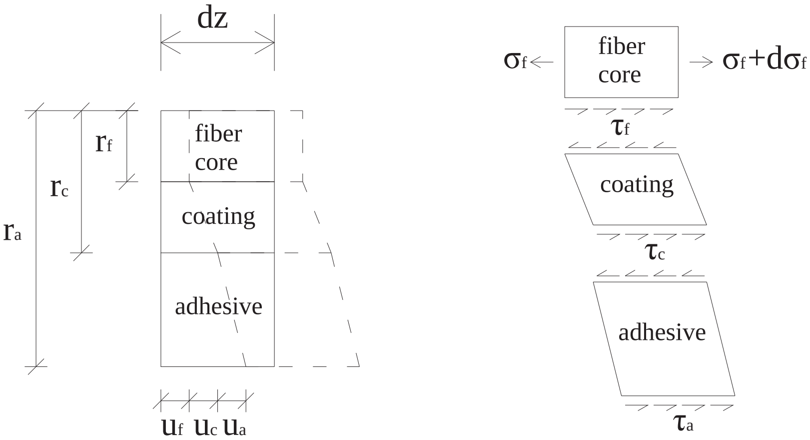

(a) deformation (b) stress

Figure 5. Schema of the deformation and stress analysis of a fiber segment

For a small segment dz at location z, suppose the stress is evenly distributed in the fiber core and ignores the shear strain and stress, the force equilibrium in the fiber core is given by Equation 2.6.

$$\frac{d\sigma(z)}{dz} + \frac{2\tau_f(z)}{r_f} = 0 \tag{2.6}$$

If the normal stress in the polymeric coating and the adhesive layer is neglected, the force equilibrium in the polymeric coating and adhesive layer can be given by

$$\tau(z, r) = \frac{r_f}{r}\tau_f(z) \tag{2.7}$$

The deformation in the fiber core at location z is expressed as

$$u_f(z) = \int_0^z \varepsilon_f(z)dz = \int_0^z \frac{\sigma(z)}{E_f}dz \tag{2.8}$$

For the cross section shown in Figure 5, the shear deformation of the polymeric coating $u_c(z)$ and adhesive layer $u_a(z)$ can be acquired by Equations 2.9-2.10

$$u_c(z) = \int_{r_f}^{r_{c2}} \gamma(z, r)dr = \alpha_c\tau_f(z) \tag{2.9}$$

$$u_a(z) = \int_{r_c}^{r_a} \gamma(z, r)dr = \alpha_a\tau_f(z) \tag{2.10}$$

where $\alpha_c = r_f\left(\frac{1}{G_{c1}}\ln\frac{r_{c1}}{r_f} + \frac{1}{G_{c2}}\ln\frac{r_{c2}}{r_{c1}}\right)$ and $\alpha_a = \frac{r_f}{G_a}\ln\frac{r_{c2}}{r_a}$

The compatibility of deformation at location z is given as

$$u_f(z) + u_c(z) + u_a(z) = \delta \tag{2.11}$$

Equation 2.11 can be transformed to Equation 2.12 by replacing $u_f(z)$, $u_c(z)$ and $u_a(z)$ with Equations 2.8-2.10.

$$u_f(z) = \delta + \frac{E_f r_f(\alpha_c+\alpha_a)}{2} u_f''(z) \tag{2.12}$$

The displacement field in the sensing fiber is obtained as Equation 2.13 by solving Equation 2.12.

$$u_f(z) = C_1 \exp(\beta z) + C_2 \exp(-\beta z) + \delta \tag{2.13}$$

where β is the shear lag effect factor, which is given by Equation 2.14. β is related to the material and geometric properties of the optical fiber and the adhesive layer.

$$\beta^2 = \frac{2}{E_f r_f(\alpha_c+\alpha_a)} \tag{2.14}$$

The strain in the fiber core is obtained by differentiating Equation 2.13 once.

$$\varepsilon_f(z) = \beta C_1 \exp(\beta z) - \beta C_2 \exp(-\beta z) \tag{2.15}$$

The boundary conditions for the single crack case can be expressed as $u_f(0) = 0$ and $\varepsilon_f(\pm L) = 0$. For the segment of $z > 0$, constants C_1 and C_2 are determined from the boundary conditions and given by

$$C_1 = -\frac{\delta}{\exp(2\beta L)+1} \tag{2.16}$$

$$C_2 = -\frac{\delta\exp(2\beta L)}{\exp(2\beta L)+1} \tag{2.17}$$

When $\exp(2\beta L) \gg \delta$, $C_1 \approx 0$ and $C_2 \approx -\delta$. For the segment of $z > 0$, the strain in the fiber core can be simplified as Equation 2.18 (105).

$$\varepsilon_f(z) = \delta\beta\exp(-\beta z) \tag{2.18}$$

Due to symmetry with respect to the crack location, the strain in the fiber induced by a COD 2δ at $z = 0$ can be expressed as a piecewise exponential function by Equation 2.19.

$$\varepsilon_f(z) = \begin{cases} \delta\beta\exp(-\beta z) & z > 0 \\ \delta\beta\exp(\beta z) & z \leq 0 \end{cases} \tag{2.19}$$

One issue with Equation 2.19 is to determine the value of β. In (102) (103) (104), β was calculated through Equation 2.14. In this process, even though the geometric boundary of the adhesive layer was simplified as a circle, no explanation was provided for determination of the radius of the adhesive layer. As described later in this chapter, β was determined from finite elements analysis in this study.

For embedded distributed sensors, theoretical analysis of strain induced by a crack could follow a similar process. Even though the mechanism of strain transfer and the material properties may be different, it is believed that shear lag factors could also be available for embedded distributed sensors.

2.1.4 Determination of shear lag factor

Three-dimensional finite element analysis (FEA) was employed to acquire the shear lag factor β for the surface-installed distributed sensor. The center of the fiber core at the crack location was selected as the origin of the finite element model. In the model, the optical fiber was supposed bonded to the structural surface by an adhesive layer from $z = -1\text{m}$ to $z = 1\text{m}$. The mechanical properties of the adhesive layer were chosen to mimic the adhesive employed in a following experiment. The optical fiber was modeled with two coating layers to mimic Corning's SMF28 optical fiber which was used in the following experiment. The cross section of the optical fiber is shown in Figure 6.

Compared to the soft adhesive layer, the base structure was with much higher Young's modulus and can be treated as a rigid body and not included in the model. The COD was applied to the bottom surface of the adhesive layer. As shown in Figure 7, only one quarter of the model was modeled in ANSYS, since the analyzed problem is symmetric to the planes $x = 0$ and $z = 0$. No slippage between different material layers was considered in the FEA. The mechanical properties of the materials involved are shown in Table I.

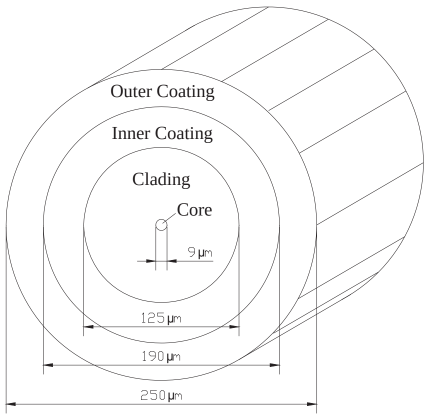

Figure 6. Cross section and dimensional properties of SMF28 optical fiber

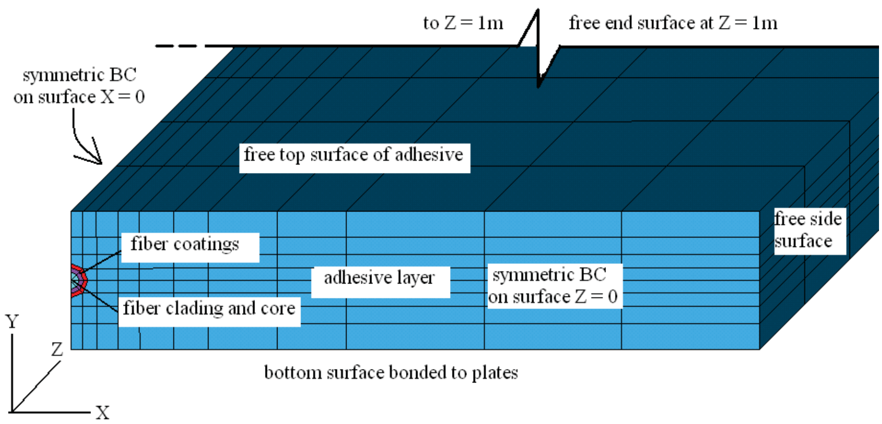

Figure 7. Cross section view of FE model of the single crack experiment

Table I. Mechanical properties of interfaces

Materials	Young's Modulus (MPa)	Poisson's ratio
Fiber core and cladding	72 000	0.2
Inner Acrylate coating	4.17 (106)	0.48
Outer Acrylate coating	904 (106)	0.46
Silicon rubber based adhesive	4	0.48

By fitting the crack-induced strain in the sensing fiber from FEA with Equation 2.19, β was determined as 45.11/m. The comparison between strains from FEA and Equation 2.19 under COD of 25μm is shown in Figure 8. The maximal difference in strains was 4.27%, which occurred at the crack location. With all the materials being linear elastic, FEA showed the crack-induced strain was proportional to the COD. For different CODs, the strain distribution according to Equation 2.19 is shown in Figure 9. Since the objective of the study presented here pertained to detection and monitoring of small cracks, the stress levels at the various interfaces within the optical fiber materials were rational for the linear elastic analysis.

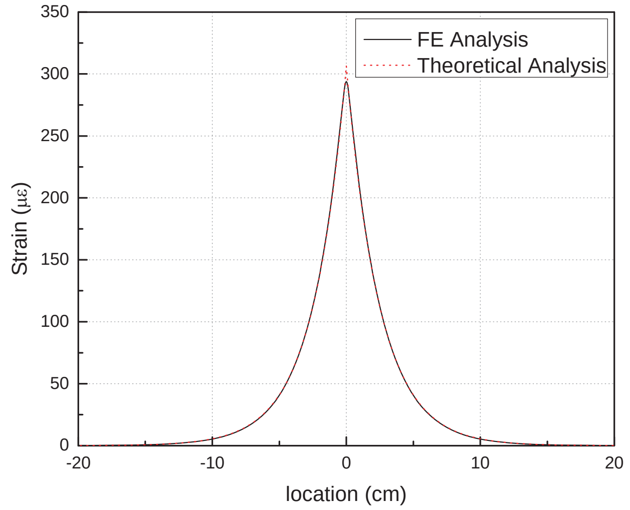

Figure 8. Strain distribution along the fiber length for a COD of 25µm

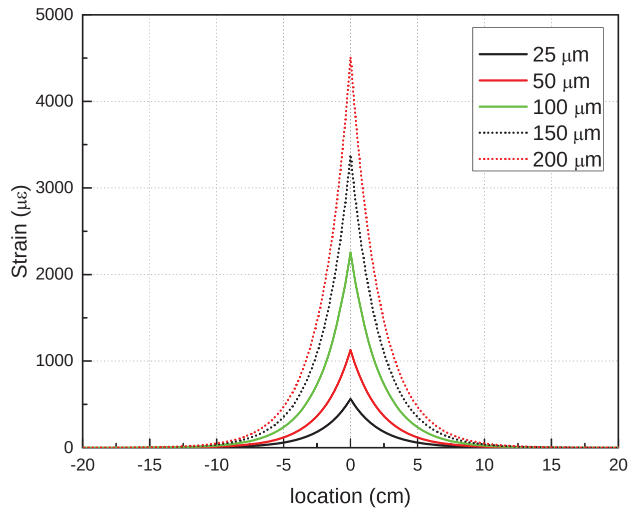

Figure 9. Strain distributions for all the simulated CODs based on theoretical analysis

2.2 <u>Numerical simulation of PPP-BOTDA</u>

2.2.1 <u>Principles</u>

Theoretical strain analysis indicated that a crack would induce a piecewise exponential distributed strain in the surface-installed distributed fiber optic sensor. The strain sharply decays with distances away from the crack location. With this distributed strain input, BGS at different locations along the distributed sensor can be predicted by Equation 1.14. Numerical simulation was realized by solving Equation 1.14 in Matlab, and the program can be referred to Appendix A.

The change in BGS can be characterized by Brillouin frequency shift (BFS), the variation in the 1dB width of the BGS (BGSWD), and the peak power of the BGS. These characters are defined in Figure 10.

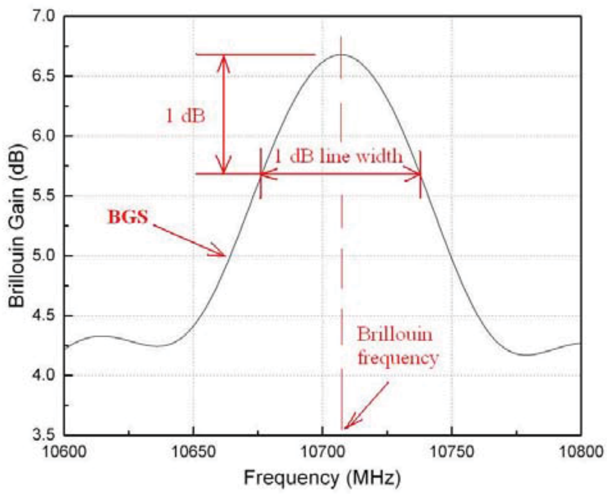

Figure 10. Characters of BGS

2.2.2 Results from numerical simulation

Numerical simulation was performed with different spatial resolutions (50cm, 20cm and 10cm SRs). The extinct ratio was set at 25dB. With the distributed strains from Figure 9 as the input, BGS at the crack location ($z = 0$) when 20cm SR was employed are shown in Figure 11. In Figure 11, both BFS and BGSWD increased with growth of CODs while the peak power decreased. However, the peak power was not employed as a character of BGS in this study due to two reasons: The commercial PPP-BOTDA device did not provide peak power of BGS as an output; the peak power of BGS from the following test was found not consistent.

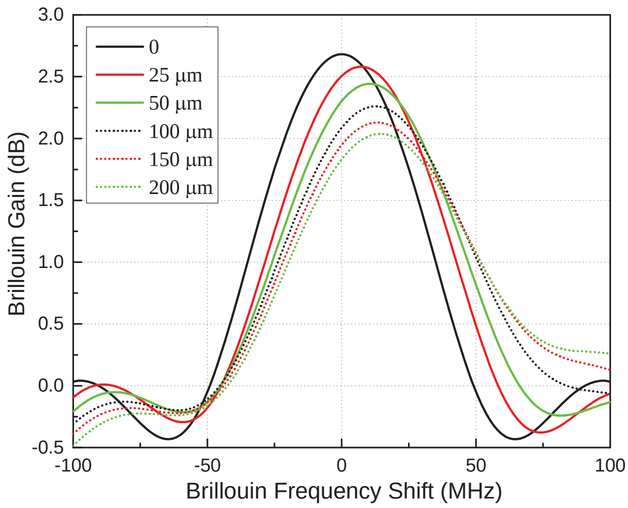

Figure 11. BGS from numerical simulation under different CODs

The BFS and BGSWD from numerical simulation are shown in Figure 12. For all the SRs employed, the crack was recognized as a single peak from both BFS and BGSWD. Comparing to the theoretical strain in Figure 9, the strain converted from BFS (1 MHz $\approx 20\mu\varepsilon$) in Figure 12(a) (c) (e) was very small. Due to a limited SR, the BGS measured at the crack location was affected by nearby locations where strain was low.

Even though the input strain was symmetric to the crack location, the distributed BFS and BGSWD were non-symmetric to the crack location. This asymmetry is due to the stepwise shape of the pump pulse. The peaks from BFS and BGSWD were close but not at the exact crack location and they moved towards the crack location under a larger COD.

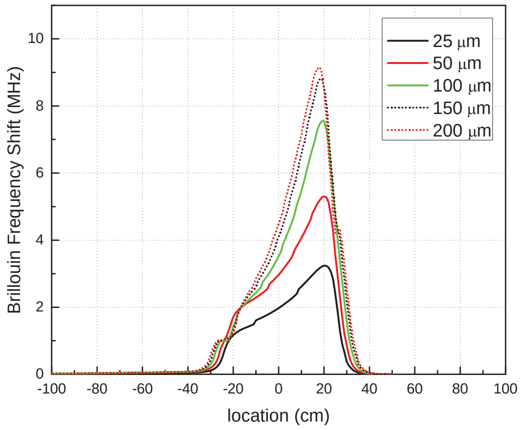

(a) BFS with 50cm SR

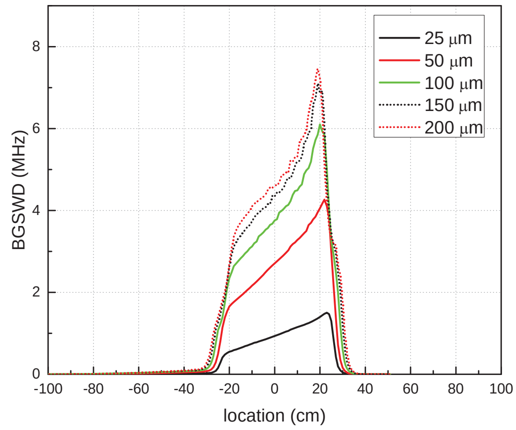

(b) BGSWD with 50cm SR

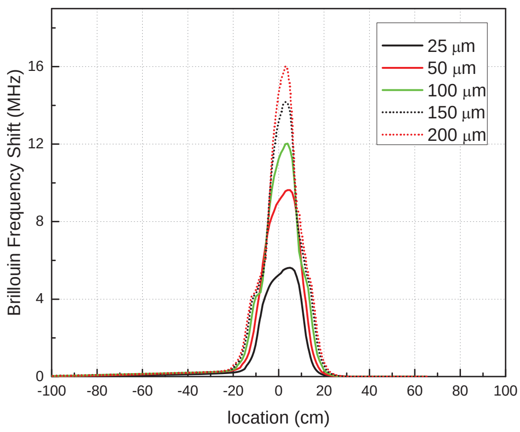

(c) BFS with 20cm SR

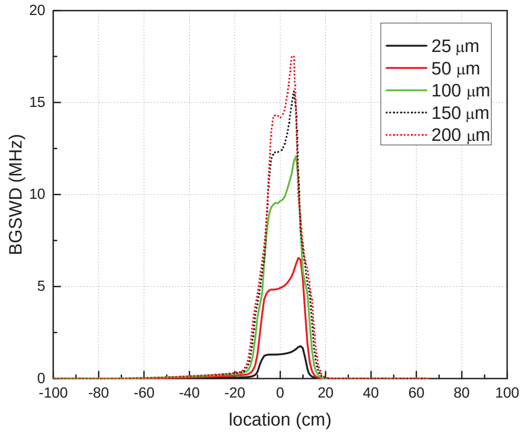

(d) BGSWD with 20cm SR

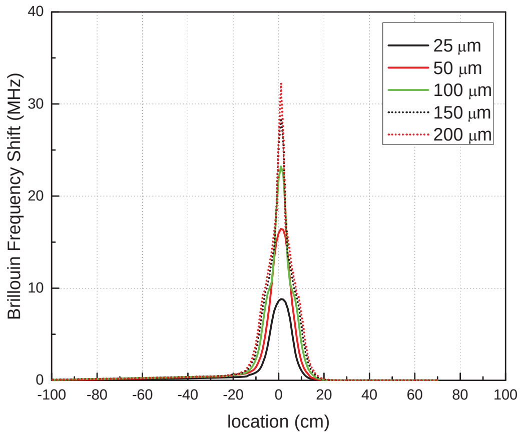

(e) BFS with 10cm SR

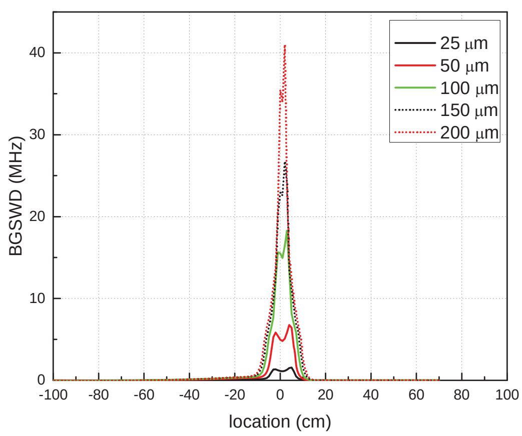

(f) BGSWD with 10cm SR

Figure 12. BFS and BGSWD from numerical simulation with different SRs

The amplitudes of BFS and BGSWD are shown in Figure 13. For each SR, the amplitudes of BFS and BGSWD increased with the COD. When 50cm SR or 20cm SR was employed, the growth of the amplitudes slowed down when the COD was close to $200\ \mu m$. In addition, the amplitudes of BFS and BGSWD increased when an improved SR was employed.

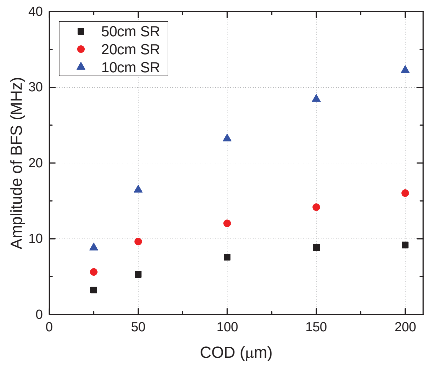

(a) BFS

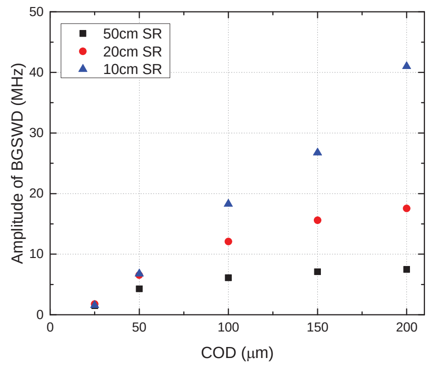

(b) BGSWD

Figure 13. Amplitudes of BFS and BGSWD from numerical simulation

The affected lengths was defined as full width at half maximum (FWHM) for BFS and BGSWD. The affected lengths of BFS and BGSWD are shown in Figure 14. For each SR employed, the affected lengths did not change much under different CODs. The averaged affected lengths of BFS and BGSWD decreased when an improved SR was employed. The affected lengths of BFS and BGSWD were quite close to each other when 20cm SR or 10cm SR was employed.

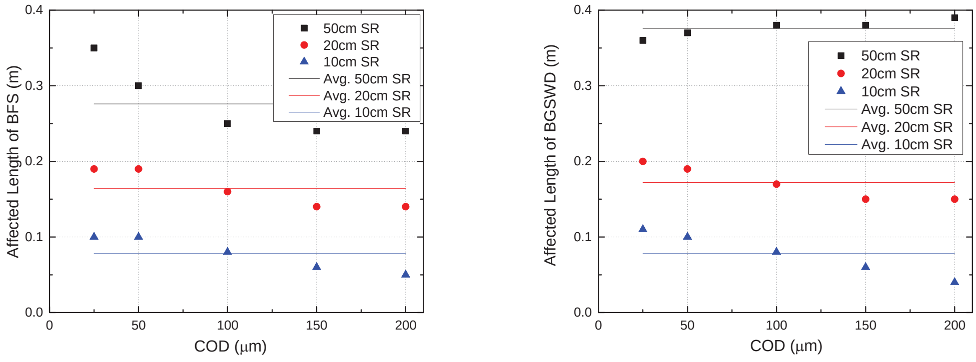

(a) BFS (b) BGSWD

Figure 14. Affected lengths of BFS and BGSWD from numerical simulation

2.2.3 Issues in numerical simulation

Numerical simulation is simplified and idealized modeling of PPP-BOTDA. There are differences between the numerical simulation and a real PPP-BOTDA device. For example, the pump light in a real PPP-BOTDA device is not a step function (107). Many effects were neglected in the numerical simulation, such as signal loss, noise brought by electrical elements, attenuation from materials, depletion of the pump light, and etc. The simplification and idealization would cause discrepancies in results between numerical simulation and test measurement. Irrespective of these challenges, the objective for the study is to determine whether the changes in BGS from a real PPP-BOTDA system could be employed in crack detection and monitoring, even though the results may be questionable due to the above-mentioned experimental realities.

2.3 Single-crack test

2.3.1 Test setup

The single-crack test was designed to simulate the opening of a crack between two aluminum plates. Schematic of the test setup is shown in Figure 15. Two pieces of aluminum plates were machined and positioned next to each other on precision micrometer stages. The test setup was designed for the plates to have capability for full closure or separation by using the precision micrometer. One section of the plate was fixed and the other was provided with translation capabilities. Translation of the plate created the opening of the crack. The experimental setup mimicked the case from numerical simulation, where the 2-meter long optical fiber was adhered to the surface of the specimen with one meter of fiber on each side of the crack. The optical fiber was pre-tensioned and bonded onto the surfaces of the plates by a thin layer of adhesive (approximately 1 mm), and also to act as cover to protect the upper surface of the optical fiber against accidental damage during the experiments. The FBG based displacement gauges are employed to measure the crack opening displacement at the center of the crack. Both the distributed sensor and displacement gauge were temperature compensated. The photo of the experiment setup is shown in Figure 16.

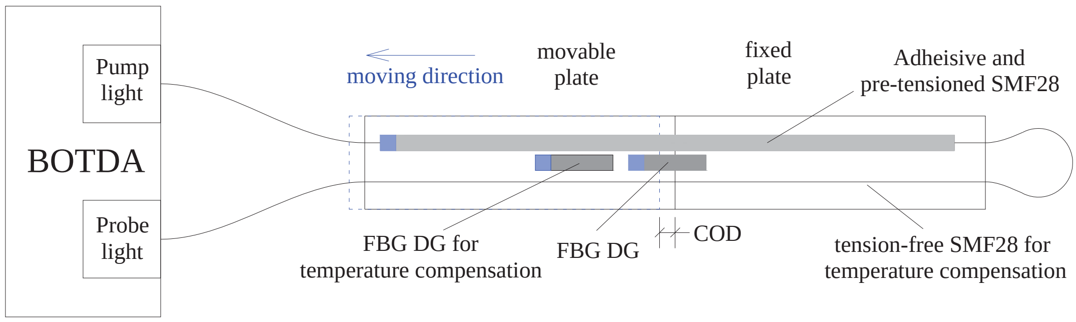

Figure 15. Schematics of the crack test setup

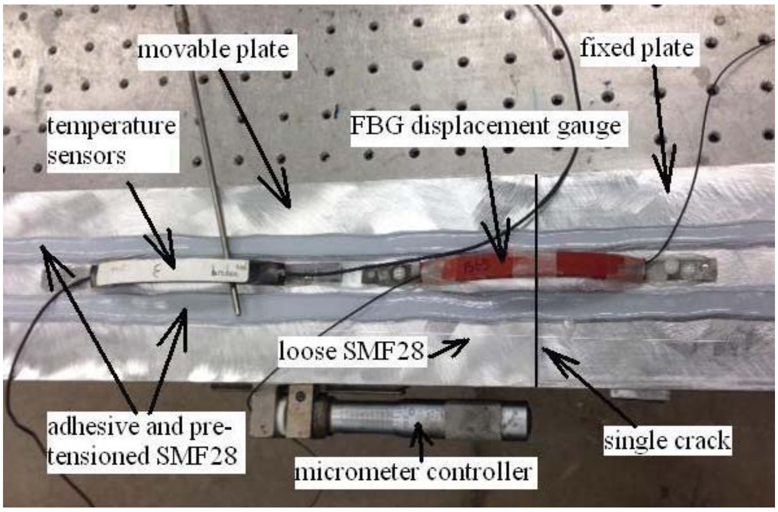

Figure 16. Single-crack test setup

2.3.2 PPP-BOTDA device

A commercially available PPP-BOTDA device (Neubrex NBX-6055) (108) was employed to perform the distributed measurements. All the input parameters for the PPP-BOTDA were selected in consonance with the parameters selected for the numerical simulations, i.e. 50cm, 20 cm and 10cm SRs and pump light extinct ratio R_x of 25dB. Even though the device was capable of performing tests with 5cm SR, the lower SRs were chosen due to better measurement repeatability with affordable time consumption. BFS and BGSWD in the sensing fiber were measured for CODs ranging from $25\mu m$ to $200\mu m$.

2.3.3 Results from tests

The BGS measured at the crack location when 20cm SR was employed are shown in Figure 17 as an example. Both BFS and BGSWD increased with the COD. However, no definite relationship was shown between the maximal Brillouin gain and the COD.

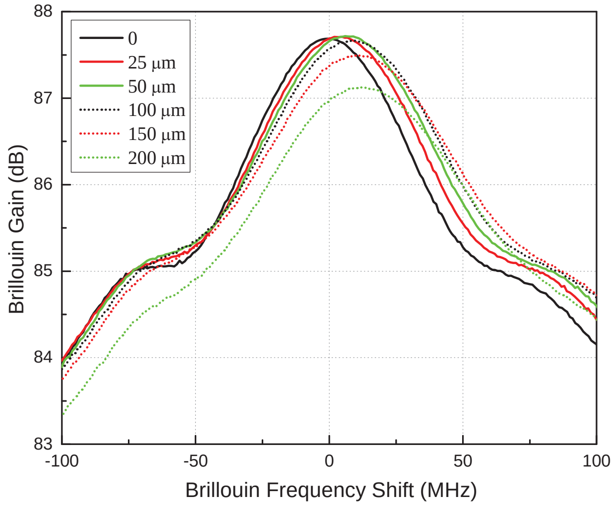

Figure 17. BGS measured at the crack location under different CODs

The BFS and BGSWD measured by PPP-BOTDA are shown in Figure 18. Similar to the results from numerical simulation, the crack was recognized from both BFS and BGSWD for all the SRs employed. Compared to numerical simulation, BFS and BGSWD measured from the test were more symmetric to the crack location.

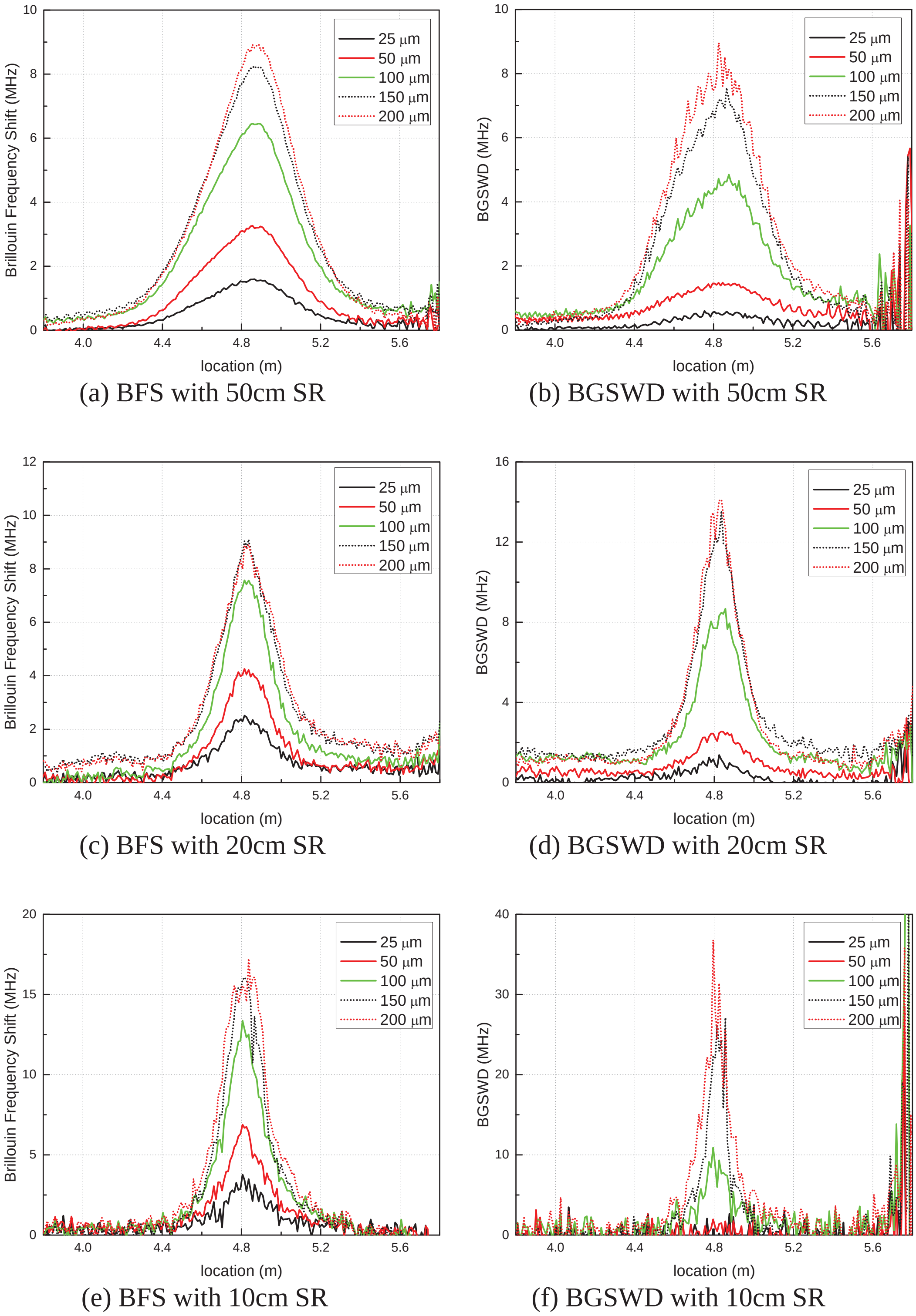

(a) BFS with 50cm SR (b) BGSWD with 50cm SR

(c) BFS with 20cm SR (d) BGSWD with 20cm SR

(e) BFS with 10cm SR (f) BGSWD with 10cm SR

Figure 18. BFS and BGSWD from single-crack test

The amplitudes of BFS and BGSWD measured with different SRs are shown in Figure 19. Similar to numerical simulation, the amplitudes were positively related to the COD. When 50cm or 20cm SR was employed, the amplitudes tended to stop growing as the COD was close to 200μm. The amplitudes of BFS and BGSWD increased with an improved SR. Compared to numerical simulation, the amplitudes of BFS and BGSWD measured from the tests were lower when 20cm SR or 10cm was employed. The difference between BFS measured with 50cm SR and 20cm SR was not obvious. The BGSWD was less sensitive for small CODs.

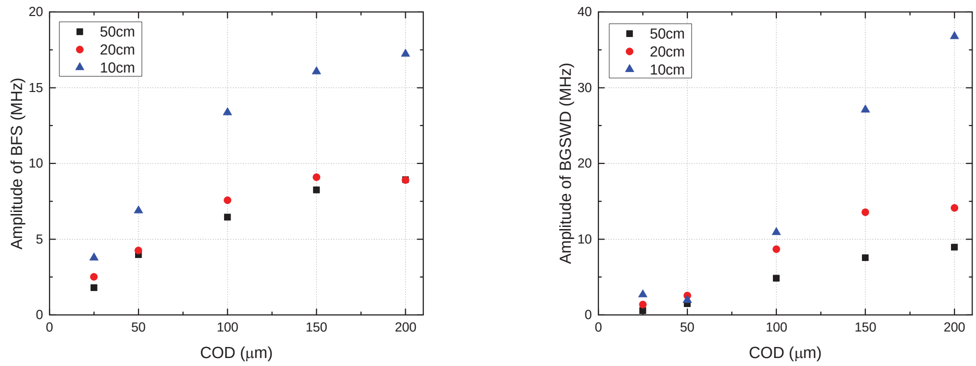

(a) BFS (b) BGSWD

Figure 19. Amplitudes of BFS and BGSWD from test measurement

The affected lengths of BFS and BGSWD are shown in Figure 20. Similar to numerical simulation, the affected lengths did not change much under different CODs for each SR employed. The averaged affected lengths decreased with an improved SR. Comparing BFS and BGSWD measured with each SR, BGSWD had a smaller affected length than BFS when 20cm SR or 10cm SR was employed. Compared to affected lengths from numerical simulation in Figure 14, the averaged affected length from the test was larger for each SR.

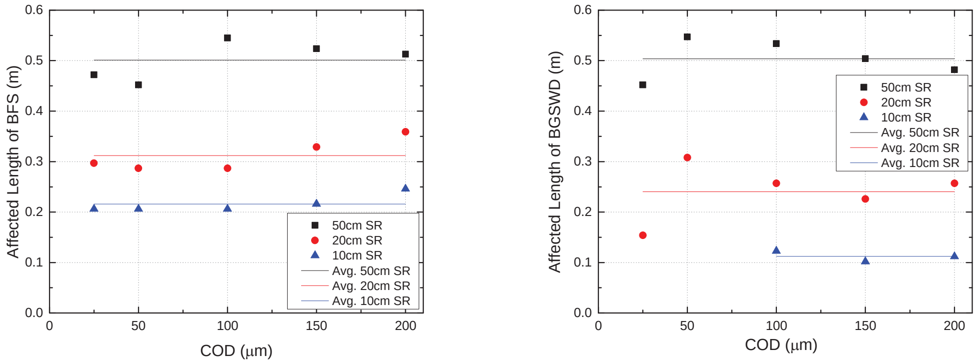

(a) BFS (b) BGSWD

Figure 20. Affected lengths of BFS and BGSWD from test measurement

2.4 Summary

Theoretical and experimental study of PPP-BOTDA distributed sensing in crack detection and monitoring was carried out. The performance of PPP-BOTDA in crack detection and monitoring was first simulated by numerical simulation, and then tested through the single-crack test with a commercial PPP-BOTDA device.

Numerical simulation was performed by programming the equations describing the principles of PPP-BOTDA in Matlab. The crack-induced strain in the distributed sensor was analyzed based on strain transfer mechanism and employed as the input of numerical simulation. BGS along the distributed sensor was acquired as the output of numerical simulation. BFS and BGSWD were employed to characterize the changes in BGS due to the COD. The crack was recognized as a peak from BFS and BGSWD. The amplitudes of BFS and BGSWD were positively related to the COD, and increased with an improved SR. The affected lengths of BFS and BGSWD were usually not sensitive to COD, and decreased with an improved SR.

The test setup mimicked the single-crack problem studied in the numerical simulation. General similarity existed between the results from numerical simulation and test measurement. However, differences were found due to effects neglected in numerical simulation. Compared to numerical simulation, BFS and BGSWD from tests were more symmetric to the crack location. The amplitudes of BFS and BGSWD measured from the test were usually lower than the amplitudes predicted by numerical simulation. The BGSWD was not sensitive as expected for small CODs. The averaged affected lengths of BFS and BGSWD from the test were also larger for each SR.

Though the results from numerical simulation and test measurement were different in some ways, it was proved that BFS and BGSWD were capable of crack detection and monitoring.

3. CRACK DETECTION AND MONITORING ON STRUCTURAL MEMBERS

3.1 Introductions

In chapter 2, PPP-BOTDA distributed sensing was proved capable of detecting and monitoring a crack by numerical simulation and experimental test. It was shown that appearance and widening of a crack would induce a change in the BGS, which was characterized by BFS and BGSWD. In this chapter, crack detection and monitoring based on PPP-BOTDA distributed sensing technology took one more step towards engineering application. Four-point-bending load tests were performed on structural members including one steel beam and three reinforced concrete (RC) beams in the lab. PPP-BOTDA distributed sensors were installed on these structural elements. Cracks appeared during the load tests were expected to be detected and monitored by the distributed sensors. Designs of the tests were introduced and results were discussed in the following sections of this chapter.

3.2 Load test of the steel beam

3.2.1 Test setup

Crack detection and monitoring was performed on a steel beam under a series of four-point-bending tests. The design of the steel beam is shown in Figures 21 and 22.The beam was 15-meter long, and fabricated by splicing three W4 × 13 segments. The three segments were 4.25m, 6.13m and 4.38m long, respectively. Two neighboring segments were spliced by gussets, and a small gap existed at each splice. The splice is shown in Figure 23.

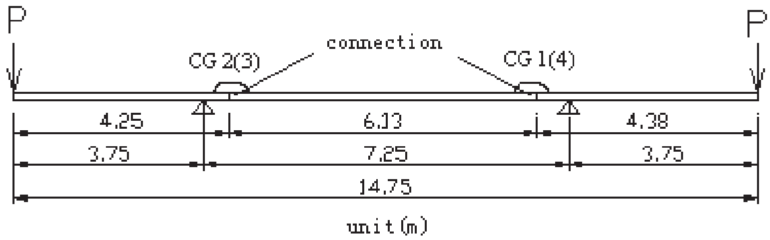

Figure 21. Schema of the load test of the steel beam

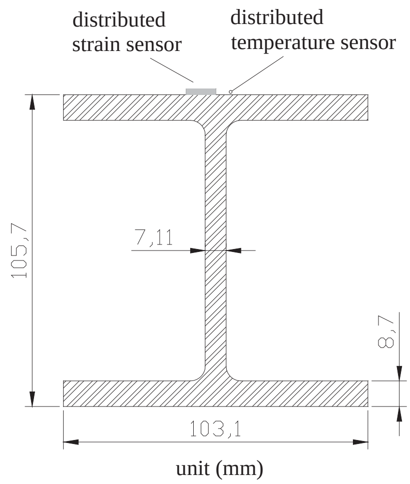

Figure 22. Cross section of the steel beam

Two supports were located at 3.75m away from each end, leaving the mid span 7.25m long. The two splices located within the pure bending zone. During the load test, tension developed in the top flange. The gaps on the top flange opened up and mimicked the widening of two cracks.

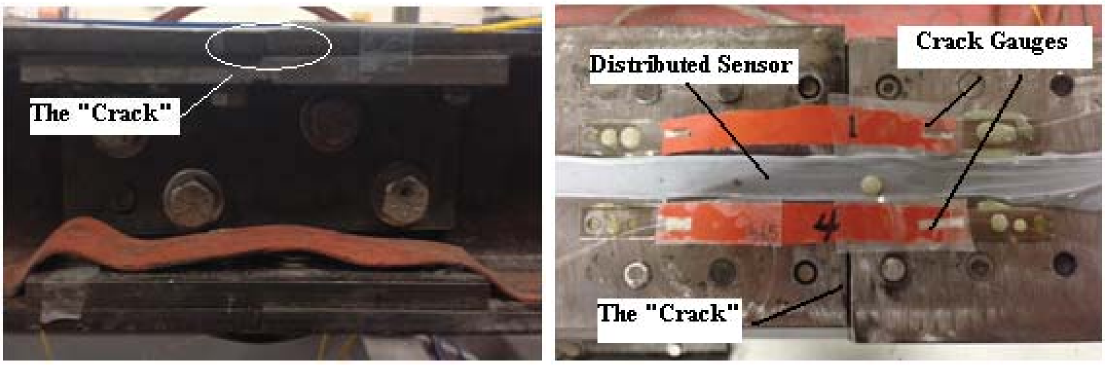

(a) side view (b) top view

Figure 23. The splice between two segments

The tensioned SMF was adhered to the top flange of the beam with silicon rubber adhesive and worked as the strain sensor. The strain-free SMF was installed on its side to compensate thermal effects caused by temperature variation. These distributed sensors can be seen in Figure 23(b). In fact, the load test was performed in a short time period in the lab, and the temperature variation was insignificant. FBG displacement sensors (CG1-4) were installed on the top flange of the beam at the splices to monitor the CODs, which can be seen in Figures 21 and 23(b).

3.2.2 <u>Strain for an intact beam</u>

Based on the Euler – Bernuli beam model (109), the strain under a bending moment can be calculated by Equation 3.1 for the steel beam.

$$\varepsilon(x) = \frac{M(x)}{EI} y \tag{3.1}$$

where y is the distance from the neutral axis, M(x) is the bending moment on the cross section, and EI is the flexural stiffness. As $y = \frac{h}{2}$ for the top flange, the strain on the top flange can be expressed as

$$\varepsilon(x) = \frac{M(x)h}{2EI} \tag{3.2}$$

The schema of the bending moment and strain on the top flange under the four-point-bending test is shown in Figure 24. M_0 is the bending moment in the pure-bending segment, and $\varepsilon_0 = \frac{M_0 h}{2EI}$. For different loads employed in the four-point-bending tests, ε_0 was calculated and listed in Table II.

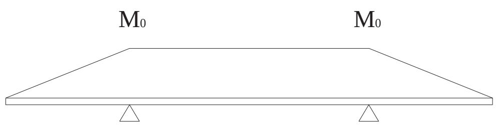

(a) Bending moment

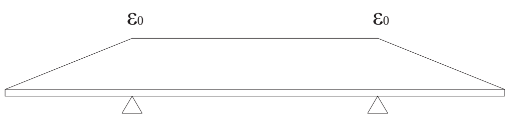

(b) Flexural strain on the top flange

Figure 24. Schema of the bending moment and flexural strain

Table II. ε_0 from theoretical analysis for different loads

Load P (N)	267	445	623	801	1023.5
ε_0 ($\mu\varepsilon$)	55.95	93.25	129.34	166.63	213.86

3.2.3 Results from the load test

For different loads applied, the CODs measured by displacement sensors are listed in Table III. Distributed measurement was performed by PPP-BOTDA with 20cm SR. The BFS and BGSWD measured are shown in Figures 25-26.

Table III. CODs measured by displacement sensors under different loads (unit: mm)

Load (lbf)	CG2	CG3	CG1	CG4	Avg. of CGs 2&3	Avg. of CGs 1&4
60	22.20	36.78	36.76	32.92	29.49	34.84
100	40.74	62.97	61.24	50.63	51.86	55.93
140	64.58	97.98	96.27	75.15	81.28	85.71
180	93.80	135.70	128.03	103.40	114.75	115.72
230	135.03	185.46	169.18	136.71	160.25	152.95

The strain converted from measured BFS ($1\ MHz\ \cong 20\mu\varepsilon$) was mostly consistent with the theoretical strain for an intact beam (solid line in Figure 25(a)). The loads applied at the ends of the beam were not identical, which caused a small shear force in the beam segment between the two supports. Two peaks were located at 4.25m and 10.4m from the measured BFS, which corresponded to the two splices of the steel beam. The relationship between the amplitudes of the peaks from BFS and the CODs are shown in Figure 25 (b) for both splices. The amplitudes were positively related to the CODs.

The measured BGSWD under different loads are shown in Figure 26 (a). Similar to the measured BFS, two distinct peaks from the BGSWD corresponded to the splices of the beam. The noise level of BGSWD was higher compared to BFS. The amplitudes of the peaks versus the CODs measured by the FBG displacement sensors are shown in Figure 26(b). The amplitudes were positively related to the CODs. However, large discrepancies caused by measurement errors were found between the two splices under certain loads.

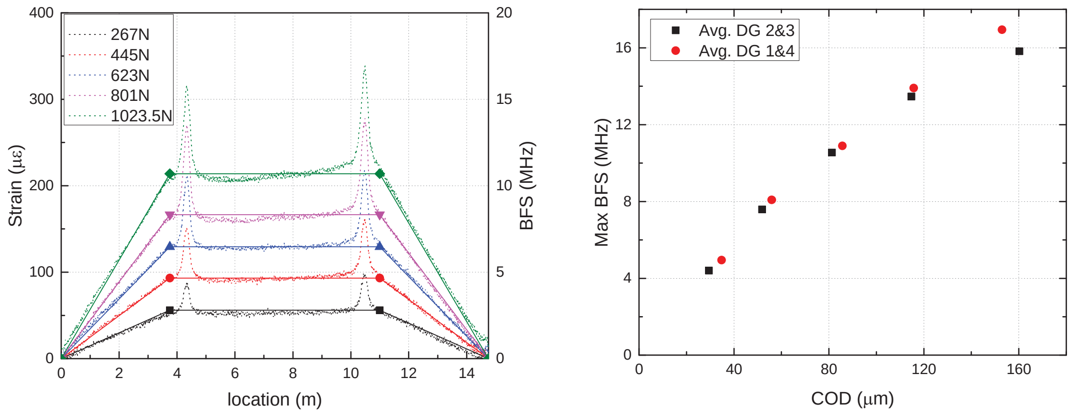

(a) Measured BFS (b) Max BFS measured at the splices

Figure 25. BFS measured from the load test

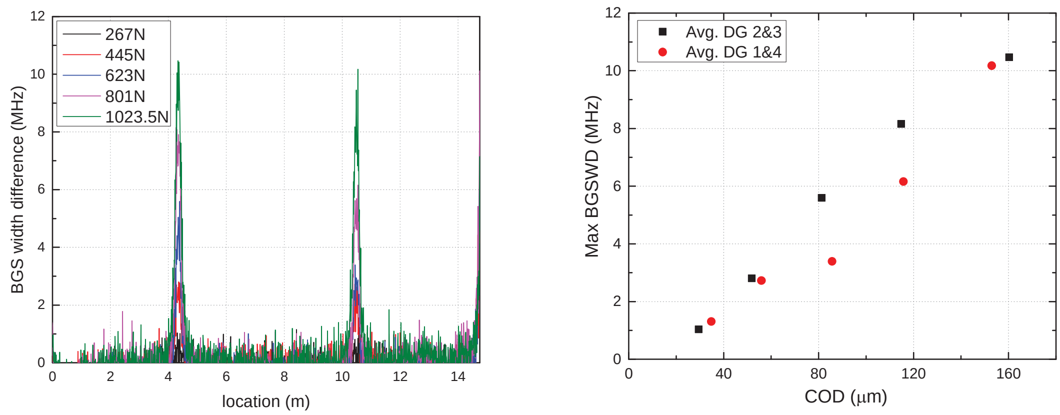

(a) Measured BGSWD (b) Max BGSWD measured at the splices

Figure 26. Measured BGSWD from the load test

3.2.4 Results summary

Two gaps opened at the splices of the steel beam during the four-point-bending test, which mimicked the widening of two cracks. They were successfully detected by two peaks from the measured BFS and BGSWD with 20cm SR. Positive relationships were found between the CODs and the amplitudes of peaks from BFS and BGSWD, indicating that BFS and BGSWD could also be utilized to monitor opening of cracks.

3.3 Load tests of RC beams

3.3.1 Introductions

Concrete has good compressive strength and is a very popular structural material due to its economy. However, concrete has low tensile strength, making it crack easily under tension. Reinforced concrete takes the advantages of the high tensile strength from steel reinforcement and good compressive strength from concrete. RC structures usually carry small cracks which don't affect the function of the structures. However, severe cracking may allow water and other hazard chemicals infiltration and cause the corrosion of the reinforcement, and lower the strength and stiffness of structural elements by destroying structural integrity. In this section, load tests of three RC beams were employed to test the performance of PPP-BOTDA distributed sensing in crack detection and monitoring on RC structural elements. The distributed sensors and FBG sensors were both embedded inside and installed on the surfaces of the RC beams. 20cm SR was employed for the distributed sensing due to its good performance in the steel beam test.

3.3.2 Load test of RC beam 1

3.3.2.1 Beam design and sensor installation

Dimensions and reinforcement layout of RC beam 1 are shown in Figure 27. The beam was 2.7 m long, 150 mm wide, 250 mm high, and the clear span was 2.5 m. The main steel reinforcement included two No.3 rebars for compression and two No.4 rebars for tension. The shear reinforcement included 35 hoops spacing at 75 mm, which were made of steel wires of 1/8 inch diameter. The concrete mix was of C30 grade (design strength of 4000 psi) with suggested water/concrete mix ratio 6.2-9.2 lbs / 80 lbs. The ratio of water/concrete mix for RC beam 1 was 9 lbs / 80 lbs.

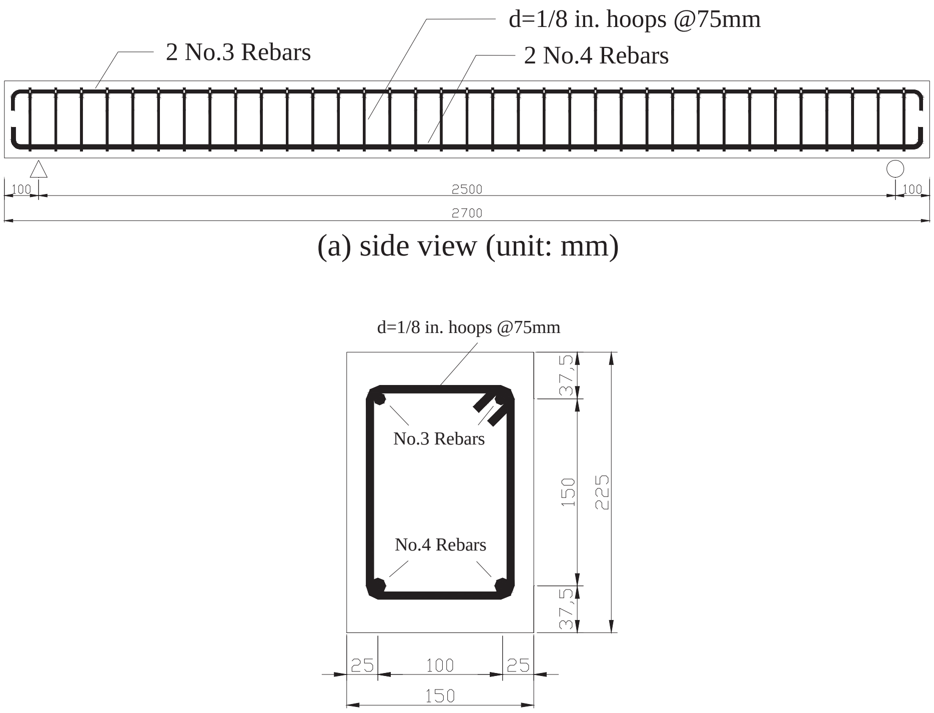

(a) side view (unit: mm)

(b) cross section view (unit: mm)

Figure 27. Dimensions and reinforcement layout of RC beam 1

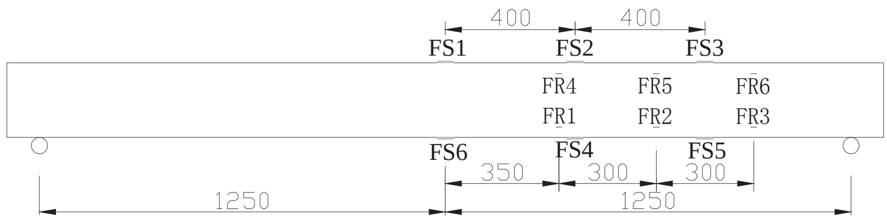

(a) side view (unit: mm)

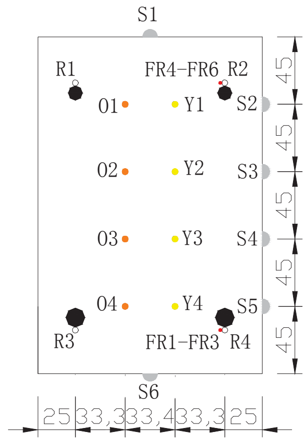

(b) cross section view (unit: mm)

Figure 28. Locations of the sensors

The locations of the distributed sensors and FBG sensors are shown in Figure 28. Beam fabrication and sensor installation were performed according to the following procedures. Distributed sensors R1-R4, O1-O4, Y1-Y4 and FBG sensors FR1-FR6 were embedded sensors and installed before concrete pouring. Before the installation of R1-R4 and FR1-FR6, a flat surface was created on each rebar by grinding off parts of the threads. SMF was tensioned and bonded to each rebar with 2-ton epoxy and named R1-R4. Six FBGs were also bonded to certain rebars with 2-ton epoxy and named FR1-FR6. The details of distributed sensors and FBG sensors are shown in Figure 29. The steel reinforcement cage was created after the sensors had been installed on the reinforcement, which is shown in Figure 30.

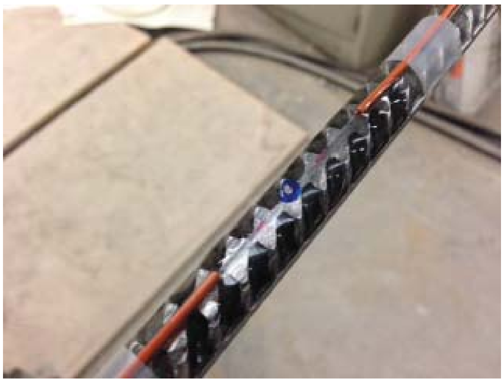

Figure 29. Details of distributed sensors and FBG sensors on reinforcement

Figure 30. The steel reinforcement cage

After the cage was in place, embedded distributed strain sensors O1-O4 and Y1-Y4 were passing through the cage. The locations of P1-P4 and Y1-Y4 are shown from the cross section view in Figure 28(b). The sensors O1-O4 were made of SMF bonded in peek tubes with 2-ton epoxy. The sensors Y1-Y4 were made of buffered SMF bonded in patch cords with 2-ton epoxy. Schemas of these sensors are shown in Figure 31. They were tensioned at both ends to keep the geometry a straight line during concrete pouring, which is shown in Figure 32.

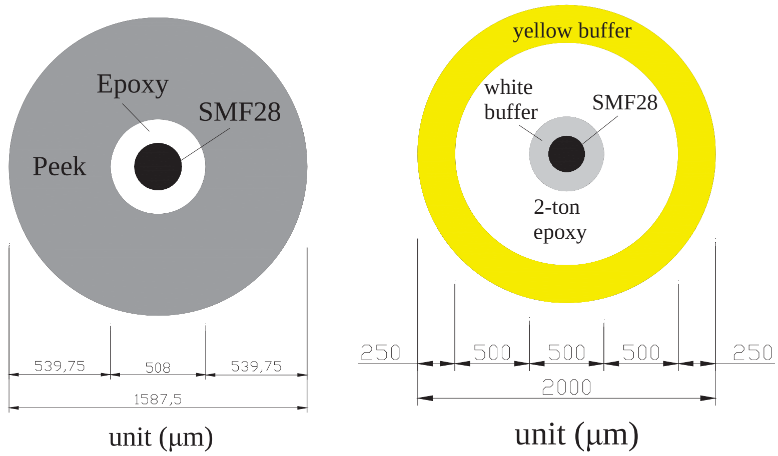

Figure 31. Schemas of O1-O4 (left) and Y1-Y4 (right)

Figure 32. Tension of P1-P4 and Y1-Y4 at both ends

After concrete pouring was finished, the specimen was cured in moisture for the first week and cured in the air for the next two weeks. The forms were stripped off after three weeks from concrete pouring, and the surface-attached distributed sensors and FBG strain gauges were installed, which can be seen in Figure 33. The distributed sensors S1 – S6 were made of SMF tensioned and bonded to the surfaces of the beam with silicon rubber adhesive. Their locations can be seen from the cross section in Figure 28(b). FBG strain gauges FS1-FS6 were installed on the top surface and bottom surface, and their locations are shown in Figure 28(a).

Figure 33. Installation of surface-attached sensors

3.3.2.2 <u>Load test</u>

Four-point-bending test were performed on RC beam 1 in the lab. The test setup is shown in Figure 34. The clear span of the RC beam was 2.5m, and the 1m long segment at the mid span of the beam was under pure bending. Before the load test, concrete cylinder tests were performed and the results are shown in Table IV.

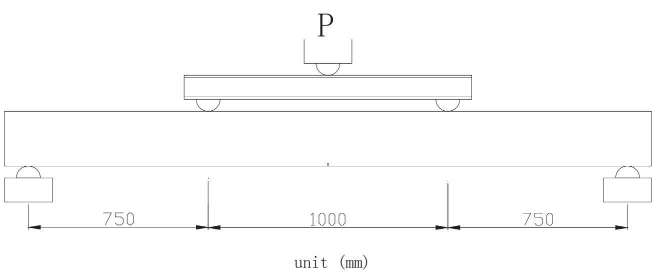

(a) Schema (b) picture

Figure 34. Four point bending test setup

Table IV. Results from concrete cylinder tests

Specimen number	No.1	No.2	Average
Ultimate load (lb)	180795	151100	165948
Ultimate stress (psi)	6395	5345	5870

According to ACI 318 (110), the Young's modulus of the concrete was estimated at $4367.1\ \mathrm{ksi}$ $(30.11\ \mathrm{GPa})$ based on the average compressive strength of $5870\ \mathrm{psi}$ $(40.47\ \mathrm{MP}a)$ from the cylinder tests. The rapture strength of concrete was estimated about $574.6\ \mathrm{psi}\ (3.96\ \mathrm{MPa})$. As a result, the cracking strain for the concrete was about $131.5\mu\varepsilon$. According to the beam design and material properties, the cracking load of RC beam 1 was estimated about 2800 lbs (12.5 kN), and the ultimate load was about 12810 lbs (57 kN). The calculations can be referred to Appendix B.

The load test of RC beam 1 was performed in three cycles to introduce damages of different levels to the beam. In load cycle 1, the beam was loaded from 0 to 2000 lbs, and only minor damages were expected in the beam. The beam was loaded from 0 to 4000lbs in load cycle 2, and major cracking was expected when the load was beyond the estimated cracking load. The beam was loaded from 0 to 7000lbs in load cycle 3, and then loaded to failure.

The load – deflection curve of RC beam 1 is shown in Figure 35. The slope changed obviously under the loads of 2000 lbs and 16000 lbs, corresponding to the cracking load and ultimate load of the beam.

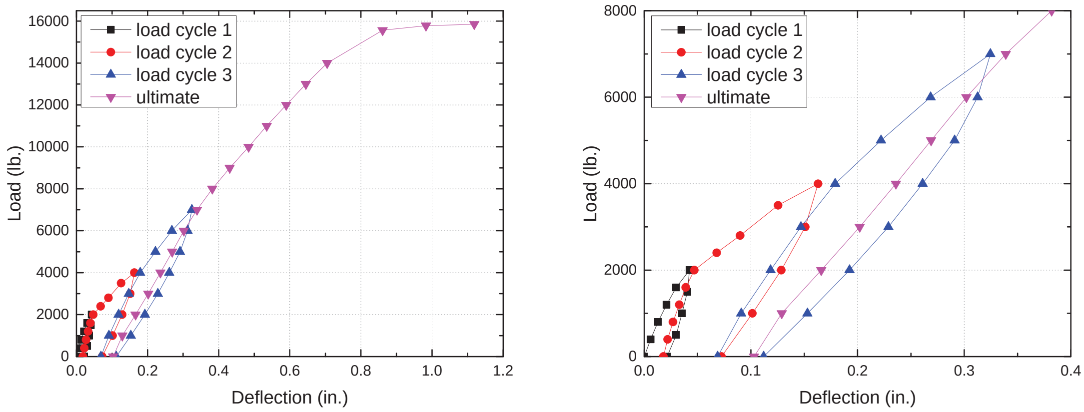

(a) Overall (b) details of load cycles 1-3

Figure 35. Load-deflection curve of RC beam 1

3.3.2.3 Results from S6

The distributed sensor S6 was adhered to the tension surface of the beam. The BFS and BGSWD measured by S6 with 20cm SR are shown in Figures 36-37. The state of the beam before the load test was chosen as the reference.

As is shown in Figure 36, The BFS increased rapidly between the loads of 2000 lbs and 2800lbs, indicating cracking initially took place in load cycle 2. Under the load of 2800 lbs, one major peak was found at 1.55m, and one minor peak was found at 1.15m. When the load was increased to 4000 lbs, peaks can be found at 0.85m, 1.15m and 1.55m. Under the load of 6000 lbs in load cycle 3, a new peak was found at 1.9m. The amplitude of each peak was positively related to the load applied to the beam. However, none of the peaks matched with cracks located by visual inspections after the load test.

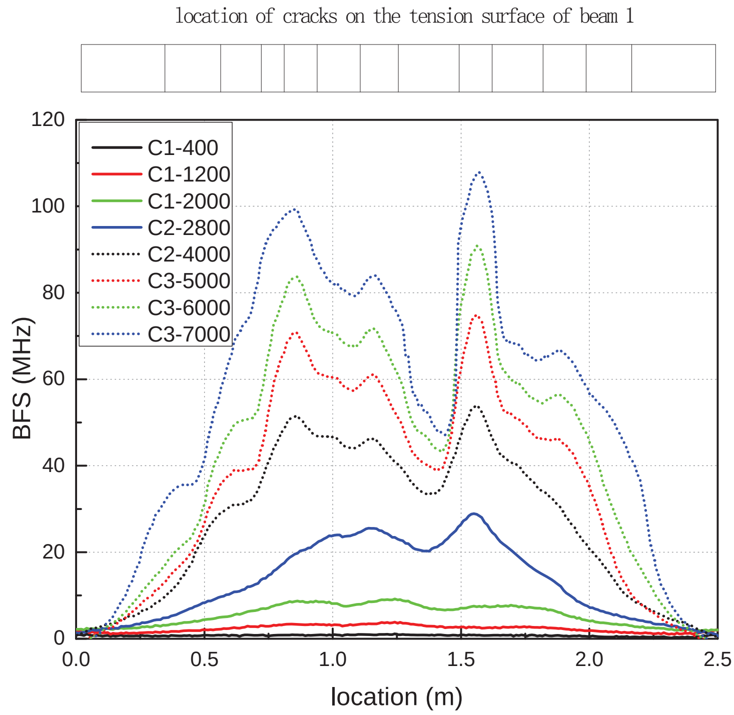

Figure 36. BFS measured from S6

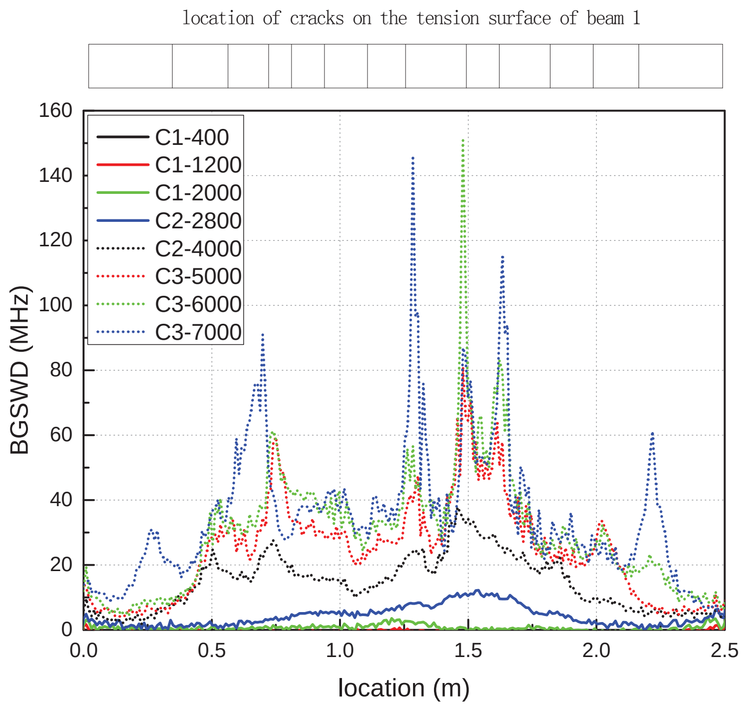

Figure 37. BGSWD measured from S6

As is shown in Figure 37, the BGSWD started increasing under the load of 2800 lbs in load cycle 2. Under the load of 4000 lbs, a few peaks were recognized at 0.72m, 1.3m and 1.45m. Under the load of 5000 lbs in load cycle 3, the peaks were found at 0.72m, 1.3m, 1.48m and 1.6m. Under the load of 7000 lbs, major peaks were found at 0.28m, 0.7m, 1.3m, 1.48m, 1.62m, and 2.22m. Usually, the amplitude of the peak was positively related to the load applied to the beam. Compared to BFS, some of the peaks matched with or located close to the cracks on the beam.

The results from sensor S6 are summarized in Table V. A few cracks were detected by BGSWD only. Generally, BFS and BGSWD increased with the load applied to the beam. However, as the information of CODs was not available, the relationship between the peak amplitude and the COD was not provided.

Table V. Location of cracks on RC beam 1

Locations of cracks (m)	0.33	0.55	0.7	0.8	0.93	1.09	1.25	1.49	1.62	1.82	1.98	2.16
Detected by BFS												
Detected by BGSWD			√				√	√	√			

3.3.3 **Load test of RC beam 2**

3.3.3.1 **Beam design and sensor installation**

The structural design of RC beam 2 was same to RC beam 1 and can be referred to Section 3.3.2.1. The sensors layout was altered and locations of different sensors are shown in Figure 38. The distributed sensors Y1 – Y4 were replaced due to poor performances from previous load test. Instead, six distributed sensors O1 – O6 were embedded in RC beam 2. Five FBGs FR1 – FR5 were installed on the main reinforcement, and their locations can be seen from Figure 38. S1 – S7 were seven distributed sensors installed on the surfaces of the beam, and their locations were shown in Figure 38(b). The locations of surface-installed FBG strain sensors FS1 – FS6 were altered and can be seen in Figure 38.

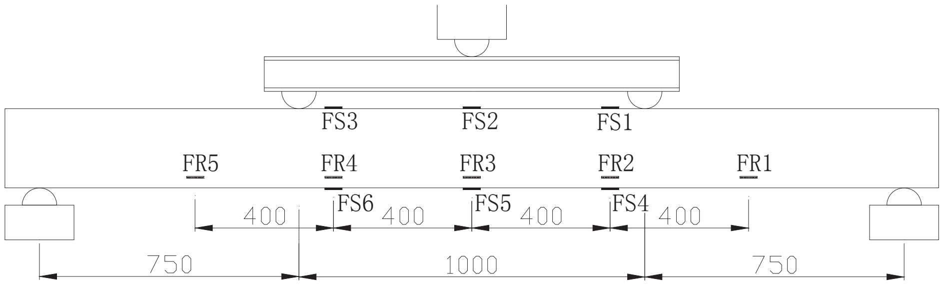

(a) Side view (unit: mm)

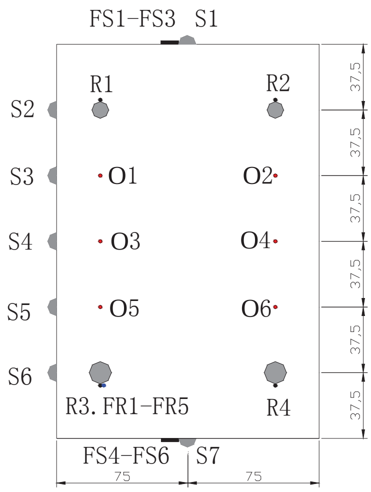

(b) Cross section view (unit: mm)

Figure 38. Locations of sensors on RC beam 2

3.3.3.2 Load test

The water/concrete mix ratio was 6.5 lbs / 80 lbs, which was close to the lower bound of the suggested value. The results of concrete cylinder test are listed in Table VI. The average compressive strength is 7750 psi (53.43 MPa). Young's modulus and rapture strength of the concrete was estimated at 5017.9 ksi (34.6 GPa) and 660.3 psi (4.55 MPa), respectively. Based on the beam design and material properties, the cracking load of RC beam 2 was estimated about 2800 lbs, and the ultimate load was about 12840 lbs (57.1 kN). The calculation can be referred to Appendix B.

Table VI. Results of concrete cylinder tests for RC beam 2

Specimen	No.1	No.2	No.3	Average
Ultimate load (lb)	203420	232735	221220	219125
Ultimate stress (psi)	7195	8230	7825	7750

The load test of RC beam 2 was performed in two load cycles with ranges of 0-2000 lbs and 0-4000 lbs. After load cycle 2, the beam was loaded to failure under the load of 14000 lbs. The load-deflection curves are shown in Figure 39. The slope first changed after 1200 lbs in load cycle 1, indicating initial cracking in the beam.

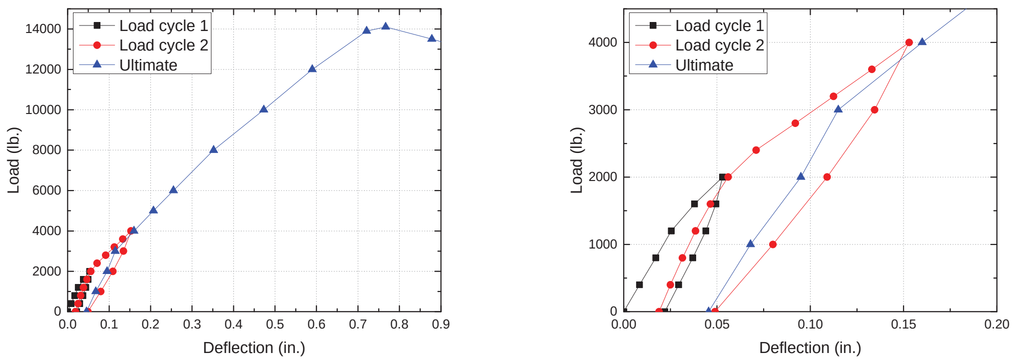

(a) Overall (b) Details of load cycles 1-2

Figure 39. load-deflection curve of RC beam 2

3.3.3.3 Results from S7

The distributed sensor S7 was adhered to the tension surface of RC beam 2. The BFS and BGSWD measured by S7 are shown in Figures 40 - 41.

As is shown in Figure 40, a few minor peaks were found from the BFS under the load of 2800 lbs in load cycle 2. When the load was increased to 4000 lbs, peaks can be clearly recognized at 0.75m, 0.88m, 1.05m, 1.35m, 1.65m and 1.78m. No more peaks were found from BFS when the load was larger than 4000 lbs in load cycle 3. The amplitude of each peak was positively related to the load applied to the beam.

As is shown in Figure 41, the BGSWD started to change under the load of 2800 lbs in load cycle 2. Under the load of 4000 lbs, a few peaks can be recognized at 0.7m, 0.9m, 1.05m, 1.6m and 1.7m. When the load was increased to 6000 lbs in load cycle 3, new peaks were recognized at 1.4m, and 2.1m. Under the load of 8000 lbs, major peaks were found at 0.42m, 1.22m, 1.45m, and 2.1m. In addition, there were many minor peaks that were difficult to distinguish from noise, which may indicate less integrity of RC beam 2.

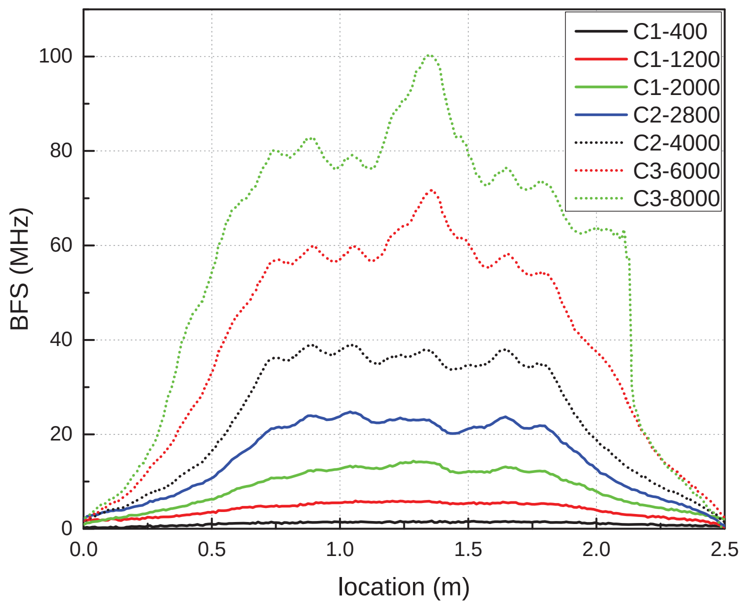

Figure 40. BFS measured from S7

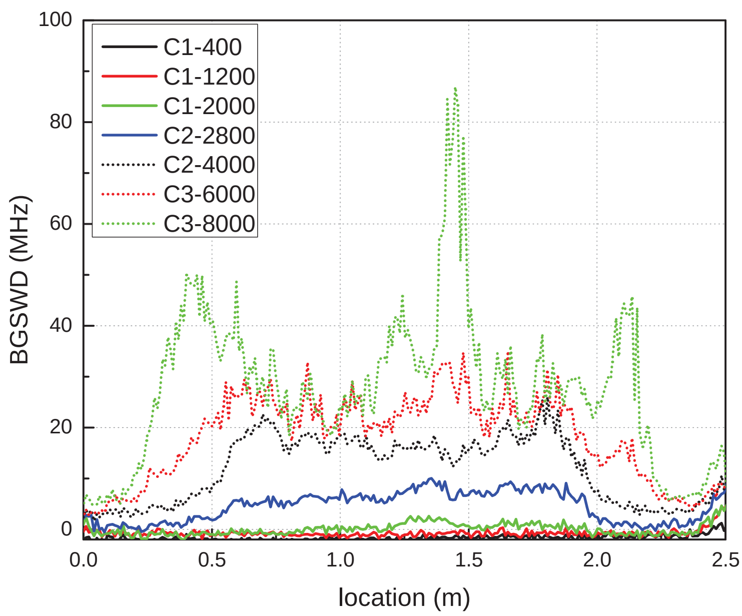

Figure 41. BGSWD measured from S7

The surfaces of RC beam 2 were very coarse due to the low water/mix ratio, and visual inspections failed to recognize any cracks from the surface.

3.3.4 <u>Load test of RC beam 3</u>

3.3.4.1 <u>Beam design and sensor installation</u>

The dimensions and reinforcement layout of RC beam 3 can be referred to RC beam 1 in Section 3.3.2.1. Locations of the sensors installed in and on RC beam 3 are shown in Figure 42. Compared to RC beam 2, only locations of P1 – P6 were altered.

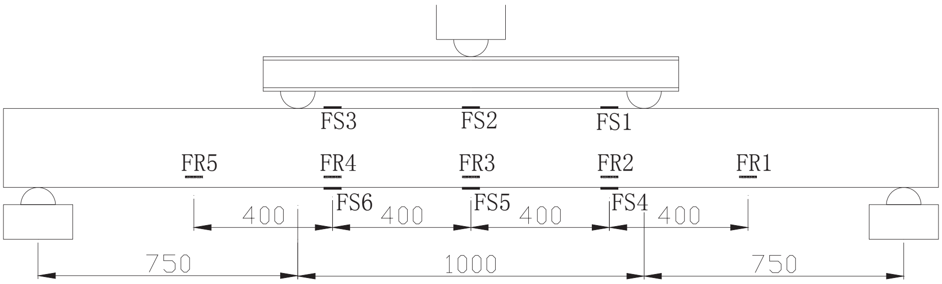

(a) Side view (unit: mm)

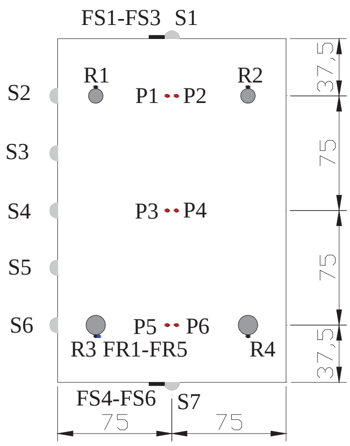

(b) Cross section view (unit: mm)

Figure 42. Locations of sensors on RC beam 3

3.3.4.2 Load test

The results of concrete cylinder tests are listed in Table VII. The average compressive strength from the cylinder tests was 6220 psi (42.88 MPa). Based on calculations according to ACI 318, modulus of elasticity was 4495.4 ksi (30.99 GPa), and the rapture strength of concrete was 591.5 psi (4.08 MPa). The cracking load was estimated about 2800 lbs, and the ultimate load was about 12775 lbs (56.8 kN). The calculations can be referred to Appendix B.

Table VII. Results of concrete cylinder tests for RC beam 3

Specimen	No.1	No.2	No.3	Average
Ultimate load (lb)	165135	165395	197010	175850
Ultimate stress (psi)	5840	5850	6965	6220

The load test of RC beam 3 was performed in two cycles with ranges of 0-2000 lbs and 0-4000 lbs. After load cycle 2, the beam was loaded to failure around 17000 lbs. The load-deflection curve is shown in Figure 43. The slope first changed under the load of 2800 lbs, indicating initial cracking of the beam.

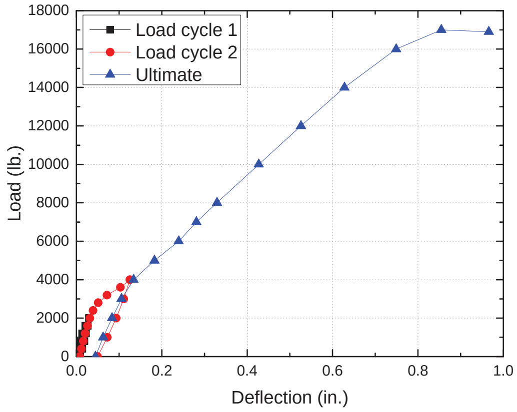

(a) Overall

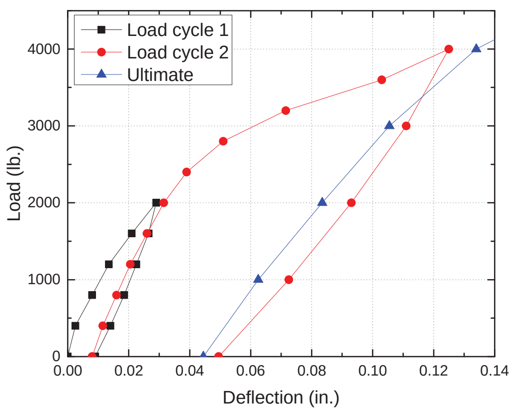

(b) details of load cycles 1-2

Figure 43. Load-deflection curve of RC beam 3

3.3.4.3 Results from S7

The distributed sensor S7 was adhered to the tension surface, and the measured BFS and BGSWD from S7 are shown in Figures 44 - 45.

As is shown in Figure 44, a rapid increase in the BFS between the loads of 2800 lbs and 4000 lbs in load cycle 2 indicated initial cracking in the beam. Under the load of 4000 lbs, a few peaks can be vaguely recognized from BFS at 1.15m, 1.32m, 1.48m, and 1.7m. When the load was increased to 6000 lbs and 8000 lbs in load cycle 3, major peaks can be found at 0.7m, 1.08m, and 1.7m. However, none of the major peaks matched with the crack detected from visual inspections after the load test. Locations of the cracks are listed in Table VIII.

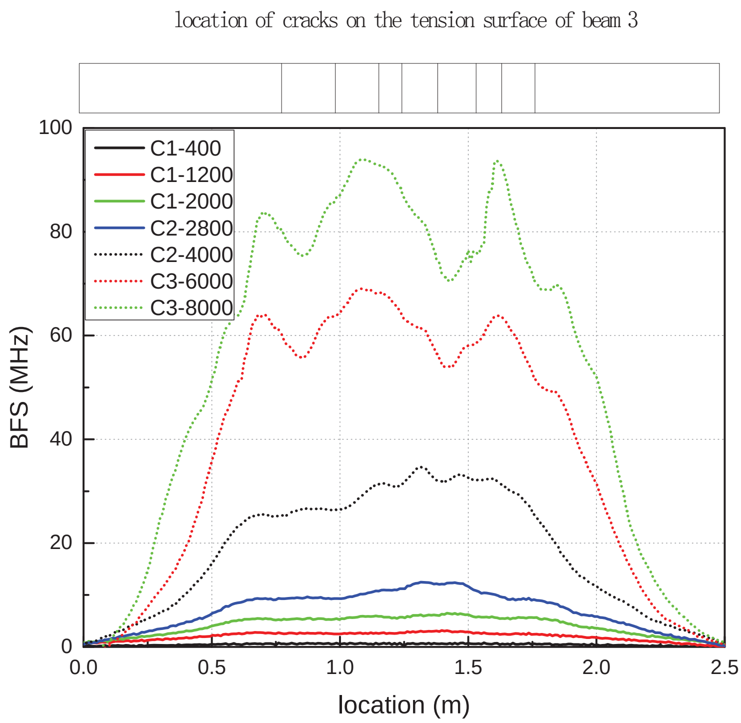

Figure 44. BFS measured from S7

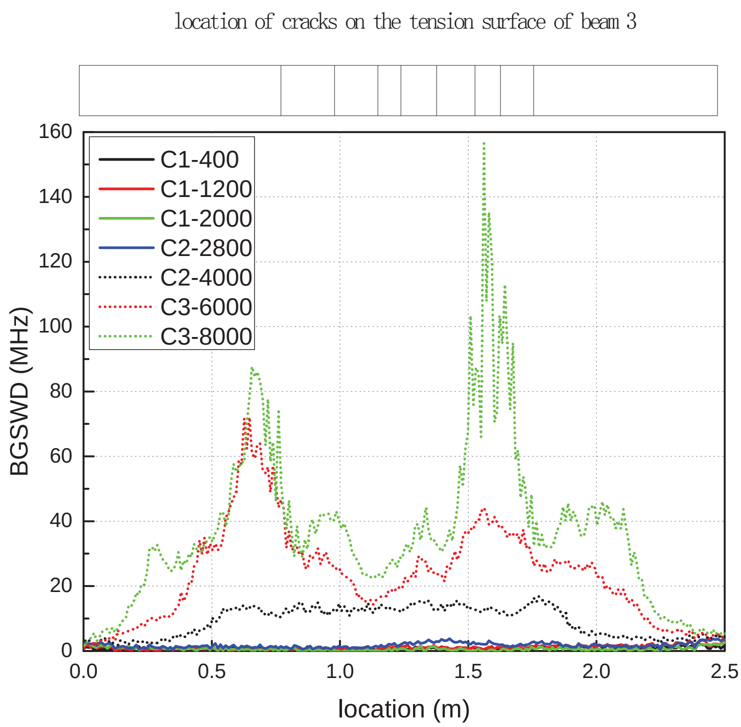

Figure 45. BGSWD measured from S7

As is shown in Figure 45, the BGSWD first had an obvious change under the load of 4000 lbs in load cycle 2. However, the BGSWD increased evenly over the pure bending segment, and it was difficult to locate any peaks except the one at 1.8m. Under the load of 6000 lbs in load cycle 3, major peaks were recognized at 0.65m, 1.33m and 1.56m. When the load was increased to 8000 lbs, major peaks were found at 0.65m, 0.95m, 1.33m, 1.5m, 1.56m, 1.64m, 1.9m, and 2.0m. Among all the peaks recognized from the BGSWD, only the peaks at 1.56m and 1.64m matched with the crack location from visual inspection.

The results from sensor S7 are summarized in Table VIII. Only two cracks were detected by BGSWD. Generally, BFS and BGSWD increased with the load applied to the beam. Since few cracks were detected by the distributed sensor, no relationship between the peak amplitude and the COD was provided.

Table VIII. Location of cracks on RC beam 3 from visual inspection

Locations of cracks (m)	0.8m	1.01m	1.18m	1.26m	1.4m	1.56m	1.64m	1.79m
Detected by BFS								
Detected by BGSWD						√	√	

3.3.4 Results summary

Changes were shown from BFS and BGSWD measured by PPP-BOTDA distributed sensors installed on RC beams 1 – 3 due to cracks developing in the beams during the load tests. With 20cm SR employed in the test, peaks were recognized from BFS and BGSWD when the applied load was larger than the cracking load for each beam. And the amplitudes of the peaks were positively related to the load applied to the beam. However, the peaks from BFS did not match with the cracks detected from visual inspections, and the peaks usually appeared between two cracks. A few peaks from BGSWD matched with or were close to the locations of cracks detected from visual inspections.

3.5 Summary

Four-point-bending tests were performed on a steel beam and three RC beams. PPP-BOTDA distributed sensors were employed to detect and monitor the cracks developed in the beams during the load tests.

In the load test of the steel beam, two cracks at the splices were successfully detected as two peaks from the BFS and BGSWD measured by the PPP-BOTDA distributed sensor with 20cm SR. Positive relationship was found between the CODs at the splices and the amplitudes of the peaks from BFS and BGSWD. Compared to BFS, BGSWD was of a higher noise level and less sensitive to small CODs.

In the load tests of RC beams 1 – 3, multiple cracks appeared on the beams when the applied load was beyond the cracking load. However, crack detection and monitoring based on PPP-BOTDA distributed sensing with 20cm SR was not very successful. Most peaks recognized from BFS and BGSWD did not match with the cracks detected from visual inspections after the load tests. The peaks found from BFS usually located between cracks, and a few peaks found from BGSWD matched with or closely located to the cracks from visual inspections.

4. CAPABILITY OF PPP-BOTDA IN DIFFERENTIATING CRACKS

4.1 Introductions

Cracks usually appear in groups on concrete structures due to the low tensile strength of concrete. The unsuccessful experiences from the load tests of RC beams 1-3 indicated that there was a limit for PPP-BOTDA in differentiating neighboring cracks. In chapter 2, SR was shown as an important factor affecting the performance of PPP-BOTDA in single-crack detection. In order to study the capability of PPP-BOTDA in differentiating neighboring cracks, a series of dual-crack cases were employed considering different SRs and crack spacing.

Following a similar research schema of the single-crack case, distributed strain in a sensing fiber traversing two cracks were analyzed theoretically based on the strain transfer mechanism. The distributed strain acquired from theoretical analysis was then employed as the input of numerical simulation. Different spatial resolutions were considered in the numerical simulation. Changes in BGS due to the crack-induced strain were characterized by BFS and BGSWD along the distributed sensor. Experimental research was carried out with a PPP-BOTDA device (NBX-6055) through a series of dual-crack tests. Results from the numerical simulation and the tests were employed to evaluate the performance of PPP-BOTDA in differentiating neighboring cracks.

4.2 Theoretical strain analysis for the dual-crack case

4.2.1 Strain analysis based on superposition

The superposition principle (111) states that the response caused by two or more stimuli is the sum of the responses which would have been caused by each stimulus individually. The principle only works for linear systems. If the induced strain is considered as a linear response for a dual-crack case, the strain can be acquired as superposition of strains induced by each crack individually. For the dual case shown in Figure 46, with CODs $2\delta_1$ at $z = z_1$ and $2\delta_2$ at $z = z_2$ ($z_1 < z_2$), the induced strains in the sensing fiber can be expressed by Equation 4.1.

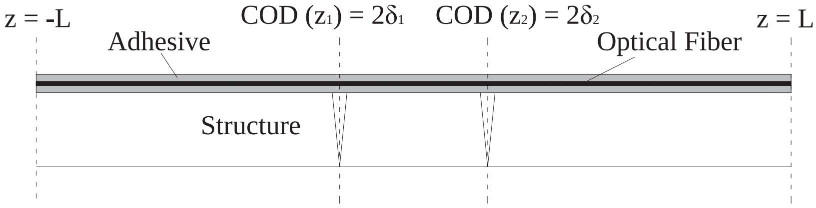

Figure 46. Schema of the dual-crack case

$$\varepsilon(z) = \begin{cases} \delta_1\beta exp[\beta(z - z_1)] + \delta_2\beta exp[\beta(z - z_2)] & z < z_1 < z_2 \\ \delta_1\beta exp[-\beta(z - z_1)] + \delta_2\beta exp[\beta(z - z_2)] & z_1 < z < z_2 \\ \delta_1\beta exp[-\beta(z - z_1)] + \delta_2\beta exp[-\beta(z - z_2)] & z_1 < z_2 < z \end{cases} \tag{4.1}$$

where β is the shear lag factor defined in chapter 2.

4.2.2 <u>Comparisons between strains from theoretical analysis and FEA</u>

Similar to the single-crack case, the dual-crack case was modeled in ANSYS and FEA was performed. The same shear lag factor was obtained by choosing the geometric and material properties from the single-crack case. Considering the dual-crack case with two CODs $2\delta_1 = 2\delta_2 = 100\mu m$ at $z_1 = -10cm$ and $z_2 = 10cm$ (20cm crack spacing), the strains in the fiber core obtained from theoretical analysis and FEA are shown in Figure 47. The biggest difference was 4.1% (2256με vs. 2167με) and occurred at the crack locations. With the strain derived from theoretical analysis as input, numerical simulation was performed for different dual-crack cases and presented in the next section.

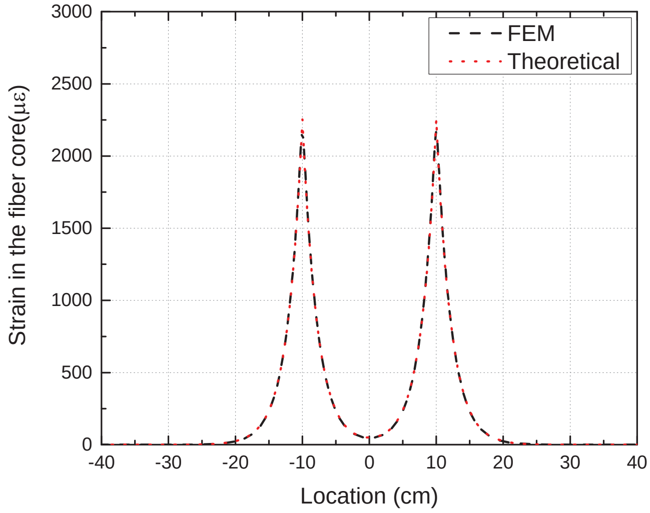

Figure 47. Strains from theoretical analysis and FEA for the dual-crack case

4.3 Numerical simulation

4.3.1 Cases under study

Numerical simulation for the single-crack case showed that a crack can be detected as a peak from BFS and BGSWD by PPP-BOTDA. For the dual-crack case, similar characters in BFS and BGSWD were expected. As the SR was considered a major factor affecting the performance of PPP-BOTDA in differentiating neighboring cracks, different SRs and crack spacing were employed to create cases to study, which are listed in Table IX. CODs up to 200 μm are assigned to both cracks. The input strains considering different crack spacing are shown in Figure 48. The BFS and BGSWD were outputted at every 1cm.

Table IX. Cases for numerical simulation
(√ for considered, - for unconsidered)

Crack spacing (cm)		50cm	20cm	10cm
	50cm	√	√	-
Spatial resolution (cm)	20cm	√	√	√
	10cm	√	√	√

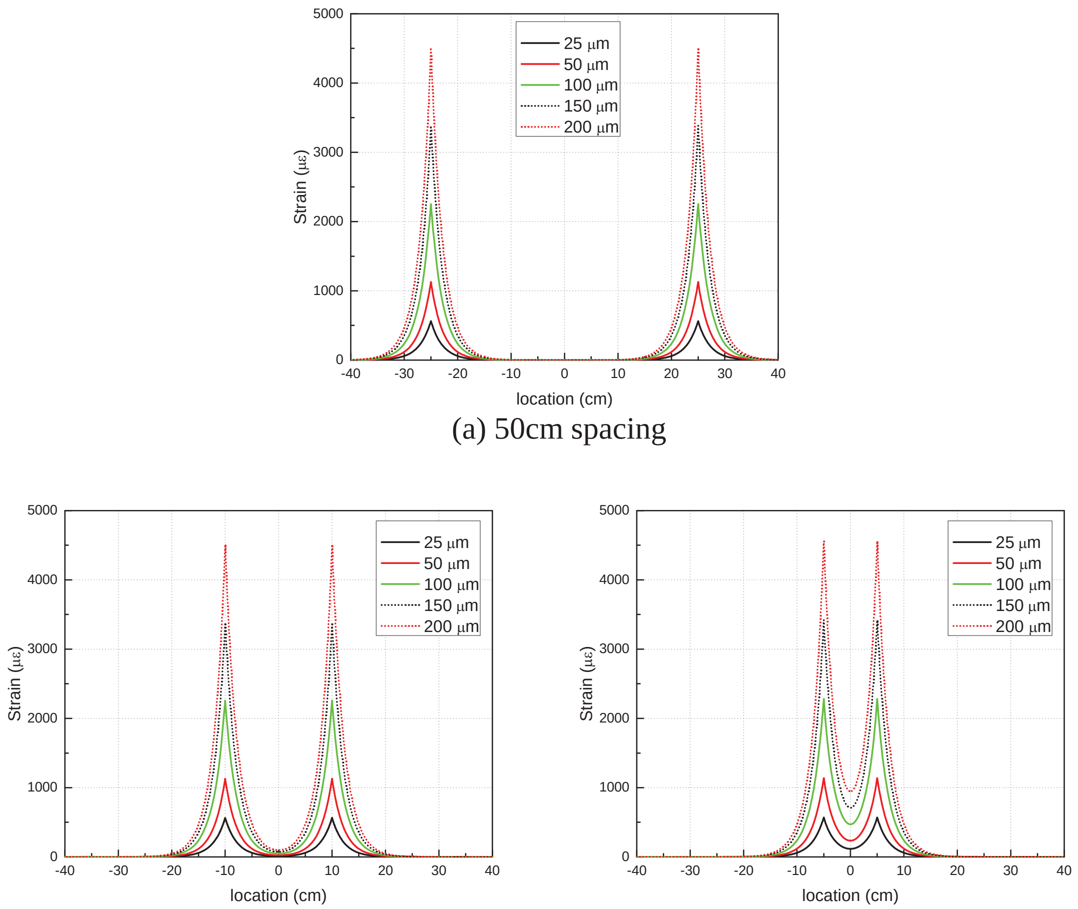

(a) 50cm spacing

(b) 20cm spacing

(c) 10cm spacing

Figure 48. Input strains for numerical simulation

4.3.2 Results from Numerical simulation

The BFS and BGSWD obtained from numerical simulation are shown in Figures 49 – 54 for cases of different crack spacing.

4.3.2.1 50cm crack spacing

The BFS and BGSWD obtained from numerical simulation for the case of 50cm crack spacing are shown in Figure 49. The two cracks (located at -25cm and 25cm) were recognized as two distinct peaks from the BFS and BGSWD by PPP-BOTDA with 50cm, 20cm and 10cm SRs. Similar to the single crack case, the BFS and BGSWD were not symmetric to the crack locations, and the peaks were not at the exact locations of the cracks.

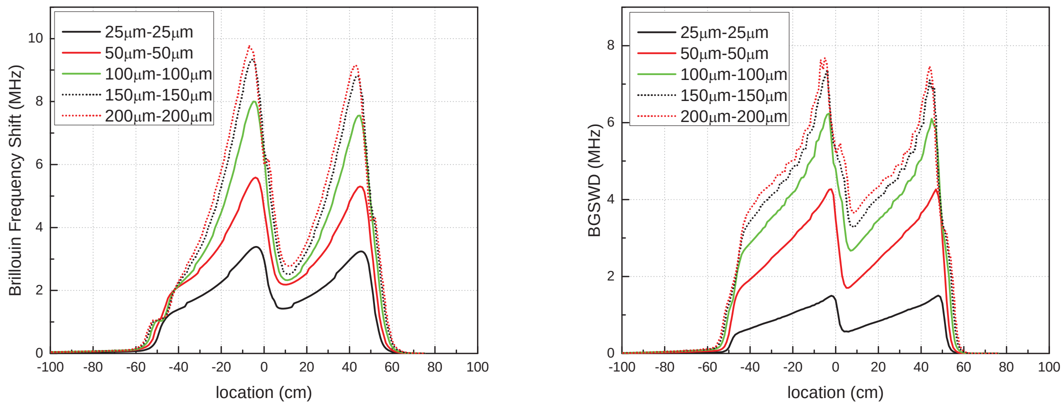

(a) 50cm SR

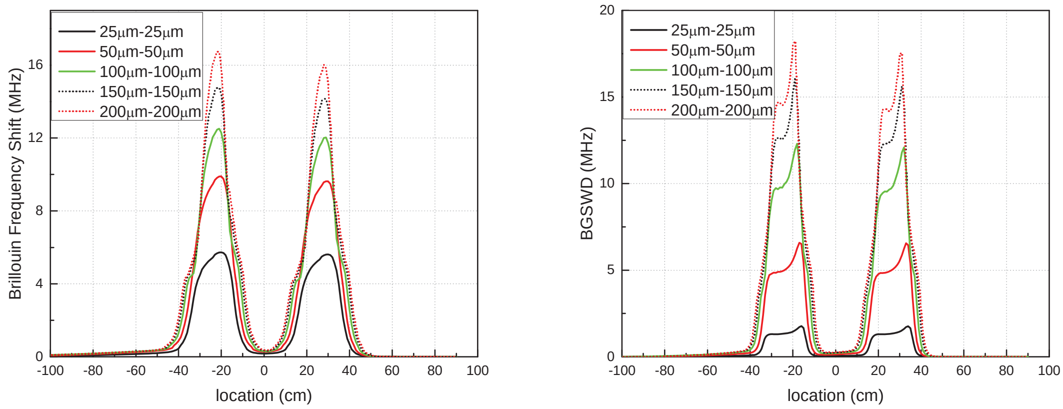

(b) 20cm SR

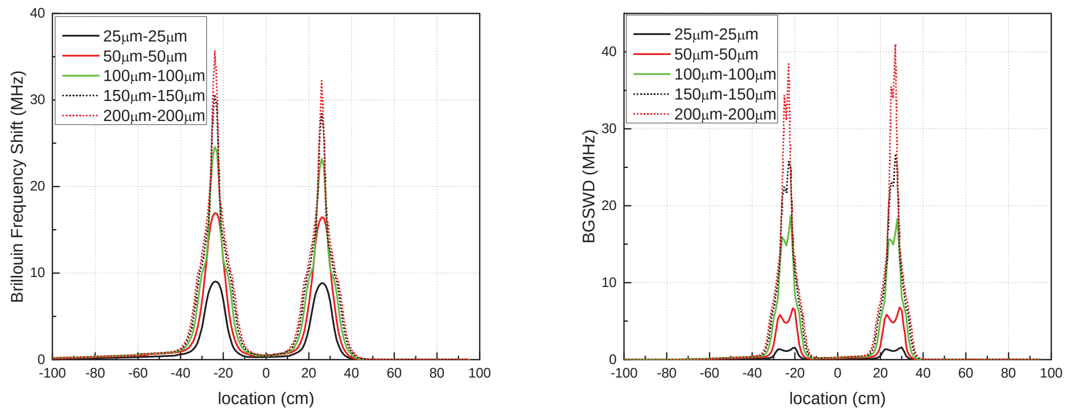

(c) 10cm SR

Figure 49. BFS and BGSWD from numerical simulation for 50cm crack spacing

For each crack, the amplitudes of BFS and BGSWD from the dual-crack case are shown in Figure 50 (a)-(b), and their ratios to the amplitudes from the single-crack case are shown in Figure 50 (c)-(d). Similar to the single-crack case, the amplitudes from the dual-crack case increased with the COD. When 50cm or 20cm SR was employed, the amplitudes of BFS and BGSWD tended to stop growing as the COD was increased to 200 μm. No obvious difference was shown between the amplitudes from the dual-crack case and from the single-crack case.

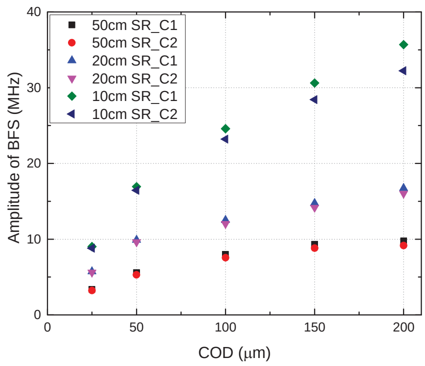

(a) BFS

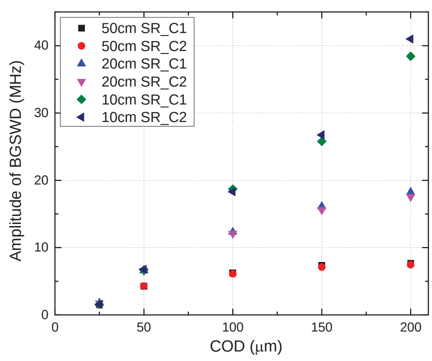

(b) BGSWD

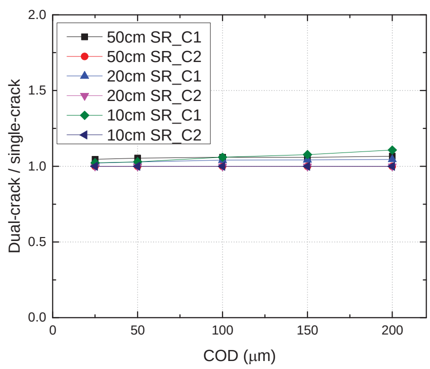

(c) Ratio of BFS

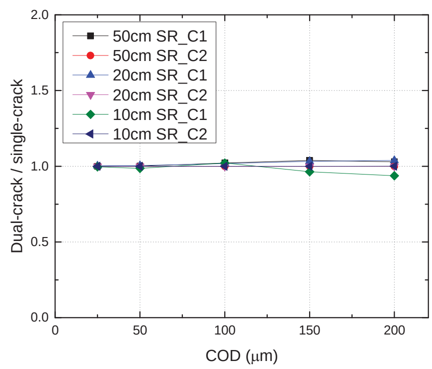

(d) Ratio of BGSWD

Figure 50. Amplitudes from numerical simulation for 50cm crack spacing

The affected lengths of BFS and BGSWD from the dual-crack case are shown in Figure 51 (a)-(b), and their ratios to the affected lengths from the single-crack case are shown in Figure 51 (c)-(d). Similar to the single-crack case, the averaged affected lengths decreased with an improved SR. The affected lengths from the dual-crack case were similar to those from the single-crack case.

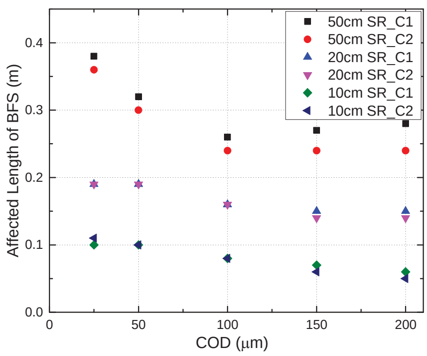

(a) BFS

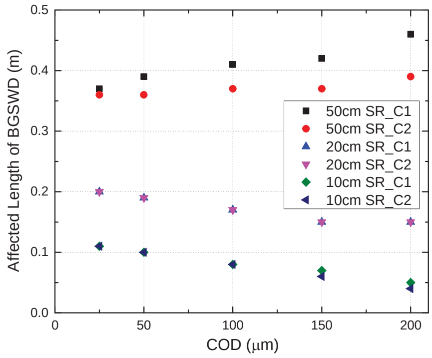

(b) BGSWD

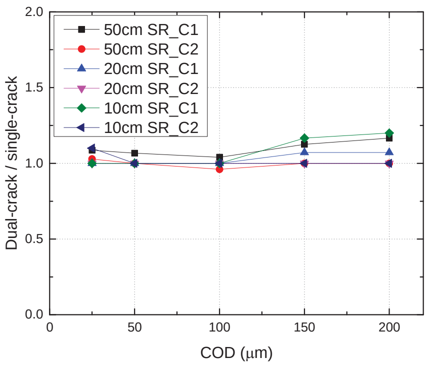

(c) Ratio of BFS

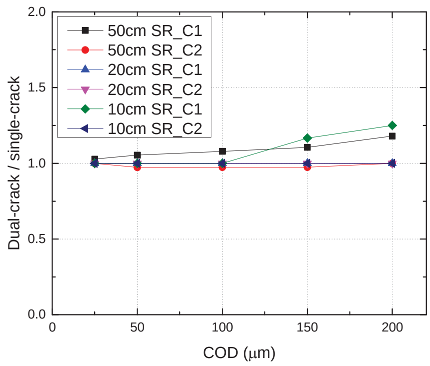

(d) Ratio of BGSWD

Figure 51. Affected lengths from numerical simulation for 50cm crack spacing

4.3.2.2 20cm crack spacing

The BFS and BGSWD obtained from numerical simulation for the case of 20cm crack spacing are shown in Figure 52. When 50cm and 20cm SRs were employed, the cracks (located at -10cm and 10cm) could not be recognized as two distinct peaks from BFS or BGSWD. Instead, one major peak emerged between the cracks with 50cm SR, and a relatively flat top appeared between the cracks with 20cm SR. When 10cm SR was employed, the cracks were recognized as two distinct peaks from the BFS and BGSWD.

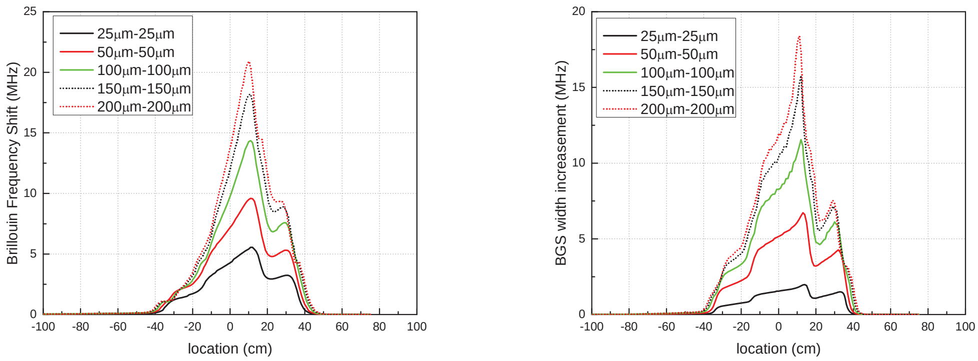

(a) 50cm SR

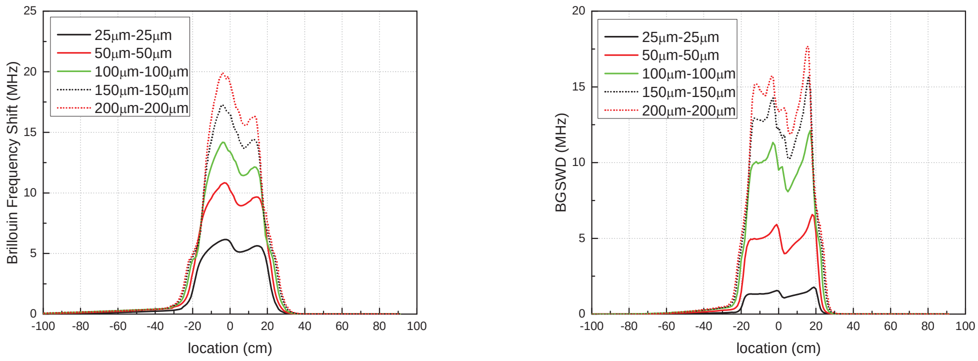

(b) 20cm SR

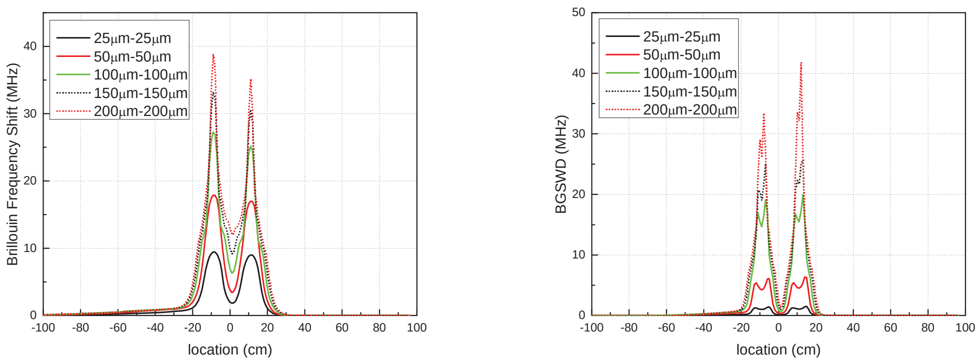

(c) 10cm SR

Figure 52. BFS and BGSWD from numerical simulation for 20cm crack spacing

The amplitudes of BFS and BGSWD from the dual-crack case are shown in Figure 53 (a)-(b), and their ratios to amplitudes from the single-crack case are shown in Figure 53 (c)-(d). When 50cm SR was employed, the amplitudes of BFS and BGSWD were larger compared to the single-crack case. When 20cm or 10cm SR was employed, the amplitudes of BFS and BGSWD from the dual-crack case were similar to the single-crack case.

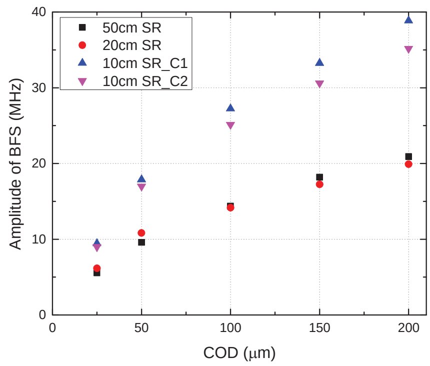

(a) BFS

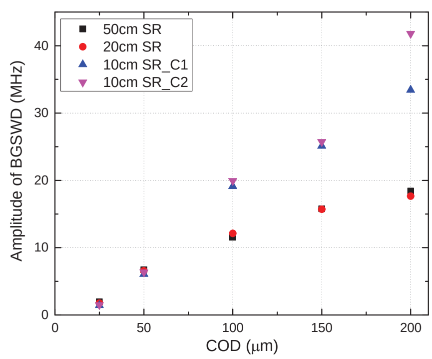

(b) BGSWD

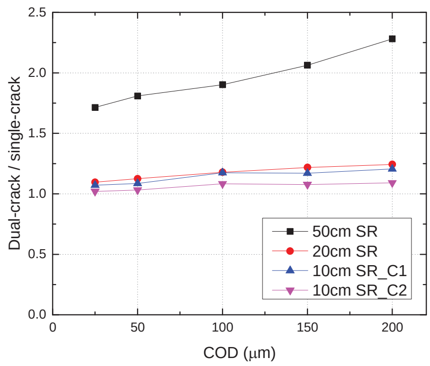

(c) Ratio of BFS

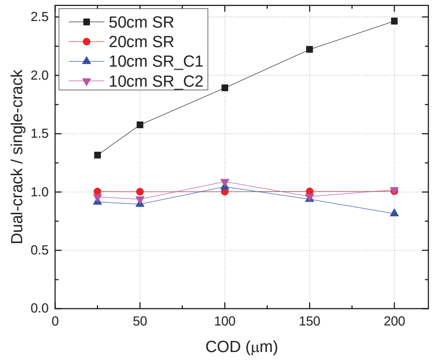

(d) Ratio of BGSWD

Figure 53. Amplitudes from numerical simulation for 20cm crack spacing

The affected lengths of BFS and BGSWD from the dual-crack case are shown in Figure 54 (a)-(b), and their ratios to the affected lengths from the single-crack case are shown in Figure 54 (c)-(d). Compared to the single-crack case, the affected lengths were much larger when 20cm SR was employed. When 50cm or 10cm SR was employed, the affected lengths from the dual-crack case were similar to the single-crack case.

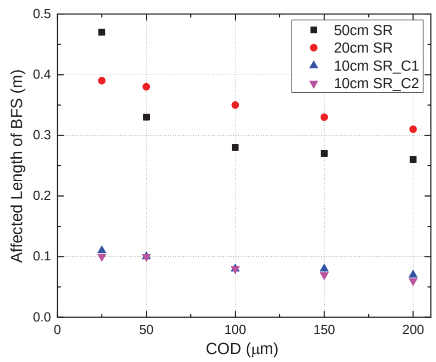

(a) BFS

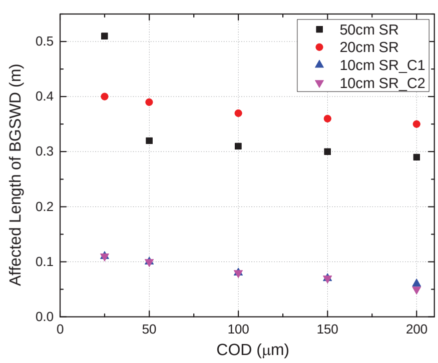

(b) BGSWD

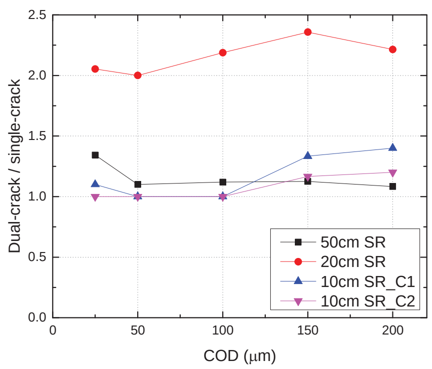

(c) Ratio of BFS

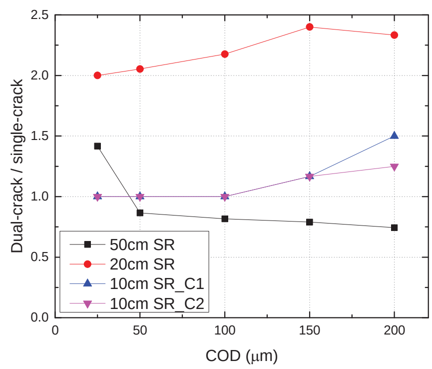

(d) Ratio of BGSWD

Figure 54. Affected lengths from numerical simulation for 20cm crack spacing

4.3.2.3 <u>10cm crack spacing</u>

The BFS and BGSWD obtained from numerical simulation for the case of 10cm crack spacing are shown in Figure 55. Only 20cm and 10cm SRs were employed by numerical simulation in view of the small spacing. One major peak was recognized between the two cracks (located at -5cm and 5cm) from the BFS, while the variation in BGSWD was more complicated. The BGSWD was relatively flat when the COD was small, and two major peaks emerged when the COD was increased to 200 μm.

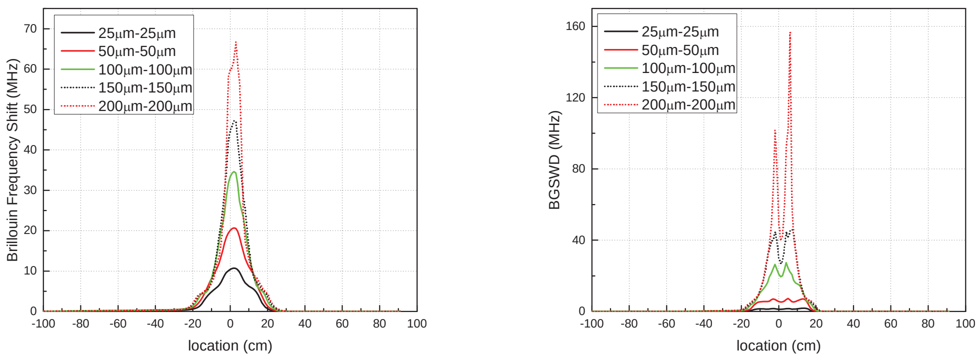

(a) 20cm SR

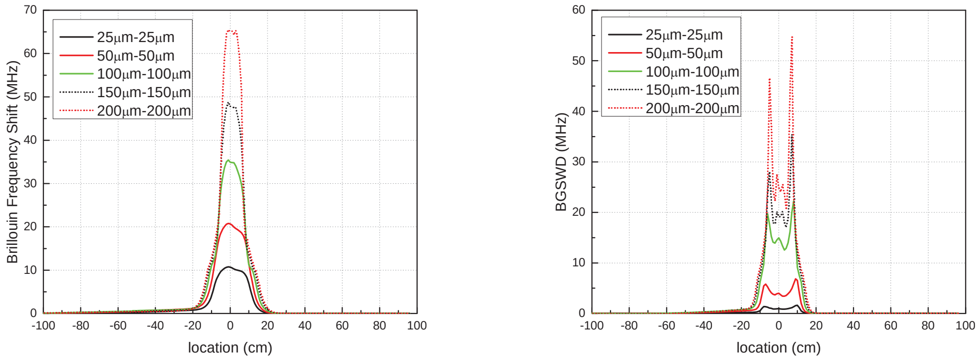

(b) 10cm SR

Figure 55. BFS and BGSWD from numerical simulation for 10cm crack spacing

The amplitudes of BFS and BGSWD from the dual-crack case are shown in Figure 56 (a)-(b), and their ratios to the amplitudes from the single-crack case are shown in Figure 56 (c)-(d). Compared to the single-crack case, the amplitudes of BFS and BGSWD were much larger when 20cm SR was employed, and only slightly larger or similar when 10cm SR was employed.

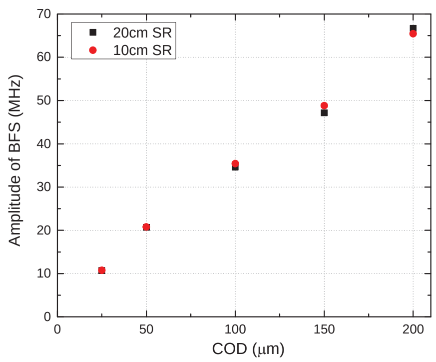

(a) BFS

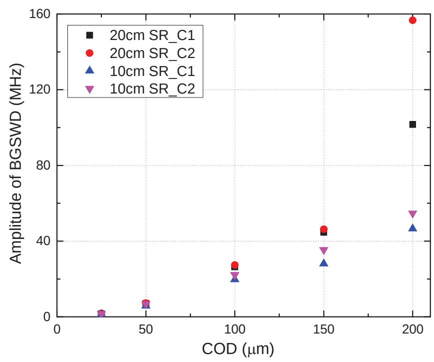

(b) BGSWD

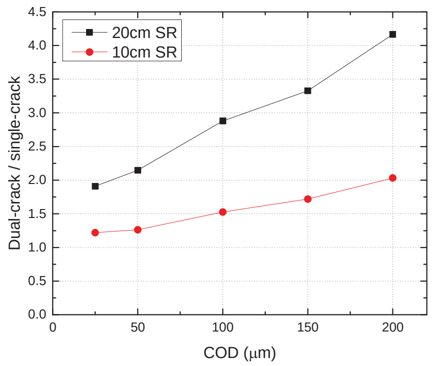

(c) Ratio of BFS

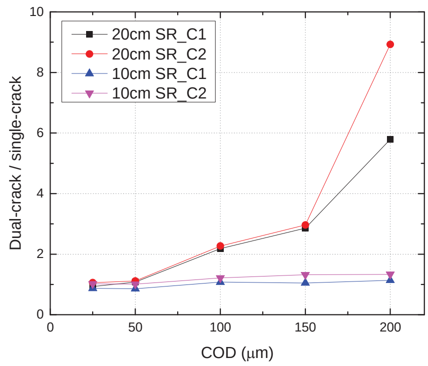

(d) Ratio of BGSWD

Figure 56. Amplitudes from numerical simulation for 10cm crack spacing

The affected lengths of BFS and BGSWD from the dual-crack case are shown in Figure 57 (a)-(b), and their ratios to the affected lengths from the single-crack case are shown in Figure 57 (c)-(d). Compared to the single-crack case, the affected lengths of BFS and BGSWD were generally larger when 20cm SR was employed, and in similar magnitudes when 10cm SR was employed. The affected lengths of BGSWD suddenly decreased when the COD was increased to 200 μm.

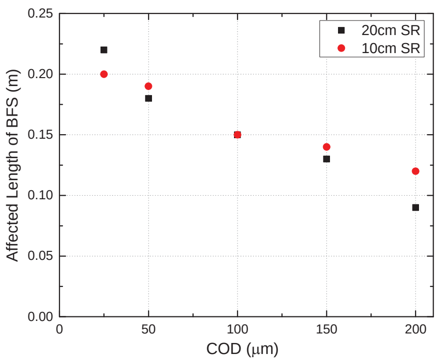

(a) BFS

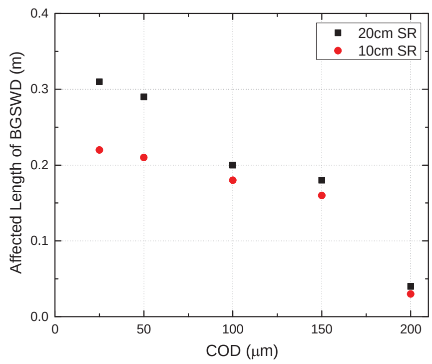

(b) BGSWD

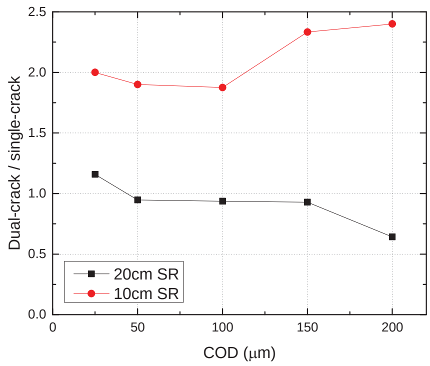

(c) Ratio of BFS

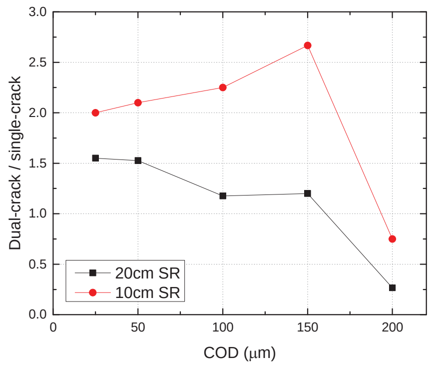

(d) Ratio of BGSWD

Figure 57. Affected lengths from numerical simulation for 10cm crack spacing

4.3.3 Results summary

Based on whether two peaks were clearly recognized from BFS and BGSWD, the results from numerical simulation are summarized in Tables X – XI for the dual-crack cases.

Table X. BFS from numerical simulation

(√ for successful, x for unsuccessful, - for unconsidered)

crack spacing (cm)		50cm	20cm	10cm
Spatial resolution applied (cm)	50cm	√	x	-
	20cm	√	x	x
	10cm	√	√	x

Table XI. BGSWD from numerical simulation

(√ for successful, x for unsuccessful, - for unconsidered)

crack spacing (cm)		50cm	20cm	10cm
Spatial resolution applied (cm)	50cm	√	x	-
	20cm	√	x	√
	10cm	√	√	√

In general, results from numerical simulation indicated that neighboring cracks could be differentiated as distinctive peaks from BFS and BGSWD with SR smaller the crack spacing. In this case, the amplitudes and affected lengths of BFS and BGSWD were similar to the single-crack case. When an inferior SR was employed, differentiating neighboring cracks as separate peaks from BFS and BGSWD could be questionable.

BGSWD would have better performances than BFS since it was successful for 3 out of 5 cases under study. Even though two peaks were recognized from BFS or BGSWD in these cases, the amplitudes and affected lengths were usually different from the single crack case. Following the findings from numerical simulation, dual-crack tests were carried out to study the capability of a commercial PPP-BOTDA device (NBX-6055) in differentiating neighboring cracks.

4.4 Dual-crack tests

4.4.1 Test setup

The setup of the dual-crack test is shown in Figure 58. Three aluminum plates were employed in a line to create two parallel cracks. The two plates on the sides were movable and controlled by two micrometer-stages, while the plate in the center was fixed to the optic table. Two cracks appeared when the two side-plates moved away from the central plate. The spacing between the two cracks was adjustable by changing the length of the central plate. In this study, three different lengths 50cm, 20cm and 10cm were chosen for the central plate. The CODs were monitored by FBG based displacement gauges installed at the crack locations. The distributed sensor traversing the two cracks were tensioned and adhered to the top surfaces of the plates with a thin layer of adhesive. CODs up to 200μm were applied to each crack. The same cases studied in numerical simulation were employed in the tests.

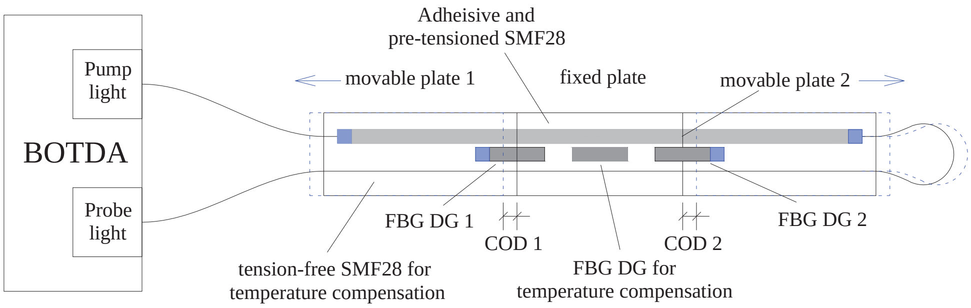

(a) Schema of the test setup

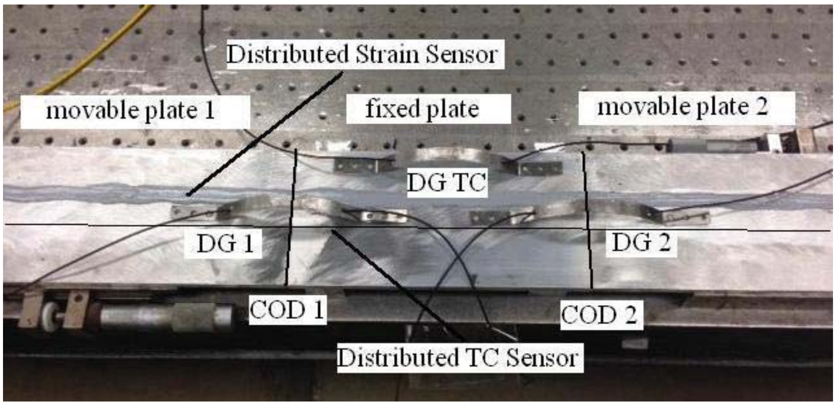

(b) Picture of the test setup

Figure 58. Setup of dual-crack test

4.4.2 Measured results from two-crack-plate tests

The measured results from the dual-crack tests are shown in Figures 59-68.

4.4.2.1 50cm crack spacing

The BFS and BGSWD measured from the dual-crack-plate tests with 50cm spacing are shown in Figure 59. The two cracks (located at 4.3m and 4.8m) were vaguely recognized as two peaks from the BFS and BGSWD when 50cm SR was employed. The locations of the peaks slightly deviated from the exact locations of the cracks. When 20cm SR or 10cm SR was employed, the two cracks were recognized as two distinct peaks from the measured BFS and BGSWD. However, BGSWD was not sensitive for CODs smaller than 100 μm.

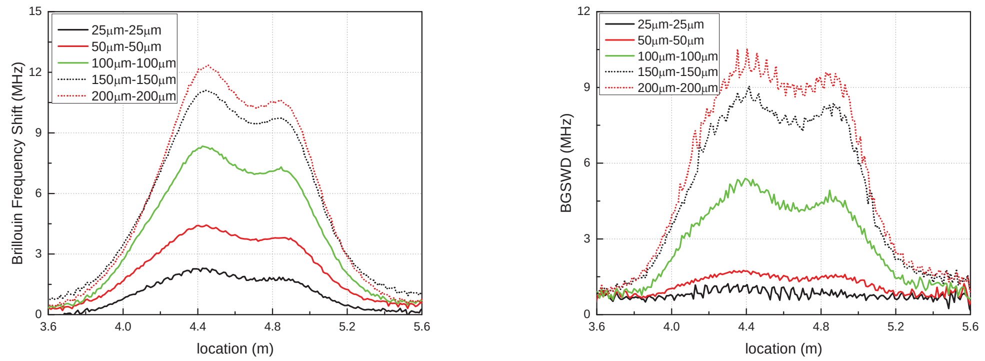

(a) 50cm SR

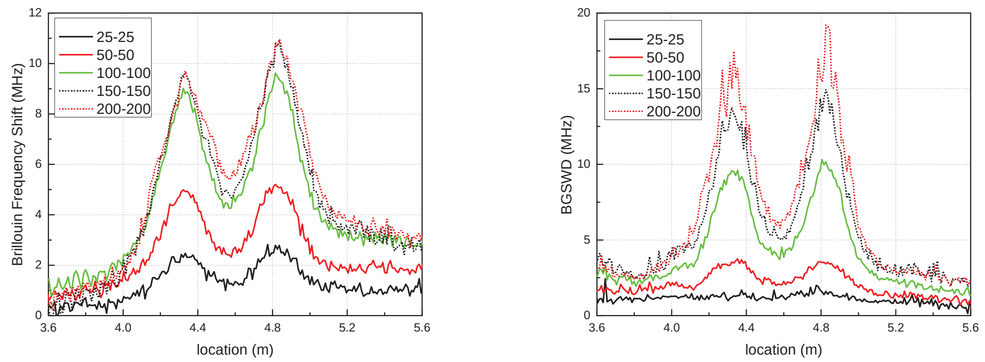

(b) 20cm SR

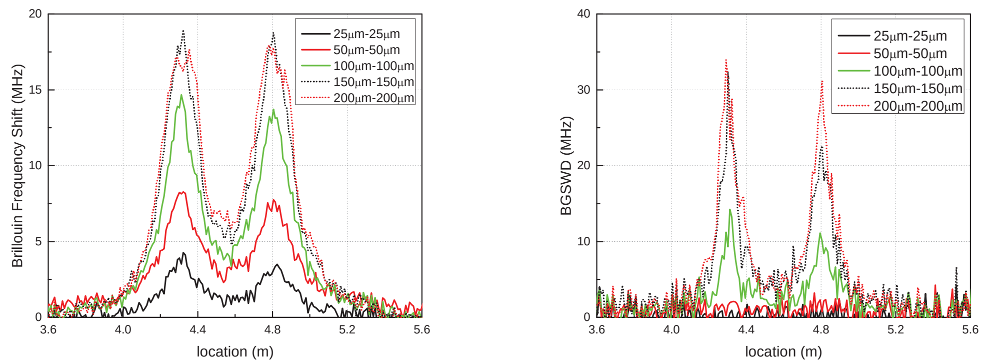

(c) 10cm SR

Figure 59. BFS and BGSWD measured from the test with 50cm crack spacing

The amplitudes of BFS and BGSWD from the dual-crack test are shown in Figure 60 (a)-(b), and their ratios to the amplitudes from the single-crack test are shown in Figure 60 (c)-(d). In general, the amplitudes increased with the COD and tended to stop growing when the COD was increased to $200\ \mu m$. The amplitudes of BFS and BGSWD measured from the dual-crack test were similar to the single-crack case.

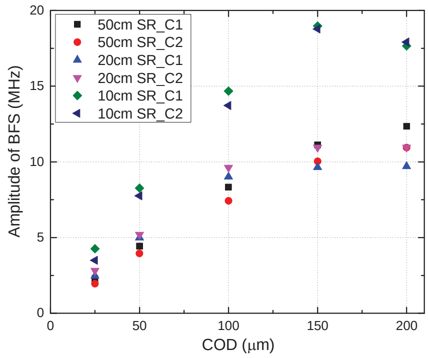

(a) BFS

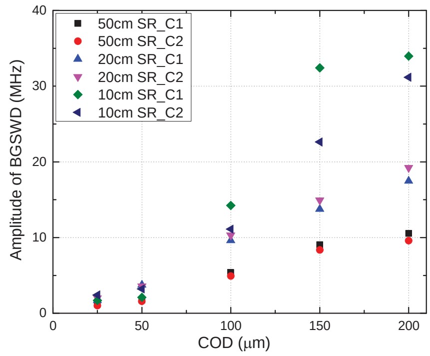

(b) BGSWD

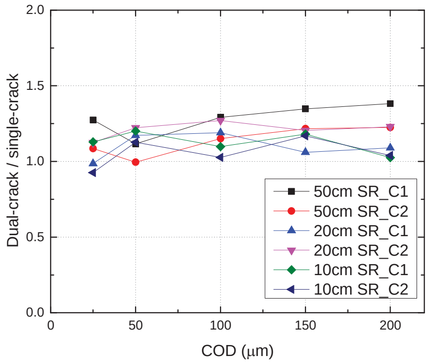

(c) Ratio of BFS

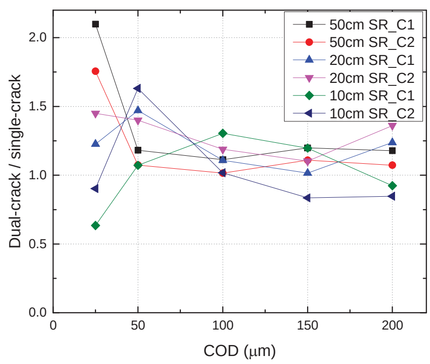

(d) Ratio of BGSWD

Figure 60. Amplitudes measured from the test with 50cm crack spacing

The affected lengths of BFS and BGSWD from the dual-crack test are shown in Figure 61 (a)-(b), and their ratios to the affected lengths from the single-crack test are shown in Figure 61 (c)-(d). Similar to the single-crack test, the affected lengths did change much under different CODs for each SR, and decreased when the SR was improved. When 50cm SR was employed, the BFS and BGSWD between the two peaks were larger than the half maximums. As a result, only one affected length was provided for the dual-crack case, and the affected lengths were much larger than the single-crack test. When 20cm or 10cm SR was employed, the affected lengths of BFS and BGSWD measured from the dual-crack test was similar to the single-crack test.

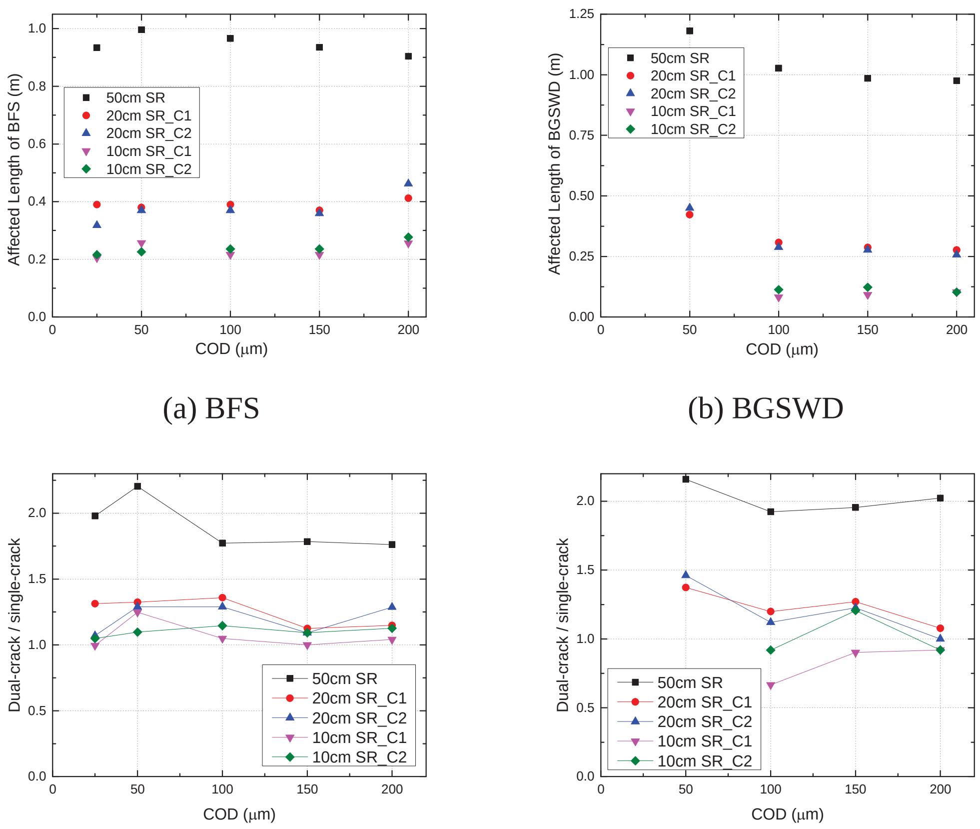

(a) BFS (b) BGSWD

(c) Ratio of BFS (d) Ratio of BGSWD

Figure 61. Affected lengths measured from the test with 50cm crack spacing

4.4.2.2 <u>20cm crack spacing</u>

The BFS and BGSWD measured from the dual-crack-plate tests with 20cm spacing are shown in Figure 62. Only one peak appeared between the two cracks (located at 4.6m and 4.8m) when 50cm SR was employed. When 20cm was employed, one peak was shown from the BFS, and a relatively flat top was shown from the BGSWD. When 10cm SR was employed, the cracks were vaguely recognized as two peaks from the BFS, and recognized as two distinct peaks from BGSWD when COD was larger than $100\ \mu m$.

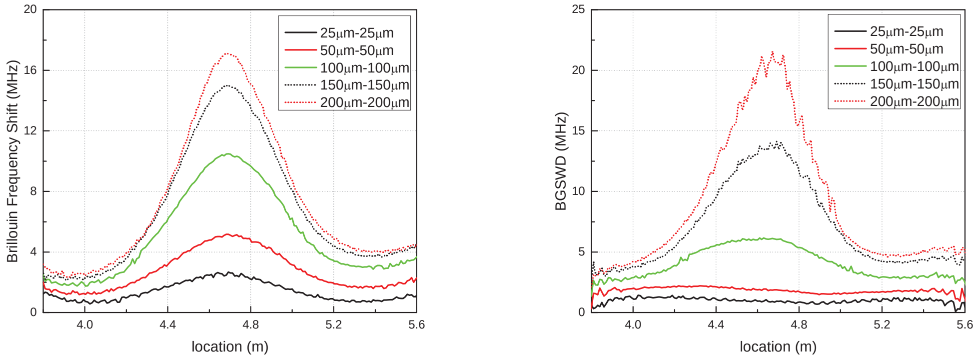

(a) 50cm SR

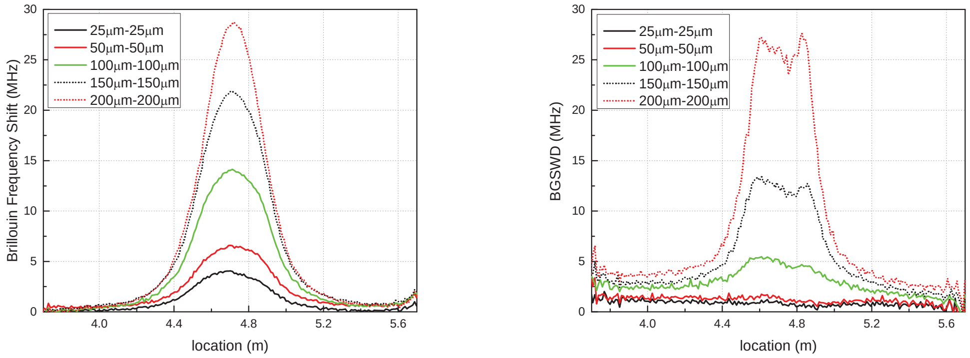

(b) 20cm SR

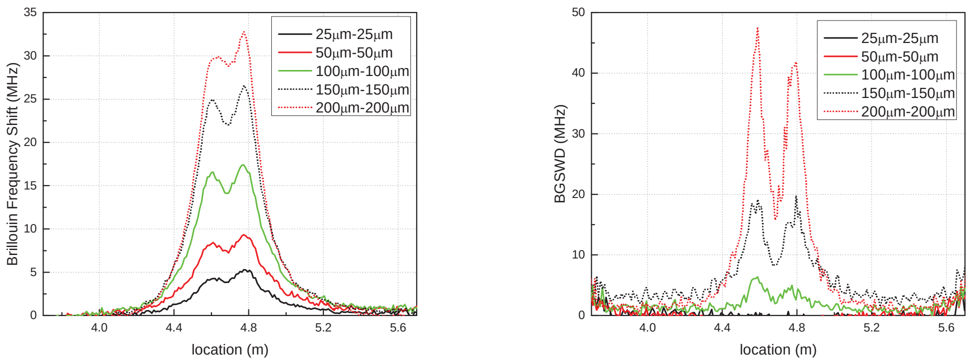

(c) 10cm SR

Figure 62. BFS and BGSWD measured from the test with 20cm crack spacing

The amplitudes of BFS and BGSWD from the dual-crack test are shown in Figure 63 (a)-(b), and their ratios to the amplitudes from the single-crack test are shown in Figure 63 (c)-(d).The amplitudes were positively related to the COD for each SR. Compared to the single crack case, growth of different degrees were found in the amplitudes of BFS. The amplitudes of BGSWD measured from the dual-crack case were larger than the amplitudes from the single-crack test when 50cm SR was employed.

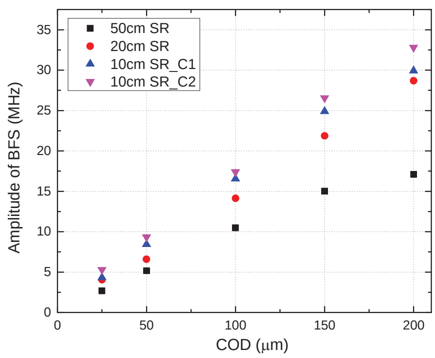

(a) BFS

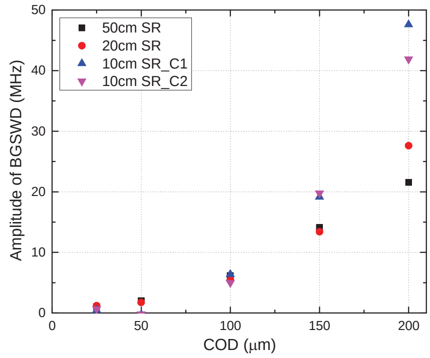

(b) BGSWD

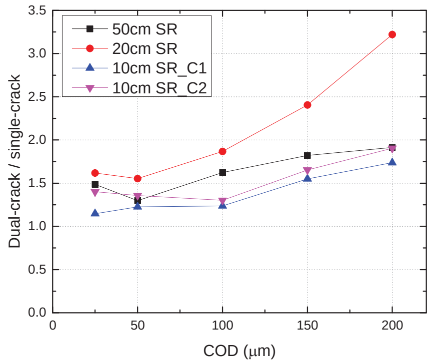

(c) Ratio of BFS

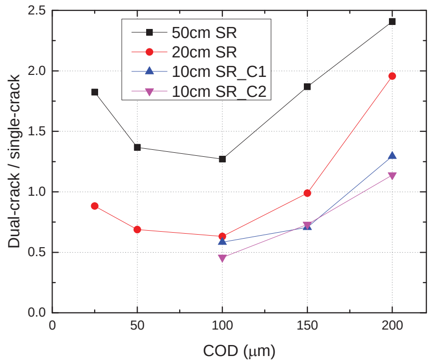

(d) Ratio of BGSWD

Figure 63. Amplitudes measured from the test with 20cm crack spacing

The affected lengths of the BFS and BGSWD from the dual-crack test are shown in Figure 64 (a)-(b), and their ratios to the affected lengths from the single-crack test are shown in figure 64 (c)-(d). The affected lengths of the BFS were for the two cracks as a unity and larger than the affected lengths from the single-crack test. Similarly, the affected lengths of the BGSWD were also larger than the affected lengths from the single-crack test when 50cm or 20cm SR was employed. When 10cm SR was employed, the affected lengths of BGSWD from the dual-crack test were similar to the single-crack test as two distinct peaks were shown.

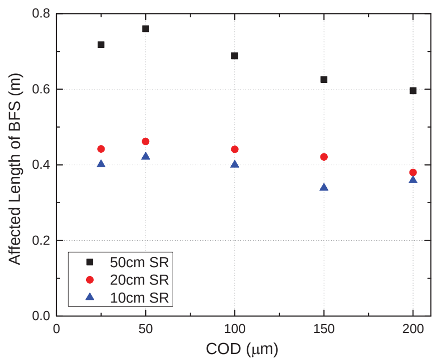

(a) BFS

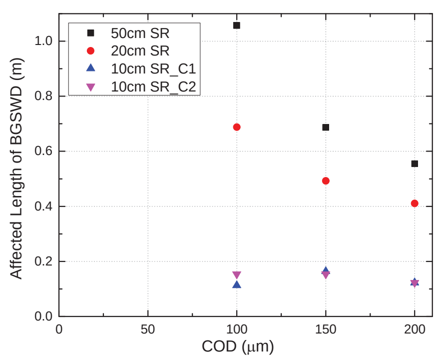

(b) BGSWD

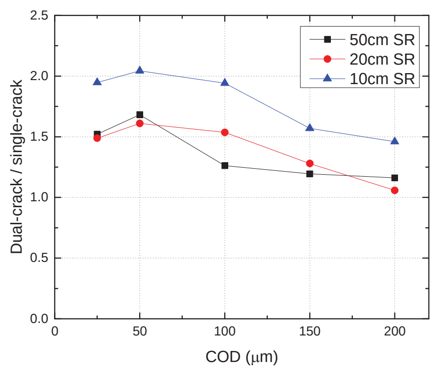

(c) Ratio of BFS

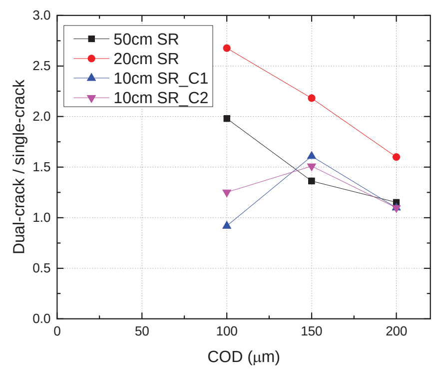

(d) Ratio of BGSWD

Figure 64. Affected lengths measured from the test with 20cm crack spacing

4.4.2.3 <u>10cm crack spacing</u>

The BFS and BGSWD measured from the dual-crack case with 10cm spacing are shown in Figure 65. 20cm and 10cm SRs were employed considering the crack spacing was only 10cm. One major peak was shown from the BFS and BGSWD when 20cm SR was employed. The peak was between the two cracks (located at 5.15m and 5.25m). When 10cm SR was employed, one major peak was first found from the BFS, which was then split into two minor peaks under the COD of 200 μm. Two distinct peaks were shown from BGSWD when CODs are larger than 100 μm.

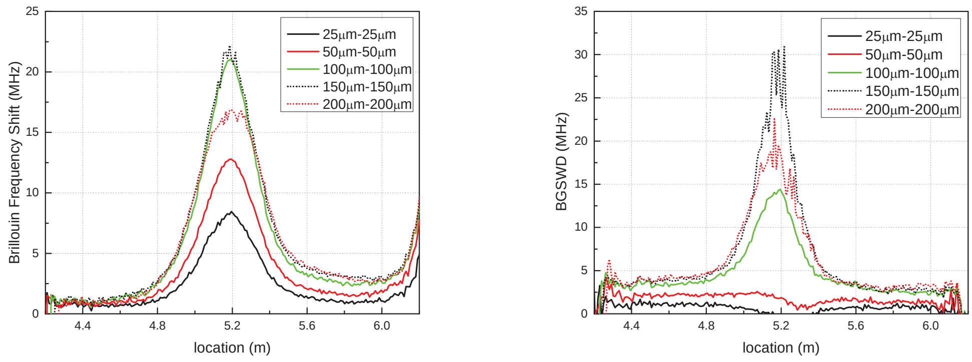

(a) 20cm SR

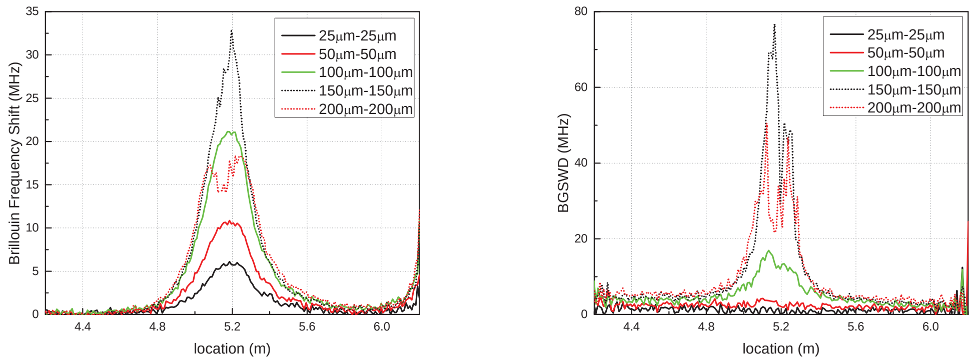

(b) 10cm SR

Figure 65. BFS and BGSWD measured from the test with 10cm crack spacing

The amplitudes of BFS and BGSWD are shown in Figure 66 (a)-(b), and their ratios to the amplitudes from the single-crack test are shown in Figure 66 (c)-(d). With one major peak shown from the BFS, the amplitudes measured from the dual-crack test were much larger than the single-crack test. The amplitudes decreased when the COD was increased from 150 μm to 200 μm. Similarly, the amplitudes of BGSWD from the dual-crack test were usually larger than the single-crack test, and the amplitudes decreased when the COD was larger than 150 μm.

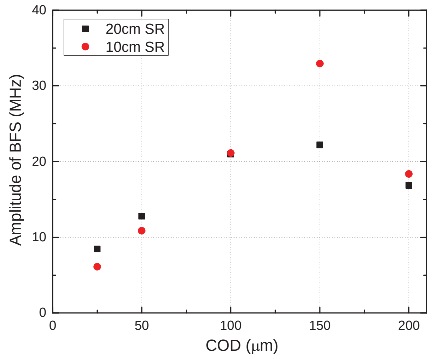

(a) BFS

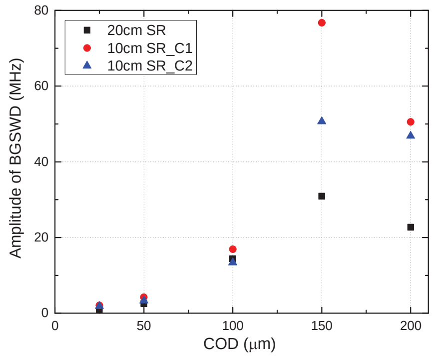

(b) BGSWD

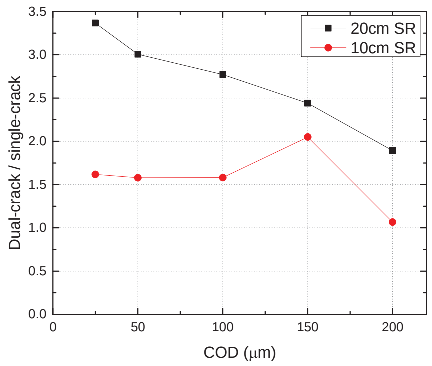

(c) Ratio of BFS

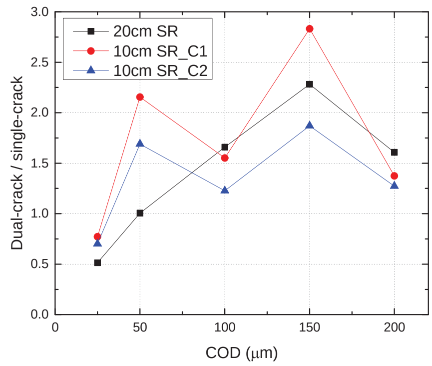

(d) Ratio of BGSWD

Figure 66. Amplitudes measured from the test with 10cm crack spacing

The affected lengths of BFS and BGSWD are shown in Figure 67 (a)-(b), and their ratios to the affected lengths from the single-crack test are shown in Figure 67 (c)-(d). With one major peak shown from the BFS, the affected lengths from the dual-crack test were a little larger than the single-crack test. The affected lengths of BGSWD from the dual-crack test were similar to the single crack test.

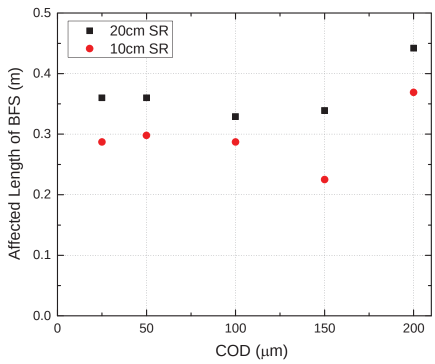

(a) BFS

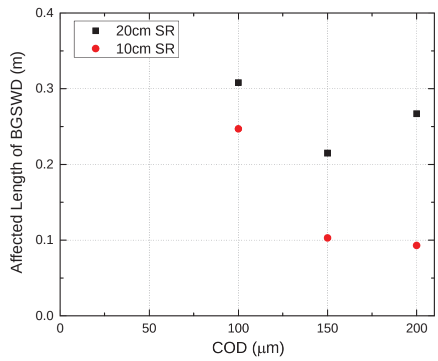

(b) BGSWD

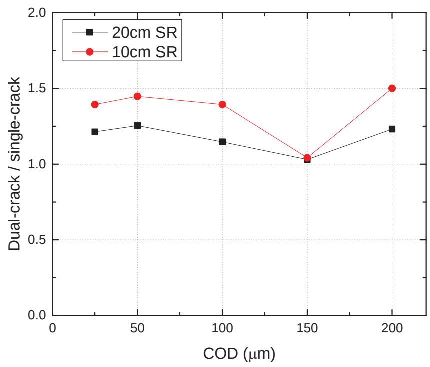

(c) Ratio of BFS

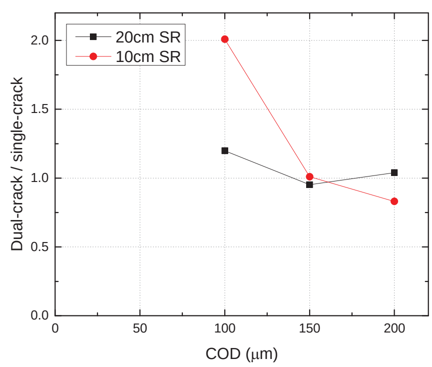

(d) Ratio of BGSWD

Figure 67. Affected lengths measured from the test with 10cm crack spacing

4.4.3 <u>Results summary</u>

Based on whether two distinct peaks were recognized from BFS and BGSWD measured by PPP-BOTDA, the results of the dual-crack-plate tests are summarized in Tables XII – XIII. In general, measured results conformed to the findings from numerical simulation. When the SR employed is smaller than the crack spacing, the neighboring cracks were differentiated as two distinctive peaks from BFS and BGSWD. When a lower SR was employed, differentiating neighboring cracks as separate peaks from BFS and BGSWD could be questionable, and BGSWD had better performances than BFS since two peaks were successfully recognized from BGSWD for the 10cm crack spacing case when 10cm SR was employed. For the case of 10cm spacing, the amplitudes of BFS and BGSWD were found decreased when the COD was increased from $150\ \mu m$ to $200\ \mu m$. Similar to the single-crack case, BGSWD measured from the dual-crack cases was not sensitive to small CODs.

Table XII. BFS measured from tests
(√ for successful, x for unsuccessful, - for unconsidered)

		Distance between two cracks (cm)		
		50cm	20cm	10cm
Spatial resolution applied (cm)	50cm	x	x	-
	20cm	√	x	x
	10cm	√	√	x

Table XIII. BGSWD measured from tests
(√ for successful, x for unsuccessful, - for unconsidered)

		Distance between two cracks (cm)		
		50cm	20cm	10cm
Spatial resolution applied (cm)	50cm	x	x	-
	20cm	√	x	x
	10cm	√	√	√

4.5 Summary

The capability of PPP-BOTDA in differentiating two neighboring surface-cracks was studied through numerical simulation and experimental research in this chapter.

Strain induced by a dual-crack case was analyzed based on superposition for a distributed sensor installed on the structural surface. FEA was performed to validate the correctness of the theoretical strain analysis. With the strain from theoretical analysis as input, numerical simulation was performed to simulate the changes in the BGS, which were characterized by BFS and BGSWD. Different crack spacing (50cm, 20cm and 10cm) and SRs (50cm, 20cm and 10cm SRs) were employed in the study. Results from numerical simulation showed that the neighboring cracks could be differentiated as two peaks from the BFS and BGSWD when the SR employed was smaller than the crack spacing, and the amplitudes and affected lengths of BFS and BGSWD were similar to the single crack case. When the SR was similar to or larger than the crack spacing, it was questionable for PPP-BOTDA to differentiate two neighboring cracks as separate peaks from BFS and BGSWD, and BGSWD had better performance than BFS in this case.

Following the numerical simulation, the capability of a commercial PPP-BOTDA device in differentiating neighboring cracks was evaluated through dual-crack tests. Overall, results from the tests matched with numerical simulation. The neighboring cracks were differentiated as two distinct peaks from BFS and BGSWD when the SR employed was smaller than the crack spacing. The amplitudes and affected lengths of BFS and BGSWD were similar to the single-crack case. When the SR employed was same to or larger than the crack spacing, PPP-BOTDA failed to detect the cracks as two peaks in most cases. BGSWD had better performances than BFS when the crack spacing was small, and two peaks were successfully recognized from BGSWD for the 10cm-spacing case when 10cm SR was employed. However, BGSWD was found not sensitive to small CODs. In addition, the amplitudes of BFS and BGSWD decreased for the 10cm-spacing case when COD was larger than 150 μm, which made monitoring of COD based on amplitudes questionable.

5. CRACK DETECTION AND MORNITORING ON RC BEAMS 4 AND 5

5.1 Introductions

In chapter 3, the attempt to detect and monitor cracks on RC beams 1-3 as peaks from BFS and BGSWD was unsuccessful when 20cm SR was employed. From visual inspections after the load tests, the crack spacing on RC beams 1 – 3 was about 10cm ~ 15cm, which was smaller than the SR employed. In chapter 4, the capability of PPP-BOTDA in differentiating neighboring cracks was studied through a series of dual-crack tests, and it was concluded that PPP-BOTDA distributed sensing could differentiate neighboring cracks as two distinct peaks from BFS and BGSWD when the SR employed was smaller than the crack spacing. In this chapter, crack detection and monitoring were performed on two more RC beams (RC beams 4-5) based on PPP-BOTDA distributed sensing. Considering the crack spacing on the RC beams and the SRs provided by NBX-6055, 10cm SR was employed in the distributed sensing. In addition, pre-existing notches were arranged at certain locations on the tension surfaces of RC beams 4 – 5 to initiate cracks. The designs and results are introduced in the following sections.

5.2 Load test of RC beam 4

5.2.1 Beam design and sensor installation

Similar to RC beams 1-3, the structural design of RC beam 4 is shown in Figure 68. Notches of ¼ inch depth were created on the tension surface of the beam to initiate cracks at certain locations. The notches were located at 0.45m, 0.5m, 0.6m, 0.8m, 0.85m, 1.05m, 1.25m, 1.45m, 1.55m, 1.85m, 2.05m and 2.15m from the left supporting point, and can be seen in Figure 68 (a). The ratio of water/concrete mix for RC beam 4 was 7.5lbs per 80lbs.

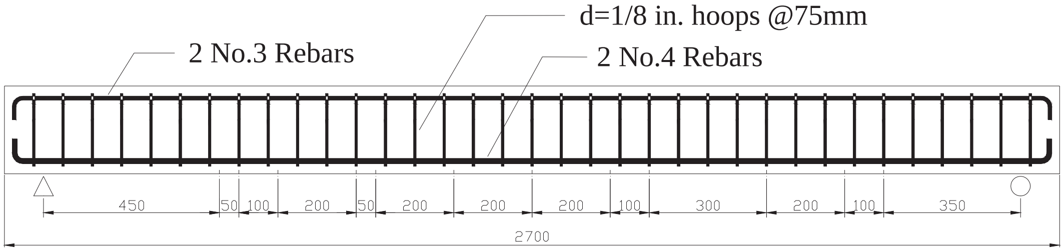

(a) Side view (unit: mm)

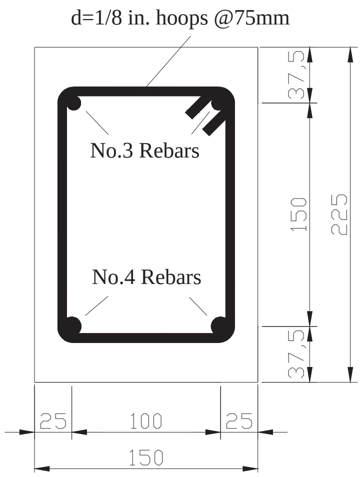

(b) Cross section view (unit: mm)

Figure 68. Structural design of RC beam 4

PPP-BOTDA distributed sensors and FBG sensors were both installed inside and on the surfaces of the beam. The embedded distributed sensors (G1-G3, O1-O3 and R1-R4) and FBG sensors (FR1-FR6) were installed before concrete pouring. The locations of the embedded distributed sensors are shown in Figure 69.

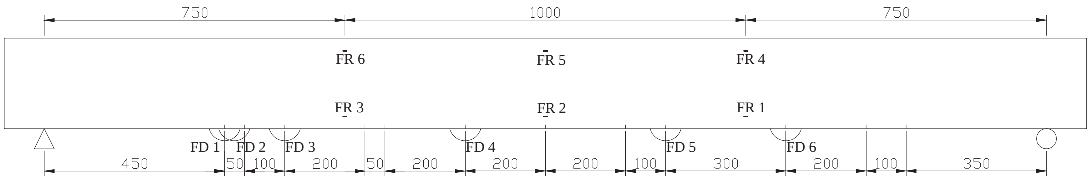

(a) Side view (unit: mm)

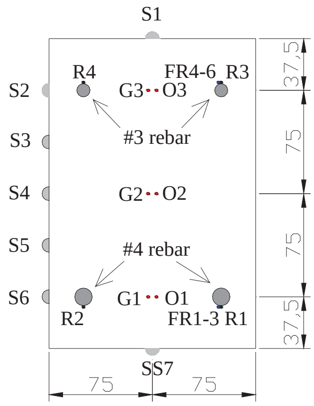

(b) cross section view

Figure 69. Locations of sensors installed on RC beam 4

The procedure of sensor installation was similar to RC beams 1-3, and can be referred to chapter 3. The embedded sensors G1-G3 had structures similar to O1-O3. The only difference was the wall thickness of the peek tube. The schema of G1-G3 comparing with O1-O3 is shown in Figure 70.

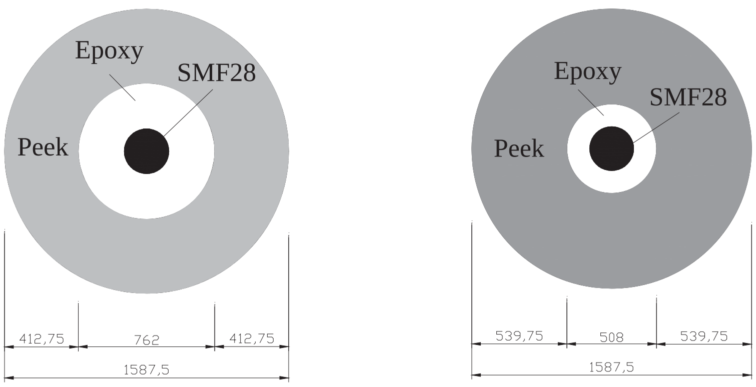

(a) G1-G3 (b) O1-O3

Figure 70. Cross section view of G1-G3 comparing with O1-O3 (unit: **μm**)

The RC beam 4 was cured in moisture for the first 7 days, and then cured in the air. The forms were taken off after 21 days from concrete pouring, and distributed sensors S1-S7 were installed on the surfaces of the beam. The locations of S1-S7 are shown according to Figure 69(b). After RC beam 4 was placed for the loading tests, FBG displacement sensors FD1 – FD6 were installed on the tension surface of the beam to monitor the widening of certain notches during the load tests. The locations of FBG displacement sensors are shown in Figure 69(a).

5.2.2 Load test

The test setup was same to RC beams 1-3 and can be referred to chapter 3. Before the load test, concrete cylinder test was performed and the results are listed in Table XIV.

Table XIV. Results from concrete cylinder test

Specimen No.	1	2	3	Average
Ultimate load (lbs)	233125	240835	239390	237780
Stress (psi)	8245	8515	8465	8408

The average compressive strength from the concrete cylinder test was $8408\,psi$ (57.97 MPa). According to ACI 318-08, the Young's modulus and rapture strength of the concrete were estimated at $5266.6\,ksi$ $(36.31\,\mathrm{GPa})$ and $687.7\,psi$ $(4.74\,\mathrm{MPa})$, respectively. The cracking load was estimated about 2800 lbs, and the ultimate load was estimated about 12200 lbs. The calculations can be referred to Appendix B.

The load test was performed in three cycles. In Cycle 1, the beam was loaded from 0 to 2000 lbs and believed to keep intact or experience minor damages. In Cycle 2, the beam was loaded up to 4000lbs, and major cracking was expected when the load was beyond 2000 lbs. In Cycle 3, the beam was loaded from 0 to 8000lbs, and severe cracking was expected. The load – deflection curve is shown in Figure 71. The sudden change in the slope between 2000 lbs and 3000 lbs indicated initial cracking. The beam failed under the load of 14500 lbs.

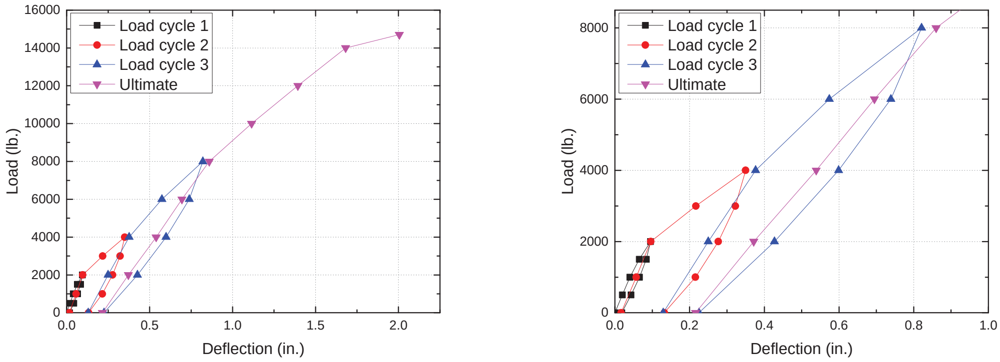

(a) Overall (b) details of load cycles 1-3

Figure 71. Figure 5.4 Load-deflection curve of RC beam 4

5.2.3 Test results

5.2.3.1 Results from S7

Distributed sensor S7 was installed on the tension surface of RC beam 4 and experienced larger tensile strains than the other distributed sensors. With the intact state of the beam as reference, BFS and BGSWD under different loads are shown in Figures 72-75.

(1) Load cycle 1

The measured BFS and BGSWD from load cycle 1 are show in Figure 72. Three peaks were recognized from the BFS under the load of 2000 lbs, corresponding to the notches at 0.6m, 1.05m and 1.55m. Slight nonlinearity was noticed between the loads of 1500 lbs and 2000 lbs. No distinct peak was found from the BGSWD, and the results were noisy.

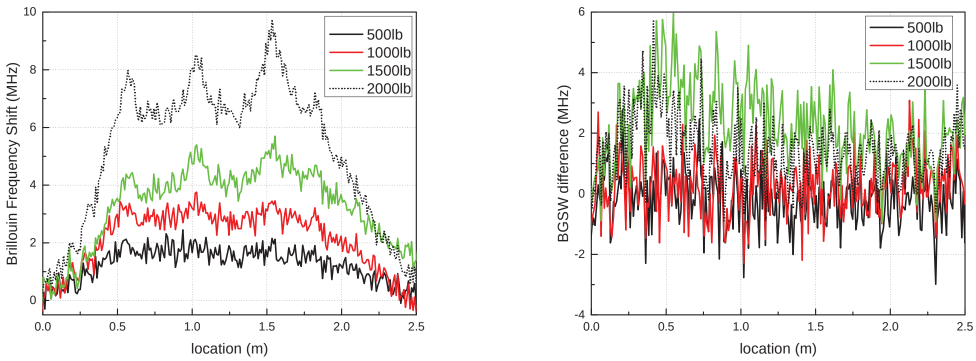

(a) BFS (b) BGSWD

Figure 72. Figure 5.5 BFS and BGSWD from load cycle 1

The displacements measured by sensors FD1 – FD6 are shown in Table XV. Considering the locations of the sensors, no major difference was shown between the sensors in respect of crack developing.

Table XV. Displacements measured by FD1-FD6 in load cycle 1 (unit: **μm**)

Loads (lbs)	FD 1	FD 2	FD 3	FD 4	FD 5	FD 6
500	-1.02	-0.12	4.11	5.27	6.53	3.83
1000	3.45	5.92	13.07	14.57	19.12	11.80
1500	5.28	9.98	19.57	21.49	27.87	19.38
2000	5.56	13.88	26.94	31.13	40.32	26.73

(2) Load cycle 2

The measured BFS and BGSWD from load cycle 2 are show in Figure 73. Small residue was found from the BFS before any load was applied, indicating small damages accumulated in the beam already. Similar to load cycle 1, peaks were found at 0.6m, 1.05m and 1.55m from BFS under the load of 2000 lbs. More peaks appeared at 0.8m, 1.25m and 1.7m under the loads of 3000 lbs and 4000lbs, and the peak at 1.55m shifted to 1.5m. Results from BGSWD were with a higher noise level. No distinct peak was recognized from BGSWD until the load of 3000 lbs, and the peaks were found at 0.8m, 1.05m 1.45m and 1.85m from BGSWD. Under the load of 4000 lbs, more peaks were found at 0.4m, 0.6m, and 1.25m.

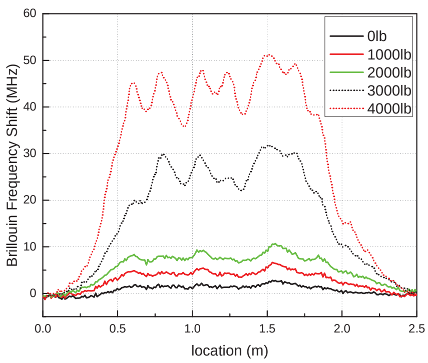

(a) BFS

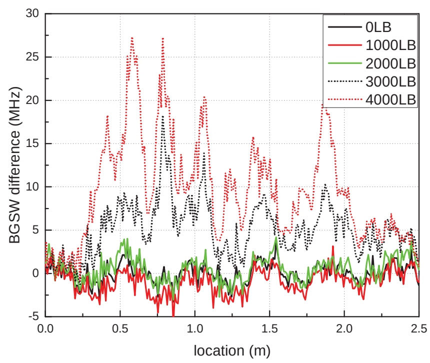

(b) BGSWD

Figure 73. BFS and BGSWD from load cycle 2

The results from the displacement sensors matched with the results from S7. The displacements measured by FD1 – FD6 are listed in Table XVI. Under the load of 3000 lbs, the displacement measured by FD 4 was obviously larger than the supposed value, indicating a crack developing at 1.05m. Under the load of 4000 lbs, the displacements measured by FD3, FD4 and FD6 were larger than the average value, indicating cracks developing at 0.6m and 1.05m and 1.85m.

Table XVI. Displacements measured by FD1-FD6 in load cycle2 (**unit**: **μm**)

Loads (lbs)	FD 1	FD 2	FD 3	FD 4	FD 5	FD 6
0	-6.16	-27.15	-26.15	-27.45	-9.59	-10.28
1000	-5.01	-21.96	-14.18	-13.46	7.68	-0.49
2000	2.27	-10.43	2.02	2.90	30.04	15.57
3000	15.77	7.49	31.93	97.46	54.60	40.75
4000	59.01	49.26	171.53	169.01	98.83	100.54

(3) Load cycle 3

The measured BFS and BGSWD from load cycle 3 are shown in Figure 74. As a result of the cracking damages from load cycle 2, notable residue was found from BFS before any load was applied to the beam. Peaks were recognized from BFS at 0.6m, 0.8m, 1.05m, 1.25m, 1.5m, 1.7m and 1.85m under the load of 4000 lbs, which was consistent with the results from load cycle 2. One new peak was found at 2.05m when the load was increased to 6000 lbs, and no more peaks were found under the load of 8000 lbs. From BGSWD, distinct peaks were identified at 0.4m, 0.6m, 0.8m, 1.05m, 1.25m, 1.45m and 1.85m under 4000 lbs with a threshold of 20 MHz. Two more peaks appeared at 1.7m and 2.2m when the load was increased to 6000 lbs. Since no cracks were located at 0.4m or 2.2m by visual inspections after the load test, it was believed the peaks at these two locations were caused by large strain slopes in the sensing fiber.

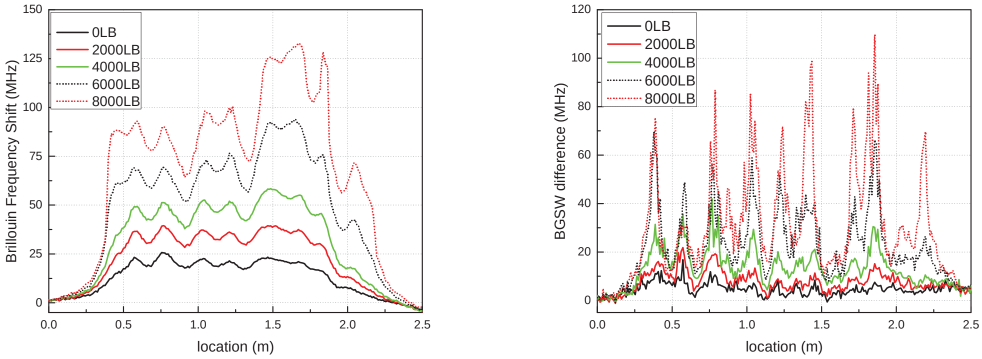

(a) BFS (b) BGSWD

Figure 74. BFS and BGSWD from load cycle 3

The displacements measured by FD1 – FD6 from load cycle 3 are listed in Table XVII. Under the loads of 6000 lbs and 8000 lbs, the measured displacement from FD5 was smaller than the other displacement sensors, indicating the crack at 1.55m didn't open as much as the other cracks. This finding matched with the results from BFS and BGSWD.

Table XVII. Displacements measured by FD1-FD6 in load cycle 3 (**unit**: **μm**)

Loads (lbs)	FD 1	FD 2	FD 3	FD 4	FD 5	FD 6
0	50.76	21.15	70.31	74.42	18.13	28.19
2000	70.16	47.10	135.72	139.64	67.12	70.60
4000	93.82	77.04	203.15	209.85	120.53	117.52
6000	182.93	178.51	298.24	319.09	159.44	207.58
8000	270.40	273.27	413.96	466.78	210.52	338.31

(4) Results summary

The cracks detected by distributed sensor S7 from each load cycle are summarized in Table XVIII. The BGSWD was not sensitive to small cracks and usually had a higher noise level than BFS, which made it difficult to detect cracks at the early stage of cracking. However, BGSWD was better than BFS in differentiating neighboring cracks very close to each other, such as the cracks at 1.45m and 1.55m on the beam. The BGSWD did not work well when the strain slope in the sensing fiber was very large, which was the case for sensor segments close to the supporting points. Positive relationship was found between CODs and amplitudes of the peaks recognized from BFS and BGSWD.

Table XVIII. Results summary for S7 in crack detection

crack locations (m)		0.45	0.6	0.8	1.05	1.25	1.45	1.55	1.7	1.85	2.05
load cycle 1	BFS		√		√			√			
	BGSWD										
load cycle 2	BFS		√	√	√	√			√		
	BGSWD		√	√	√	√	√			√	
load cycle 3	BFS		√	√	√	√	√		√	√	√
	BGSWD		√	√	√	√	√		√	√	

5.2.3.2 <u>Results from O1 and G1</u>

The mechanism of strain-transfer between embedded distributed sensors and surrounding materials was still not clear. In this study, the strain functions developed for the surface-installed distributed sensor was assumed also taken by the embedded distributed sensor. Even though the shear-lag factor was different, similar changes in

BGS should take place when the embedded distributed sensor was subjected to the crack-induced strain. BFS and BGSWD from the embedded distributed sensors O1 and G1 are shown in Figures 75-80 regarding the state of the undamaged beam as the reference.

(1) Load cycle 1

The results measured by O1 and G1 are shown in Figures 75 and 76 respectively. In Figure 75, three peaks at 0.6m, 1.05m and 1.55m were recognized from BFS under the load of 2000 lbs. No distinct peaks were shown from BGSWD. In Figure 76, similar results were obtained from BFS and BGSWD measured by G1.

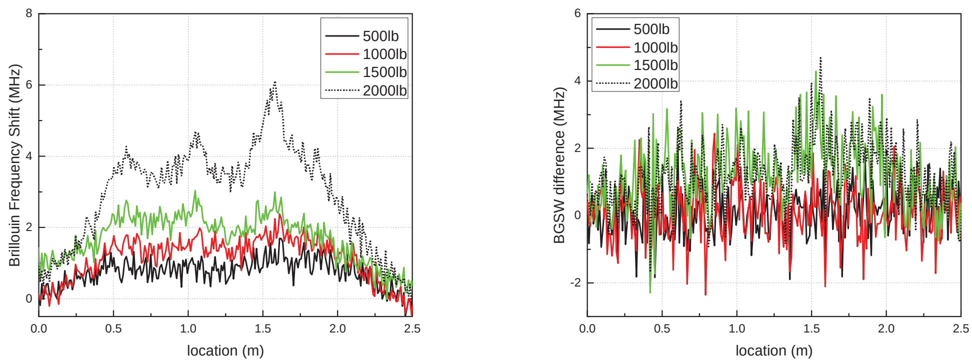

(a) BFS (b) BGSWD

Figure 75. BFS and BGSWD from O1 in load cycle 1

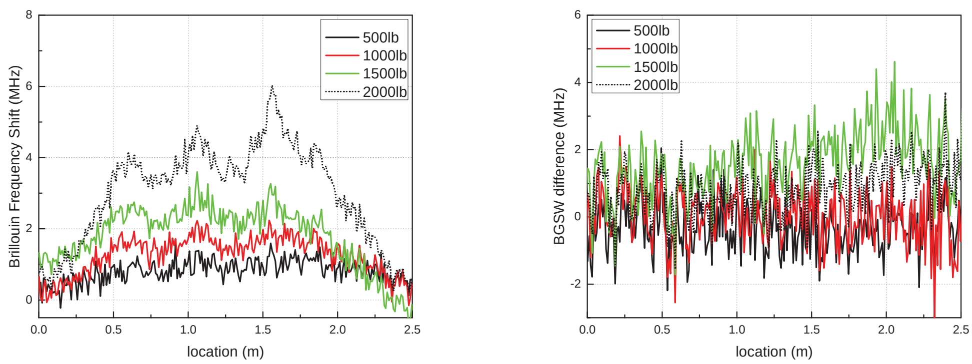

(a) BFS (b) BGSWD

Figure 76. BFS and BGSWD from G1 in load cycle 1

(2) Load cycle 2

The BFS and BGSWD measured by O1 are shown in Figure 77. Peaks were recognized at 0.8m, 1.05m, 1.25m, 1.45m, 1.55m and 1.7m from BFS under the load of 3000 lbs. One more peak was found at 0.6m from BFS under the load of 4000 lbs. Since the noise level of BGSWD was high, only two peaks were recognized at 0.8m and 1.05m under the load of 3000 lbs, and more peaks were recognized at 0.6m and 1.85m under the load of 4000 lbs.

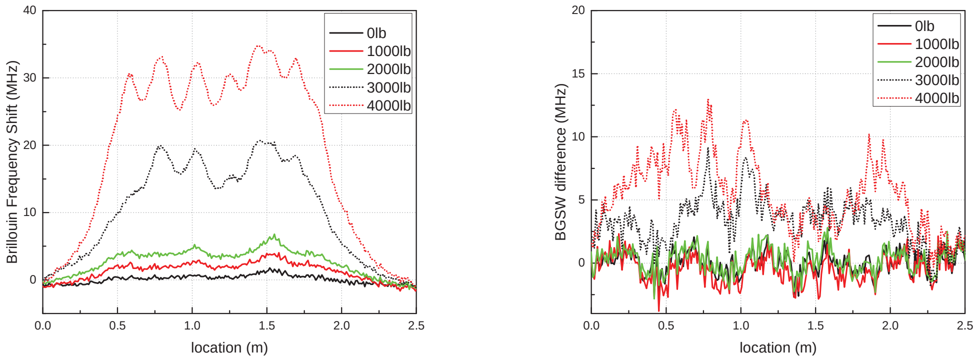

(a) BFS (b) BGSWD

Figure 77. BFS and BGSWD from O1 in load cycle 2

The BFS and BGSWD measured by G1 are shown in Figure 78. Similar to O1, distinct peaks were found at 0.6m, 0.8m, 1.05m, 1.25m, 1.45m, 1.55m and 1.7m from BFS under the load of 4000 lbs. One major peak at 0.8m and a few minor peaks at 0.45m, 0.6m, 1.05m and 1.85m were recognized from BGSWD under the load of 4000 lbs.

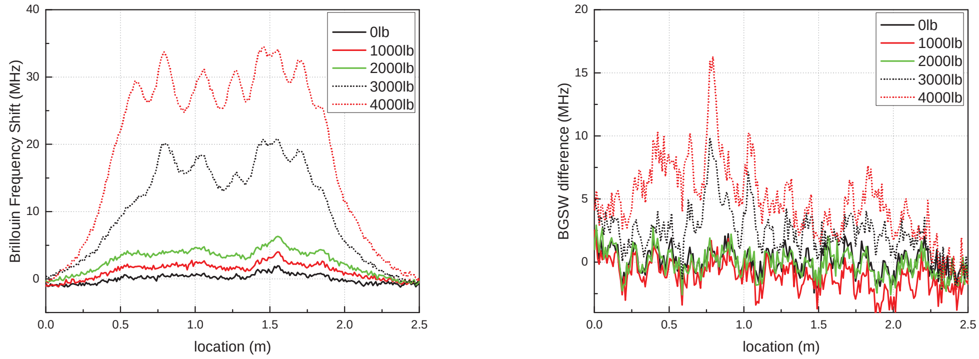

(a) BFS (b) BGSWD

Figure 78. BFS and BGSWD from G1 in load cycle 2

(3) Load cycle 3

The BFS and BGSWD measured by O1 are shown in Figure 79. Peaks were found at 0.6m, 0.8m, 1.05m, 1.25m, 1.45m, 1.55m, 1.7m, 1.85m and 2.05m from BFS under the loads of 6000 lbs and 8000 lbs. Major peaks were found at 0.4m, 0.6m, 0.8m, 1.05m, 1.85m, 2.05m and 2.15m from BGSWD under the loads 6000 lbs of 8000 lbs. However, the peaks at 0.4m and 2.15m did not correspond to any cracks on the beam.

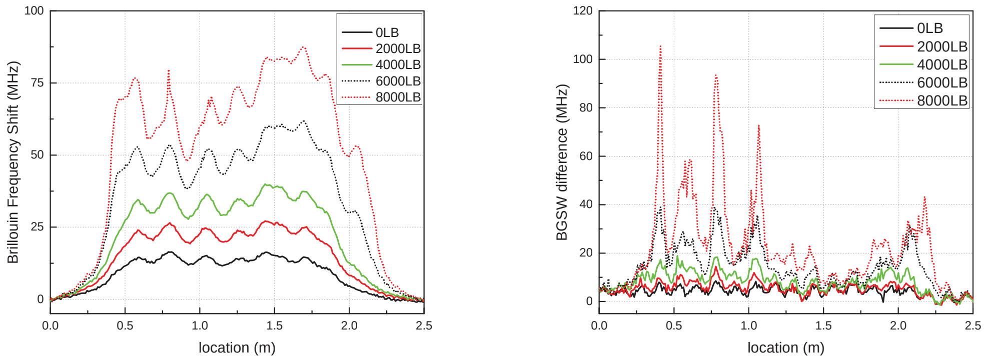

(a) BFS (b) BGSWD

Figure 79. BFS and BGSWD from O1 in load cycle 3

The BFS and BGSWD measured by G1 are shown in Figure 80. Similar to O1, distinct peaks were recognized at 0.6m, 0.8m, 1.05m, 1.25m, 1.45m, 1.55m, 1.7m, 1.85m and 2.05m from BFS under the loads of 6000 lbs and 8000 lbs. Compared to O1, more major peaks were shown from BGSWD measured by G1, and they were located at 0.4m, 0.6m, 0.8m, 1.05m, 1.25m, 1.45m, 1.85m and 2.15m.

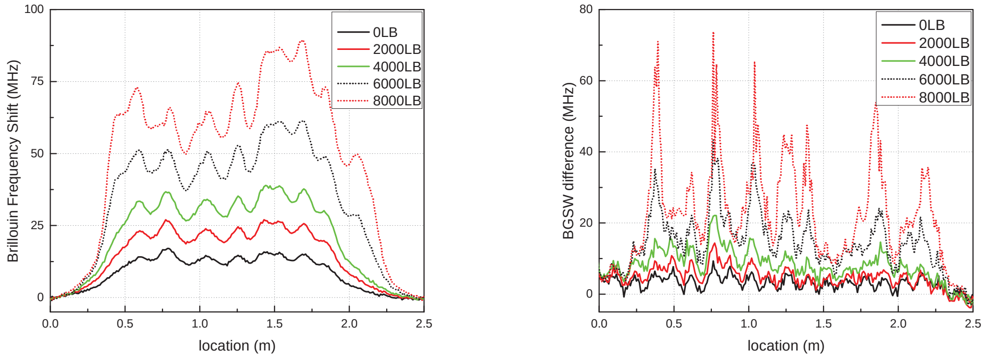

(a) BFS (b) BGSWD

Figure 80. BFS and BGSWD from G1 in load cycle 3

(4) Results summary

The cracks detected by distributed sensors O1 and G1 from each load cycle are summarized in Tables XIX and XX. Overall, peaks from measured BFS and BGSWD by distributed sensors O1 and G1 matched with cracks from visual inspections. Compared to sensor S7, O1 and G1 had better performances in differentiating the neighboring cracks at 1.45m and 1.55m from BFS, which may be caused by larger crack spacing inside the beam. Positive relationship was found between CODs and amplitudes of the peaks recognized from BFS and BGSWD.

Table XIX. Results summary for O1 in crack detection

crack locations (m)		0.45	0.6	0.8	1.05	1.25	1.45	1.55	1.7	1.85	2.05
load cycle 1	BFS		√		√			√			
	BGSWD										
load cycle 2	BFS		√	√	√	√	√	√	√		
	BGSWD		√	√	√					√	
load cycle 3	BFS		√	√	√	√	√	√	√	√	√
	BGSWD		√	√	√					√	√

Table XX. Results summary for G1 in crack detection

crack locations (m)		0.45	0.6	0.8	1.05	1.25	1.45	1.55	1.7	1.85	2.05
load cycle 1	BFS		√		√			√			
	BGSWD										
load cycle 2	BFS		√	√	√	√	√	√	√		
	BGSWD	√	√	√	√					√	
load cycle 3	BFS		√	√	√	√	√	√	√	√	√
	BGSWD		√	√	√	√	√			√	

5.3 Load test of RC beam 5

5.3.1 Beam design and sensor installation

RC beam 5 shared the same design with RC beam 4 in the dimension and reinforcement layout, and relevant information can be referred to Section 5.2.1. The water/concrete mix ratio of RC beam 5 was 8 lbs per 80 lbs. Six notches located at 0.5m, 0.85m, 1.05m, 1.25m, 1.55m and 2.05m from the left supporting point were created on the tension surface of the beam to initiate cracks, and the locations are shown in Figure 81.

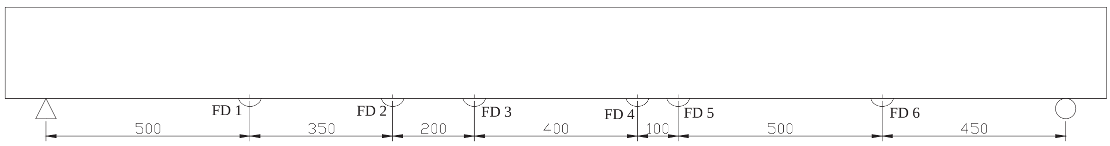

Figure 81. Locations of notches and displacement sensors on RC beam 5 (unit: mm)

Same procedures of sensor installation and beam fabrication for RC beam 4 were followed by RC beam 5. The layout of the embedded sensors and surface-installed distributed sensors for RC beam 5 was same to RC beam 4, and relevant information can be referred to Section 5.2.2. Before the load test, FBG displacement sensors FD1 – FD6 were installed on the tension surface of the beam to monitor widening of the notches, and their locations are shown in Figure 81.

5.3.2 Load test

The concrete cylinder test was employed to estimate strength of the concrete, and the results are shown in Table XXI.

Table XXI. Results from concrete cylinder tests of RC beam 5

Specimen No.	1	2	3	Average
Ultimate load (lbs)	210670	217120	188720	205500
Stress (psi)	7450	7680	6675	7268

Based on the average compressive strength of the concrete $f_c = 7268\,psi$ (50.11 MPa), the modulus was estimated about $4859.4\,ksi$ (33.5 GPa), and the rapture strength of concrete was estimated about $639.4\,psi$ (4.41 MPa). According to the beam design and material properties, the cracking load of the beam was estimated about 2800 lbs, and the ultimate load was estimated about 12825 lbs. The calculations can be referred to Appendix B.5.

Same to RC beam 4, four-point-bending tests of RC beam 5 were performed in three load cycles. The load – deflection curve is shown in Figure 82. The sudden change in the slope of the load-deflection curve between 2000 lbs and 3000 lbs indicated initial cracking of the beam. And the ultimate load from the test was about 18000 lbs.

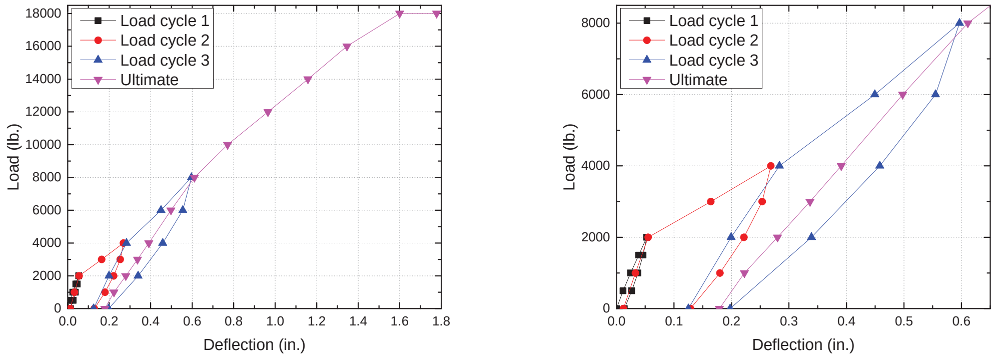

Figure 82. Load-deflection curve of RC beam 5

5.3.3 <u>Test results</u>

5.3.3.1 <u>Results from S7</u>

Distributed sensor S7 was installed on the tension surface of the beam. With the intact beam as the reference, BFS and BGSWD measured from different load cycles are shown in Figures 83-85.

(1) Load cycle 1

The BFS and BGSWD measured from load cycle 1 are shown in Figure 83. Since the load was lower than the cracking load, the beam only experienced minor damages. A few peaks were barely recognized at 0.85m, 1.05m, 1.45m and 1.55m from BFS under the load of 2000 lbs. The BGSWD was noisy and no distinct peaks were recognized.

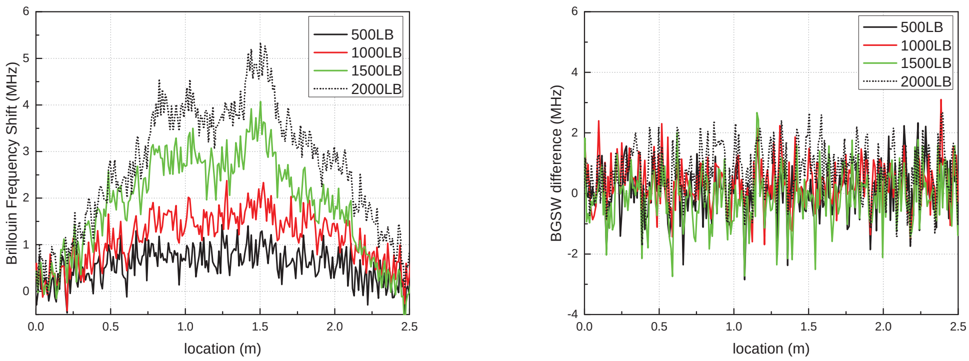

(a) BFS (b) BGSWD

Figure 83. BFS and BGSWD from S7 in load cycle 1

The displacements measured by sensors FD1 – FD6 are listed in Table XXII. The overall displacements measured by the sensors were very small, and it was unlikely that cracks developing at any of the notches in load cycle 1.

Table XXII. Displacements measured by FD1-FD6 in load cycle 1 (**unit**: **μm**)

Loads (lbs)	FD 1	FD 2	FD 3	FD 4	FD 5	FD 6
500	3.24	4.38	5.00	4.16	4.24	2.88
1000	5.66	7.94	7.65	7.61	8.73	4.84
1500	9.07	13.37	11.65	11.31	12.71	7.07
2000	12.28	22.38	18.58	18.08	19.24	11.99

(2) Load cycle 2

The BFS and BGSWD measured from load cycle 2 are show in Figure 84. No peaks were recognized from BFS when the load was increased from 0 to 2000 lbs. Major peaks were recognized at 0.85m, 1.25m, 1.55m and 1.7m from BFS under the load of 3000 lbs, and three more peaks were found at 0.5m, 1.05m and 1.85m under the load of 4000 lbs. All these peaks matched with the cracks detected from visual inspections after the load test. Similar to BFS, no major peaks were recognized from BGSWD until the load was increased to 3000 lbs, and they were at 0.85m, 1.25m 1.55m and 1.7m. More major peaks were found at 0.5m, 1.05m, 1.45m and 1.85m under the load of 4000 lbs.

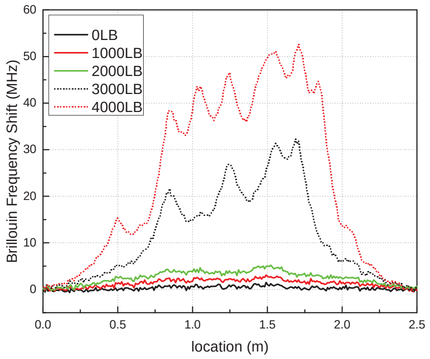

(a) BFS

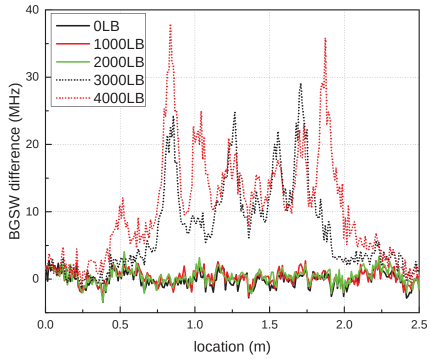

(b) BGSWD

Figure 84. BFS and BGSWD from S7 in load cycle 2

The displacements measured by sensors FD1 – FD6 are listed in Table XXIII. Displacements measured by FD 2 and FD 5 were much larger than the other sensors under the load of 3000 lbs, which indicated cracks developing at 0.85m and 1.55m. When the load was increased to 4000 lbs, results from displacement sensors indicated new cracks developing at 0.5m, 1.05m, and 1.45m.

Table XXIII. Displacements measured by FD1-FD6 in load cycle 2 (**unit**: **μm**)

Loads (lbs)	FD 1	FD 2	FD 3	FD 4	FD 5	FD 6
0	19.95	16.21	18.24	23.48	13.34	21.06
1000	24.98	23.11	22.53	29.70	21.67	24.48
2000	29.87	31.08	29.88	36.07	30.10	29.22
3000	38.33	169.62	50.31	55.75	130.21	38.09
4000	88.81	224.55	191.41	148.00	158.89	50.71

(3) Load cycle 3

The BFS and BGSWD measured in load cycle 3 are show in Figure 85. Notable residue was found from BFS before any load was applied to the beam, indicating damages accumulated in the beam in load cycle 2. Peaks were clearly recognized at 0.5m, 0.85m, 1.05m, 1.25m, 1.55m, 1.7m, and 1.85m from BFS under the load of 4000 lbs, which matched with results from load cycle 2. When the load was increased to 6000 lbs, two more peaks were found at 0.65m and 2.05m, and the peak at 1.55m shifted to 1.5m. No more peaks were found from BFS when the load was increased to 8000 lbs. Similar to BFS, residue existed in BGSWD before any load was applied to the beam, and major peaks were found at 0.5m, 0.85m, 1.05m, 1.25m, 1.7m and 1.85m under the load of 4000 lbs. When the load was increased to 6000 lbs, more peaks were clearly recognized at 0.65m, 1.45m, 1.55m and 2.05m, and the peak at 0.5m shifted to 0.45m. No more peaks were found from BGSWD under the load of 8000 lbs.

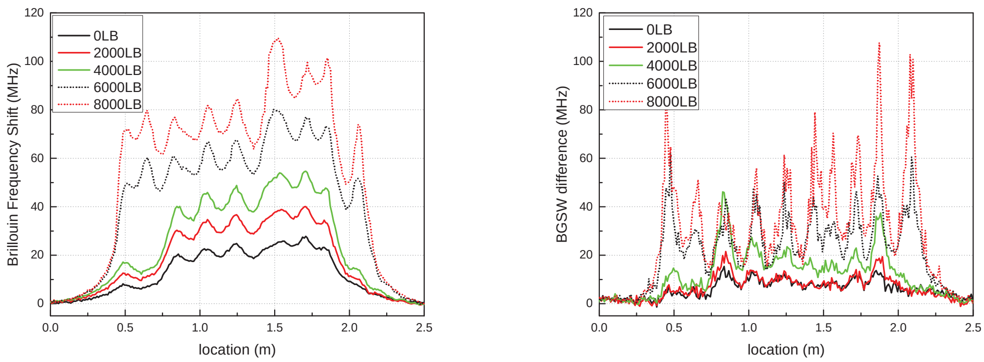

(a) BFS (b) BGSWD

Figure 85. BFS and BGSWD from S7 in load cycle 3

The displacements measured by sensors FD1 – FD6 are listed in Table XXIV. The measured displacements indicated cracks was developing at the locations of FD1 – FD5 when the load was no more than 4000 lbs. Under the load of 6000 lbs, a new crack was developing at the location of FD 6, which agreed with the results from BFS and BGSWD.

Table XXIV. Displacements measured by FD1-FD6 in load cycle 3 (**unit**: **μm**)

Loads (lbs)	FD 1	FD 2	FD 3	FD 4	FD 5	FD 6
0	44.98	118.14	94.21	67.92	67.40	16.11
2000	66.78	162.89	132.09	102.30	104.97	26.30
4000	102.74	219.34	183.39	143.37	147.06	38.75
6000	176.30	309.35	272.91	217.24	204.08	183.78
8000	273.67	412.93	374.97	291.57	267.40	256.28

(4) Results summary

Based on whether peaks were clearly recognized from BFS/BGSWD for cracks detected from visual inspections, the results from distributed sensor S7 are summarized in Table XXV. The load applied in load cycle 1 was small, and peaks were barely recognized from BFS only. Major cracking took place when the load was more than 2000 lbs in load cycle 2, and major peaks were both recognized from BFS and BGSWD. However, the crack at 1.45m was only recognized from BGSWD. When the load was more than 4000 lbs in load cycle 3, more cracks were recognized from BFS and BGSWD. For the cracks located at 1.45m and 1.55m, only one peak was shown at 1.5m from BFS, while two peaks were shown from BGSWD. In addition, the peak at 0.5m from BGSWD was affected by the large slope in strain and shifted to 0.45m.

Table XXV. Results summary for S7

crack locations (m)		0.5	0.65	0.85	1.05	1.25	1.45	1.55	1.7	1.85	2.05
load cycle 1	BFS			√	√		√	√			
	BGSWD										
load cycle 2	BFS	√		√	√	√		√	√	√	
	BGSWD	√		√	√	√	√	√	√	√	
load cycle 3	BFS	√	√	√	√	√			√	√	√
	BGSWD	√	√	√	√	√	√	√	√	√	√

5.3.3.2 <u>Results from O1 and G1</u>

(1) Load cycle 1

The BFS and BGSWD measured by O1 were shown in Figure 86. The loads were relatively small in load cycle 1, and two peaks were barely recognized at 1.05m and 1.5m from BFS under the load of 2000 lbs. No distinct peak was shown from BGSWD in load cycle 1. Similar results are found from the BFS and BGSWD measured by G1, which are shown in Figure 87. It was believed no major crack was happening in load cycle 1.

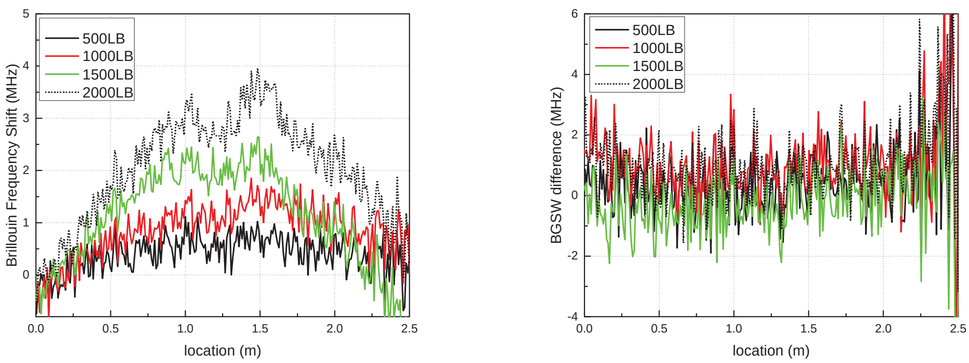

(a) BFS (b) BGSWD

Figure 86. BFS and BGSWD from O1 in load cycle 1

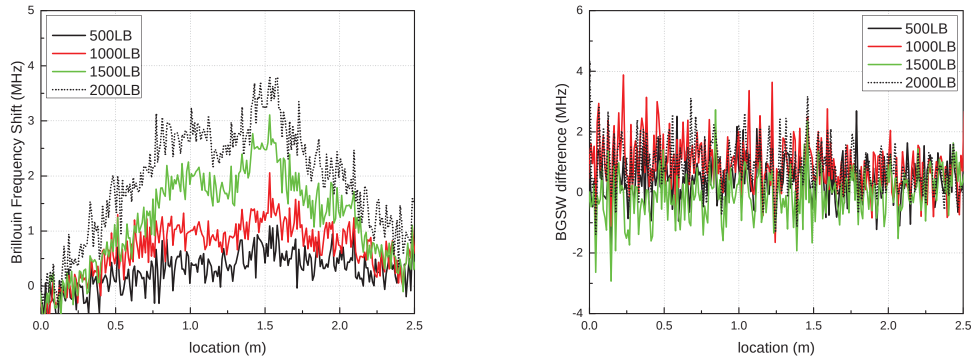

(a) BFS (b) BGSWD

Figure 87. BFS and BGSWD from G1 in load cycle 1

(2) Load cycle 2

The BFS and BGSWD measured by O1 are shown in Figure 88. Major peaks were first recognized from BFS at 0.85m, 1.25m, 1.55m and 1.7m under the load of 3000 lbs, and more peaks were found at 0.5m, 1.05m and 1.85m under the load of 4000 lbs. From BGSWD, major peaks were first recognized at 0.85m, 1.25m and 1.7m under the load 3000 of lbs, and more peaks were found at 1.05m, 1.85m and 2.05m when the load was increased to 4000 lbs.

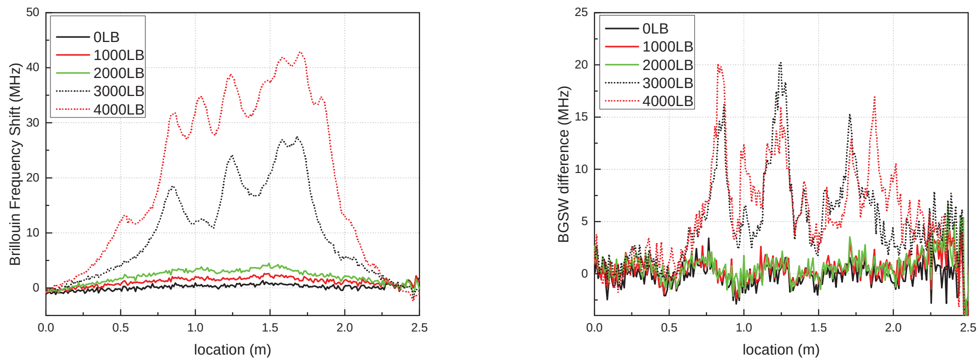

(a) BFS (b) BGSWD

Figure 88. BFS and BGSWD from O1 in load cycle 2

The BFS and BGSWD measured by G1 are shown in Figure 89. Similar to O1, major peaks were first found from BFS at 0.85m, 1.25m, 1.55m and 1.7m under the load of 3000 lbs, and more peaks were found at 0.5m, 1.05m and 1.85m under the load of 4000 lbs. Major peaks were recognized from BGSWD at 0.85m, 1.25m, 1.55m and 1.7m under the load of 3000 lbs, and more peaks were found at 1.05m and 1.85m when the load was increased to 4000 lbs.

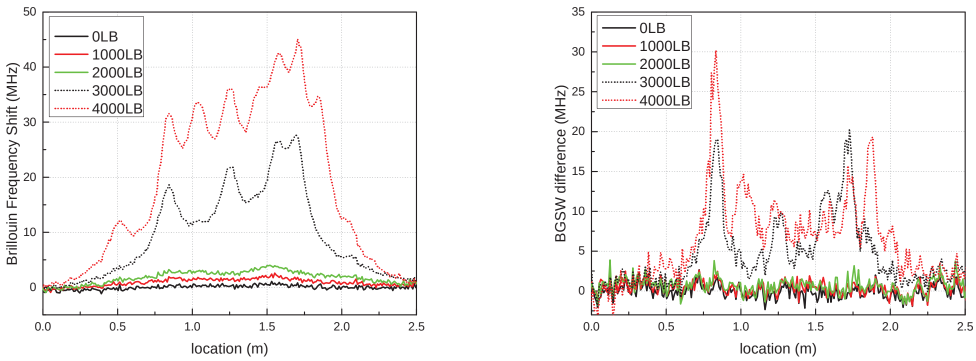

(a) BFS (b) BGSWD

Figure 89. BFS and BGSWD from G1 in load cycle 2

(3) Load cycle 3

The BFS and BGSW difference from O1 were shown in Figure 90. Residue was shown from BFS before any load was applied to the beam. Peaks were recognized at 0.5m, 0.85m, 1.05m, 1.25m, 1.55m, 1.7m and 1.85m from BFS under the load of 4000 lbs. More peaks were found at 0.65m 1.45m and 2.05m under the loads of 6000 lbs and 8000 lbs. From BGSWD, major peaks were recognized at 0.85m, 1.7m and 1.85m under the load of 4000 lbs, and more peaks were recognized at 0.5m, 0.7m, 1.2m, 2.0m and 2.1m when the load was increased to 6000 lbs and 8000 lbs.

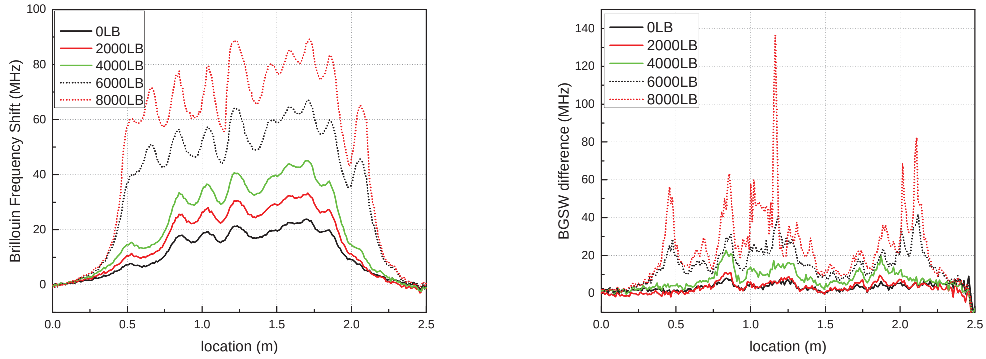

(a) BFS (b) BGSWD

Figure 90. BFS and BGSWD from O1 in load cycle 3

The BFS and BGSWD measured by G1 are shown in Figure 91. Similar to O1, residual strain existed in the sensor after load cycle 2, and major peaks were recognized at 0.5m, 0.85m, 1.05m, 1.25m, 1.55m, 1.7m and 1.85m from BFS when the load was no more than 4000 lbs. More peaks were found at 0.65m 1.45m and 2.05m when the load was increased to 6000 lbs. No more peaks were found from BFS under the load of 8000 lbs. From BGSWD, major peaks were recognized at 0.85m, 1.7m and 1.85m under the load of 4000 lbs, and more peaks were found at 0.5m, 0.7m, 1.05m, 1.25m, 1.45m, 1.55m and 2.05m when the load was increased to 6000 lbs and 8000 lbs.

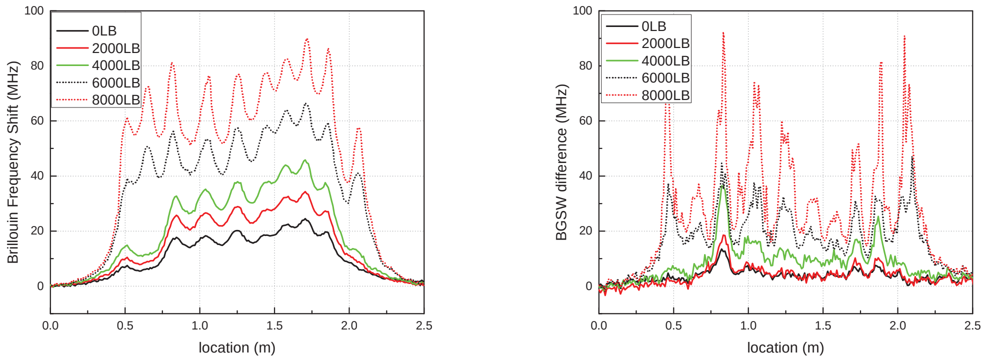

(a) BFS (b) BGSWD

Figure 91. BFS and BGSWD from G1 in load cycle 3

(4) Results summary

Based on whether cracks were recognized from BFS and BGSWD as distinct peaks, the results from sensors O1 and G1 are summarized in Tables XXVI-XXVII. Overall, the results matched with the cracks detected from visual inspections. The results measured by O1 and G1 were similar since the sensors were close to each other. Small differences existed due to different bonding conditions and surroundings. Unlike S7, O1 and G1 successfully differentiated the neighboring cracks at 1.45m and 1.55m from BFS.

Table XXVI. Results summary for O1

crack locations (m)		0.5	0.65	0.85	1.05	1.25	1.45	1.55	1.7	1.85	2.05
load cycle 1	BFS				√			√			
	BGSWD										
load cycle 2	BFS	√		√	√	√		√	√	√	
	BGSWD			√	√	√			√	√	√
load cycle 3	BFS	√	√	√	√	√	√	√	√	√	√
	BGSWD	√	√	√	√	√	√		√	√	√

Table XXVII. Results summary for G1

crack locations (m)		0.5	0.65	0.85	1.05	1.25	1.45	1.55	1.7	1.85	2.05
load cycle 1	BFS				√			√			
	BGSWD										
load cycle 2	BFS	√		√	√	√		√	√	√	
	BGSWD			√	√	√		√	√	√	
load cycle 3	BFS	√	√	√	√	√	√	√	√	√	√
	BGSWD	√	√	√	√	√	√	√	√	√	√

5.4 Summary

In this chapter, cracks on two RC beams (RC beam 4 and RC beam 5) were successfully detected and monitored by PPP-BOTDA distributed sensors with 10cm SR. The cracks were initiated by notches on the tension surfaces of the RC beams, and developing during the four-point-bending tests. A few conclusions were drawn based on the load tests of RC beams 4 and 5.

(1) BFS and BGSWD can be employed in detection and monitoring of surface-cracks for RC structures. Multiple cracks can be recognized as distinct peaks when the employed SR of PPP-BOTDA is smaller than the crack spacing, and amplitudes of the peaks are usually positively related to the CODs.

(2) BFS is better for detection of cracks in their early stages, while BGSWD is better for severe cracking problems. BGSWD only responses to large strain slopes in the sensing fiber, making it less sensitive to small CODs. When crack spacing is small, BFS

may fail in differentiating two neighboring cracks by showing only one peak between the two cracks.

(3) Similar to surface-installed distributed sensors, BFS and BGSWD measured by embedded distributed sensors can be employed to detect and monitor cracks inside the RC structures. This would help perform a comprehensive evaluation by considering results from both surface-installed sensors and embedded sensors.

(4) Large changes in the strain-slope caused by other factors would affect the performance of BGSWD in crack detection. This happened to the sensor segments near the supports in the four-point-bending tests. Peaks were shown from BGSWD in these segments as a result of fast developed strain instead of the crack-induced strain under a large load.

(5) Since BFS and BGSWD have their own advantages and disadvantages in crack detection and monitoring, it is better to perform a comprehensive evaluation by combining the findings from BFS and BGSWD.

6. CONCLUSIONS

6.1 Conclusions

Crack detection and monitoring based on PPP-BOTDA distributed sensing was systematically studied and chronologically presented in this dissertation.

Theoretical and experimental research on changes in BGS induced by a crack was introduced in chapter 2. Elastic strain analysis based on strain transfer mechanism showed that the crack would induce a piecewise exponential strain distribution in the distributed sensor. With the distributed strain as the input, numerical simulation showed that the crack can be recognized as a peak was from BFS and BGSWD. The amplitude of the peak was positively related to the COD. When an improved SR was employed, the amplitude of BFS and BGSWD would increase while the average affected lengths would decrease. The results from the single-crack test generally matched with the findings from numerical simulation, though some differences existed due to effects neglected in numerical simulation.

In chapter 3, the cracks on the steel beam were successfully recognized as two peaks from the BFS and BGSWD measured by the PPP-BOTDA distributed sensor with 20cm SR. The amplitudes of BFS and BGSWD were positively related to the CODs. However, crack detection and monitoring for RC beams 1-3 were not successful when 20cm SR was employed and most peaks from BFS and BGSWD did not match with the cracks from visual inspections.

The unsuccessful experiences from the load tests of RC beams 1-3 motivated the research on capability of PPP-BOTDA in differentiating neighboring cracks. Effects of SRs were considered for the dual-crack cases with different crack spacing. Results from numerical simulation and dual-crack tests showed that two neighboring cracks could be differentiated as two distinct peaks from BFS and BGSWD when the SR employed was smaller than the crack spacing. And the amplitudes of BFS and BGSWD were positively related to the CODs. The performance of PPP-BOTDA distributed sensing was questionable when the SR employed was larger than the crack spacing. BGSWD had a better performance in differentiating cracks with small crack spacing.

Results from the load tests of two more RC beams validated the findings from chapter 4. Multiple cracks were successfully detected from the BFS and BGSWD as distinct peaks when 10cm SR was employed. The amplitudes of BFS and BGSWD were mostly positively related to the CODs on the beams. As BFS and BGSWD have their own advantages and disadvantages, it is suggested that they could be united to improve the accuracy in crack detection and monitoring.

6.2 Future work

Even though positive results are shown in the study, there are improvements that can be achieved from future work.

When the COD is large, the fiber coating and the adhesive layer may experience plastic deformation and bond-slip between different materials may happen. As a result, different distributed strain could be induced in the sensing fiber. Under this condition, strain analysis for large CODs should be performed.

The strain transfer mechanism between the embedded distributed sensor and its surroundings could be different from the surface-installed distributed sensor, and the crack-induced strain in the embedded distributed sensor should be studied systematically.

Many aspects of numerical simulation could be improved. For example, the shape of the actual pulse should replace the step function used in the analysis. Attenuation in the fiber, signal loss brought by different components, and noises in the system could also be considered in the simulation.

The conditions in the field are usually worse than in the lab, and the effects should be considered in the research work. For example, thermal effects could be introduced to the load tests. The effects of shear forces in the structural members could also be studied.

CITED LITERATURE

1. ASCE: 2013 Report Card on America's Infrastructure – Bridges, http://www.infrastructurereportcard.org/bridges/, 2013.

2. J.M.W Brownjohn: Structural health monitoring of civil infrastructure. Phil. Trans. R. Soc. A 365: 589–622, 2007.

3. Peter C. Chang, Alison Flatau, and S. C. Liu: Review paper: health monitoring of civil infrastructure. Structural health monitoring 2(3): 257-267, 2003.

4. A. J. Cardini and John T. DeWolf: Long-term structural health monitoring of a multi-girder steel composite bridge using strain data. Structural Health Monitoring 8(1):47-58, 2008.

5. Charles R. Farrar and Keith Worden: An introduction to structural health monitoring. Philosophical Transactions of the Royal Society of London A 365: 303-315, 2007.

6. Oral Büyüköztürk and Tzu-Yang Yu: Structural health monitoring and seismic impact assessment. Proc. of the 5th National Conference on Earthquake Engineering, 2004.

7. Zhao Zhengwei, Achintya Haldar, and Florence L. Breen Jr.: Fatigue-reliability evaluation of steel bridges. Journal of Structural Engineering 120: 1608-1623, 1994.

8. I. Abdel-Qader, O. Abudayyeh, and M. Kelly: Analysis of Edge-Detection Techniques for Crack Identification in Bridges. J. Comput. Civ. Eng. 17: 255–263, 2003.

9. Tomoyuki Yamaguchi, Shingo Nakamura, Ryo Saegusa, and Shuji Hashimoto: Image-Based Crack Detection for Real Concrete Surfaces. IEEJ Transactions on Electrical and Electronic Engineering 3: 128-135, 2008.

10. Tomoyuki Yamaguchi and Shuji Hashimoto: Fast crack detection method for large-size concrete surface images using percolation-based image processing. Machine Vision and Applications 21: 797-809, 2010.

11. Yusuke Fujita, Yoshihiro Mitani, and Yoshihiko Hamamoto: A method for crack detection on a concrete structure. Proc. of 18th International Conference on Pattern Recognition 3: 901-904, 2006.

12. F. C. Sham, Nelson Chen, and Liu Long: Surface crack detection by flash thermography on concrete surface. Insight-Non-Destructive Testing and Condition Monitoring 50: 240-243, 2008.

13. Hong-Nan Li, Dong-Sheng Li, and Gang-Bing Song: Recent applications of fiber optic sensors to health monitoring in civil engineering. Engineering structures 26: 1647-1657, 2004.

14. Xianglin Gu, Zhongyu Chen, and Farhad Ansari: Embedded fiber optic crack sensor for reinforced concrete structures. ACI Structural Journal 97: 468-476, 2000.

15. P. A. Doyle and C. M. Scala: Crack depth measurement by ultrasonics: a review. Ultrasonics 16: 164-170, 1978.

16. Bao Mi, Jennifer E. Michaels, and Thomas E. Michaels: An ultrasonic method for dynamic monitoring of fatigue crack initiation and growth. The Journal of the Acoustical Society of America 119: 74-85, 2006.

17. Kyung-Young Jhang: Nonlinear ultrasonic techniques for nondestructive assessment of micro damage in material: a review. International journal of precision engineering and manufacturing 10: 123-135, 2009.

18. Nicholas J. Carino: The impact-echo method: an overview. Proceedings of the 2001 Structures Congress & Exposition, 2001.

19. Yinching Lin and M. Sansolone: Detecting flaws in concrete beams and columns using the impact-echo method. ACI Materials Journal 89: 394-405, 1992.

20. Chia-chi Cheng and Mary Sansalone: Determining the minimum crack width that can be detected using the impact-echo method Part 1: Experimental study. Materials and Structures 28: 74-82, 1995.

21. Ertugrul Cam, Sadettin Orhan, and Murat Luy: An analysis of cracked beam structure using impact echo method. NDT & E International 38: 368-373, 2005.

22. Johannes Hugenschmidt and Roman Mastrangelo: GPR inspection of concrete bridges. Cement and Concrete Composites 28: 384-392, 2006.

23. Victor Giurgiutiu and JingJing Bao: Embedded-ultrasonics structural radar for in situ structural health monitoring of thin-wall structures. Structural Health Monitoring 3: 121-140, 2004.

24. A. K. Pandey, M. Biswas, and M. M. Samman: Damage detection from changes in curvature mode shapes. Journal of sound and vibration 145: 321-332, 1991.

25. George Hearn and Rene B. Testa: Modal analysis for damage detection in structures. Journal of Structural Engineering 117: 3042-3063, 1991.

26. O. S. Salawu: Detection of structural damage through changes in frequency: a review. Engineering structures 19: 718-723, 1997.

27. Scott W. Doebling, Charles R. Farrar, and Michael B. Prime: A summary review of vibration based damage identification methods. Shock and vibration digest 30: 91-105, 1998.

28. Jerome P. Lynch and Kenneth J. Loh: A summary review of wireless sensors and sensor networks for structural health monitoring. Shock and Vibration Digest 38: 91-130, 2006.

29. Sukun Kim, Shamim Pakzad, David Culler, James Demmel, Gregory Fenves, Steven Glaser, and Martin Turon: Health monitoring of civil infrastructures using wireless sensor networks. Proc. of 6th International Symposium on Information Processing in Sensor Networks, 254-263, 2007.

30. J. M. López-Higuera, Luis Rodriguez Cobo, Antonio Quintela Incera, and Adolfo Cobo: Fiber optic sensors in structural health monitoring. Journal of Lightwave Technology 29: 587-608, 2011.

31. R. C. Tennyson, A. A. Mufti, S. Rizkalla, G. Tadros, and B. Benmokrane: Structural health monitoring of innovative bridges in Canada with fiber optic sensors. Smart materials and Structures 10: 560-573, 2001.

32. J. M. Ko and Y. Q. Ni: Technology developments in structural health monitoring of large-scale bridges. Engineering structures 27: 1715-1725, 2005.

33. K. T. V. Grattan and T. Sun: Fiber optic sensor technology: an overview. Sensors and Actuators A: Physical 82: 40-61, 2000.

34. William W. More, Gerald Meltz, and William H. Glenn: Proc. SPIE 1169, Fiber optic Bragg grating sensors VII 98-107, 1990.

35. R. Maaskant, T. Alavie, R. M. Measures, G. Tadros, S. H. Rizkalla, and A. Guha-Thakurta: Fiber-optic Bragg grating sensors for bridge monitoring. Cement and Concrete Composites 19: 21-33, 1997.

36. T. HT. Chan, Ling Yu, Hwa-Yaw Tam, Yi-Qing Ni, S. Y. Liu, W. H. Chung, and L. K. Cheng: Fiber Bragg grating sensors for structural health monitoring of Tsing Ma bridge: Background and experimental observation. Engineering structures 28: 648-659, 2006.

37. Dewei Meng and Farhad Ansari: Damped fiber optic low-frequency tiltmeter for real-time monitoring of structural displacements. Measurement Science and Technology 24: 125106, 2013.

38. Iman Talebinejad, Chad Fischer, and Farhad Ansari: Low frequency fiber optic accelerometer for civil structural health monitoring. Proc. SPIE 7294, Nondestructive Characterization for Composite Materials, Aerospace Engineering, Civil Infrastructure, and Homeland Security 729412, 2009.

39. David A. Jackson, L. Reekie, J. L. Archambault, and A. B. Lobo Ribeiro: Simple multiplexing scheme for a fiber-optic grating sensor network. Optics Letters 18: 1192-1194, 1993.

40. John S. Selker, Luc Thevenaz, Hendrik Huwald, Alfred Mallet, Wim Luxemburg, Nick Van De Giesen, Martin Stejskal, Josef Zeman, Martijn Westhoff, and Marc B. Parlange: Distributed fiber-optic temperature sensing for hydrologic systems. Water Resources Research 42: W12202, 2006.

41. Libo Yuan and Farhad Ansari: White-light interferometric fiber-optic distributed strain-sensing system. Sensors and Actuators A: Physical 63: 177-181, 1997.

42. Hideaki Murayama, Kazuro Kageyama, Hiroshi Naruse, Akiyoshi Shimada, and Kiyoshi Uzawa: Application of fiber-optic distributed sensors to health monitoring for full-scale composite structures. Journal of Intelligent Material Systems and Structures 14: 3-13, 2003.

43. Juan C. Juarez, Eric W. Maier, Kyoo Nam Choi, and Henry F. Taylor: Distributed fiber-optic intrusion sensor system. Journal of lightwave technology 23: 2081-, 2005.

44. A. A. Boiarski, G. Pilate, T. Fink, and N.Nilsson: Temperature measurements in power plant equipment using distributed fiber optic sensing. IEEE Trans. Power Delivery 10: 1771-1778, 1995.

45. Mark Froggatt and Jason Moore: High-spatial-resolution distributed strain measurement in optical fiber with Rayleigh scatter. Applied Optics 37: 1735-1740, 1998.

46. Sascha Liehr, Philipp Lenke, Mario Wendt, Katerina Krebber, Monika Seeger, Elke Thiele, Heike Metschies, Berhane Gebreselassie, and Johannes Christian Münich: Polymer optical fiber sensors for distributed strain measurement and application in structural health monitoring. IEEE Sensors Journal 9: 1330-1338, 2009.

47. R. Posey, G. A. Johnson, and S. T. Vohra: Strain sensing based on coherent Rayleigh scattering in an optical fibre. Electronics Letters 36: 1688-1689, 2000.

48. Yuelan Lu, Tao Zhu, Liang Chen, and Xiaoyi Bao: Distributed vibration sensor based on coherent detection of phase-OTDR. Journal of Lightwave Technology 28: 3243-3249, 2010.

49. Mostafa Ahangrani Farahani and Torsten Gogolla: Spontaneous Raman scattering in optical fibers with modulated probe light for distributed temperature Raman remote sensing. Journal of Lightwave Technology 17: 1379-, 1999.

50. J. P. Dakin, D. J. Pratt, G. W. Bibby, and J. N. Ross: Distributed optical fibre Raman temperature sensor using a semiconductor light source and detector. Electronics Letters 21: 569-570, 1985.

51. Scott W. Tyler, John S. Selker, Mark B. Hausner, Christine E. Hatch, Thomas Torgersen, Carl E. Thodal, and S. Geoffrey Schladow: Environmental temperature sensing using Raman spectra DTS fiber-optic methods. Water Resources Research 45: W00D23, 2009.

52. Jonghan Park, Gabriele Bolognini, Duckey Lee, Pilhan Kim, Pilki Cho, Fabrizio Di Pasquale, and Namkyoo Park: Raman-based distributed temperature sensor with simplex coding and link optimization. IEEE Photonics Technology Letters 18: 1879-1881, 2006.

53. Tsuneo Horiguchi, Toshio Kurashima, and Mitsuhiro Tateda: Tensile strain dependence of Brillouin frequency shift in silica optical fibers. IEEE Photonics Technology Letters 1: 107-108, 1989.

54. T.R.Parker, M.Farhadiroushan, V.A.Handerek, and A.J.Rogers: Temperature and strain dependence of the power level and frequency of spontaneous Brillouin scattering in optical fibers. Optics Letters 22: 787-789, 1997.

55. Toshio Kurashima, Tsuneo Horiguchi, and Mitsuhiro Tateda: Distributed-temperature sensing using stimulated Brillouin scattering in optical silica fibers. Optics Letters 15: 1038-1040, 1990.

56. Marc Nikles, Luc Thévenaz, and Philippe A. Robert: Simple distributed fiber sensor based on Brillouin gain spectrum analysis. Optics letters 21: 758-760, 1996.

57. Jun-ich Kosugi and Yasunari Takagi: Brillouin scattering in otpical fibers. Jpn. J. Appl. Phys. 38: 3069-3071, 1999.

58. T. Horiguchi, K.shimizu, T. Kurashima, M.Tateda and Y.Koyamada: Development of a distributed sensing technique using Brillouin scattering. J. Lightwave Tech. 13: 1296-1302, 1995.

59. M. Hosein Motamedi, Xin Feng, Xiaotan Zhang, Changsen Sun, and Farhad Ansari: Quantitative investigation in distributed sensing of structural defects with Brillouin optical time domain reflectometry. Journal of Intelligent Material Systems and Structures 24: 1187-1196, 2013.

60. Andrey Kobyakov, Michael Sauer, and Dipak Chowdhury: Stimulated Brillouin scattering in optical fibers. Advances in optics and photonics 2: 1-59, 2010.

61. T. R. Parker, M. Farhadiroushan, V. A. Handerek, and A. J. Roger: A fully distributed simultaneous strain and temperature sensor using spontaneous Brillouin backscatter. IEEE Photonics Technology Letters 9: 979-981, 1997.

62. ROBERT W. Tkach, ANDREW R. Chraplyvy, and R. M. Derosier: Spontaneous Brillouin scattering for single-mode optical-fibre characterization. Electronics Letters 22: 1011-1013, 1986.

63. Hiroshige Ohno, Hiroshi Naruse, Mitsuru Kihara, and Akiyoshi Shimada: Industrial applications of the BOTDR optical fiber strain sensor. Optical fiber technology 7: 45-64, 2001.

64. Toshio Kurashima, Tsuneo Horiguchi, Hisashi Izumita, Shin-ichi Furukawa, and Yahei Koyamada: Brillouin optical-fiber time domain reflectometry. IEICE transactions on communications 76: 382-390, 1993.

65. E. P. Ippen and R. H. Stolen: Stimulated Brillouin scattering in optical fibers. Applied Physics Letters 21: 539-541, 1972.

66. Xiaoling Wang, Farhad Ansari, Dewei Meng, and Tengfei Bao: Acousto-opto-mechanical theory for polarization maintaining optical fibers in Brillouin based sensing. Optical Fiber Technology 21: 170-175, 2015.

67. V. Sundar and R.E.Newnham: Elecrostriction. In: The electrical engineering handbook, eds. R.C. Dorf, pp. 1193-1200, CRC Press, 1997.

68. D. Cotter: Stimulated Brillouin scattering in monomode optical fiber. Journal of Optical Communications 4: 10-19, 1983.

69. Robert W. Boyd, Kazimierz Rzaewski and Paul Narum: Noise initiation of stimulated Brillouin scattering. Phys. Rev. A 42: 5514-5521, 1990.

70. Kazuyuki Shiraki, Masaharu Ohashi and Mitsuhiro Tateda: SBS threshold of a fiber with a Brillouin frequency shift distribution. Journal of lightwave technology 14: 50-57, 1996.

71. Marcelo A. Soto, Gabriele Bolognini, Fabrizio Di Pasquale, and Luc Thévenaz: Simplex-coded BOTDA fiber sensor with 1 m spatial resolution over a 50 km range. Optics letters 35: 259-261, 2010.

72. Kwang-Yong Song, Zuyuan He, and Kazuo Hotate: Distributed Strain Measurement with Millimeter-Order Spatial Resolution Based on Brillouin Optical Correlation Domain Analysis and Beat Lock-in Detection Scheme. Proc. OSA Optical Fiber Sensors, paper ThC2, 2006.

73. K. Kishida and C.H.Li: Pulse pre-pump-BOTDA technology for new generation of distributed strain measuring system. Proc. of the second international conference on Structural health monitoring of intelligent infrastructure pp. 471-477, 2005.

74. Kinzo Kishida, Che-Hien Li and Kenichi Nishiguchi: Pulse pre-pump method for cm-order spatial resolution of BOTDA, Proc. SPIE 5855, 17th international conference on optical fiber sensors pp.559, 2005.

75. C. H. Li, N. Kenichi, and M. Miyuki: PPP-BOTDA method to achieve 2cm spatial resolution in Brillouin distributed measuring technique. Technical Report of IEICE 32: 55-60, 2008.

76. Che-Hien Li, T. Tsuda, and K. Kishida: PPP-BOTDA method to achieve cm-order spatial resolution in Brillouin distributed measuring technique. Technical Report of IEICE 16: 1-6, 2005.

77. Hao Liang, Wenhai Li, Nicolas Linze, Liang Chen, and Xiaoyi Bao: High-resolution DPP-BOTDA over 50 km LEAF using return-to-zero coded pulses. Optics letters 35: 1503-1505, 2010.

78. Wenhua Li, Xiaoyi Bao, Yun Li and Liang Chen: Differential pulse-width pair BOTDA for high spatial resolution sensing. Optical Express 16: 21616-21625, 2008.

79. Yongkang Dong, Xiaoyi Bao, and Wenhai Li: Differential Brillouin gain for improving the temperature accuracy and spatial resolution in a long-distance distributed fiber sensor. Applied optics 48: 4297-4301, 2009.

80. Yongkang Dong , Hongying Zhang, Liang Chen, and Xiaoyi Bao: 2 cm spatial-resolution and 2 km range Brillouin optical fiber sensor using a transient differential pulse pair. Applied optics 51: 1229-1235, 2012.

81. T. Horiguchi and M. Tateda: Optical-fiber-attenuation investigation using stimulated Brillouin scattering between a pulse and a continuous wave. Opt. Lett. 14: 408-410, 1989.

82. Dario Alsia, Miguel Gonzalez Herraez, Laura Abrardi, Sonia Martin Lopez, and Luc Thevenaz: Detrimental effect of modulation instability on distributed optical fiber sensors using stimulated Brillouin scattering. Proc. SPIE 5855, 17th international conference on optical fiber sensors pp. 587, 2005.

83. F.T. Arecchi and E.O. Schulz-Dubois: Laser Handbook 2: 1077-1150, North-Holland, 1972.

84. Tsuneo Horiguchi, Kaoru Shimizu, Toshio Kurashima, Mitsuhiro Tateda, and Yahei Koyamada: Development of a distributed sensing technique using brillouin scattering: Optical fiber sensors. Journal of lightwave technology 13: 1296-1302, 1995.

85. K. Hotate and T. Hasegawa: Measurement of Brillouin gain spectrum distribution along an optical fiber using a correlation based technique – proposal, experiment and simulation. IEICE transactions on electronics E83-C(3): 405-412, 2000.

86. Xiaoyi Bao and Liang Chen: Recent progress in Brillouin scattering based fiber sensors. Sensors 11: 4152-4187, 2011.

87. Hiroshi Naruse and Mitsuhiro Tateda: Trade-off between the spatial and the frequency resolutions in measuring the power spectrum of the Brillouin backscattered light in an optical fiber. Applied Optics 38: 6516-6521, 1999.

88. Afshar V. Shahraam, Graham A. Ferrier, Xiaoyi Bao, and Liang Chen: Effect of the finite extinction ratio of an electro-optic modulator on the performance of distributed probe-pump Brillouin sensor system. Optics Letters 28: 1418-1420, 2013.

89. K.Y. Song and K. Hotate: Distributed fiber strain sensor with 1kHz sampling rate based on Brillouin optical correlation domain analysis. IEEE Photonic. Technology Letters 19: 1928-1930, 2007.

90. K. Nishiguchi and K. Kishida: Perturbation analysis of stimulated Brillouin Scattering in an optical fiber with a finite extinction ratio. Technical Report of IEICE 14: 9-14, 2004.

91. Fabien Ravet, Fabien Briffod, Branko Glisic, Marc Nikles, and Daniele Inaudi: Submillimeter crack detection with Brillouin-based fiber-optic sensors. IEEE Sensors Journal 9: 1391-1396, 2009.

92. Branko Glisic and Daniele Inaudi: Development of method for in-service crack detection based on distributed fiber optic sensors. Structural Health Monitoring 1475921711414233, 2011.

93. Lufan Zou and Maria Q. Feng: Detection of micrometer crack by Brillouin-scattering-based distributed strain and temperature sensor. Prof. 19th International Conference on Optical Fibre Sensors pp. 700419-700419, 2008.

94. Michio Imai, Ryouji Nakano, Tetsutya Kono, Toshimichi Ichinomiya, Satoru Miura, and Masahito Mure: Crack detection application for fiber reinforced concrete using BOCDA-based optical fiber strain sensor. Journal of structural engineering 136: 1001-1008, 2010.

95. A. Deif, B. Martín-Pérez, B. Cousin, C. Zhang, X. Bao, and W. Li: Detection of cracks in a reinforced concrete beam using distributed Brillouin fibre sensors. Smart Materials and Structures 19: 055014, 2010.

96. H. Zhang and Z. S. Wu: Performance evaluation of BOTDR-based distributed fiber optic sensors for crack monitoring. Structural Health Monitoring 1475921708089745, 2008.

97. Hao Zhang and Zhishen Wu: Performance evaluation of PPP-BOTDA-based distributed optical fiber sensors. International Journal of Distributed Sensor Networks 414692, 2012.

98. Tong Guo, AiQun Li, YongSheng Song, Biao Zhang, Yang Liu, and NingSheng Yu: Experimental study on strain and deformation monitoring of reinforced concrete structures using PPP-BOTDA. Science in China Series E: Technological Sciences 52: 2859-2868, 2009.

99. Yi Bao, Weina Meng, Yizheng Chen, Genda Chen, and Kamal Henry Khayat: Measuring mortar shrinkage and cracking by pulse pre-pump Brillouin optical time domain analysis with a single optical fiber. Materials Letters 145: 344-346, 2015.

100. Zhi Zhou, Jilong Li, and Jinping Ou: Interface strain transfer mechanism and error modification of embedded FBG strain sensors. Journal of Harbin Institute of Technology 1: 49-55, 2006.

101. Farhad Ansari and Yuan Libo: Mechanics of bond and interface shear transfer in optical fiber sensors. Journal of Engineering Mechanics 124: 385-394, 1998.

102. Kaitai Wan, Christopher K. Y. Leung, and Noah G Olson: Investigation of the strain transfer for surface-attached optical fiber strain sensors. Smart materials and structures 17: 035037, 2008.

103. Xin Feng, Jing Zhou, Changsen Sun, Xiaotan Zhang, and Farhad Ansari: Theoretical and experimental investigations into crack detection with BOTDR-Distributed Fiber Optic Sensors. Journal of Engineering Mechanics 139: 1797-1807, 2013.

104. Michio Imai and Maria Feng: Sensing optical fiber installation study for crack indetification using a stimulated Brillouin-based strain sensor. Journal of Structural Health Monitoring 11: 501-509, 2012.

105. Dewei Meng, Farhad Anasri and Xin Feng: Detection and monitoring of surface micro-cracks by PPP-BOTDA. Applied Optics 54: 4972-4978, 2015.

106. N.G. Olson, C. Leung and X. Wang: Stiffness measurement of the external polymeric coating on an optical fiber. Experimental Techniques 26: 51–56, 2002.

107. Hiroshi Naruse, Mitsuhiro Tateda, Hiroshige Ohno, and Akiyoshi Shimada: Dependence of the Brillouin gain spectrum on linear strain distribution for optical time-domain reflectometer-type strain sensors. Applied Optics 41: 7212-7217, 2002.

108. http://www.neubrex.com/htm/products/pro-nbx6000_1-55.htm

109. S.Timoshenko: History of strength of materials, McGraw-Hill, New York, 1953.

110. Building Code Requirements for Structural Concrete (ACI 318-08) Published by American Concrete Institue, 2008.

111. Valerie Illingworth: The Penguin Dictionary of Physics, Penguin Books, London, 1991.

APPENDICES

Appendix A. Source code for numerical simulation

A.1 Main function (integral3)

```
function integral3 (SR,Rx,omega1,omega2 )
% omega1 and omega2 in MHZ, omega for free fiber is 0; Rx in dB;
vg=200000000;       %light speed in fiber
omeganum=(omega2-omega1)+1;        % range of sweeping frequency; frequency step
1mhz
rxnum=10^(Rx/20);      % Rx in decimal


if SR==5   % pulse function for different SR;
   D=0.0000000005;
   Dpre=0.0000000135;
   cp=1;    %normalized power for continuous wave;
   ap=rxnum-1;
elseif SR==10
       D=0.000000001;
       Dpre=0.000000015;
       cp=1;
       ap=rxnum-1;
elseif SR==20
           D=0.000000002;
           Dpre=0.000000015;
           cp=1;
```

Appendix A (Continued)

```
        ap=rxnum-1;
elseif SR==50
          D=0.000000005;
          %Dpre=0.000000013;
          Dpre=0.000000018;
          cp=1;
          ap=rxnum-1;
elseif SR==100
            D=0.000000010;
            Dpre=0.000000022;
            cp=1;
            ap=rxnum-1;
else
            print('wrong spatial resolution')
            return;
end


for m=1:201
  t(m)=0.0000000001*(m-1)+Dpre-D;   % 1cm readout resolution on a 2m long
segment;
end
for n=1:omeganum
```

Appendix A (Continued)

```
        omega(n)=omega1+(n-1);    % sweeping frequency step 1MHz
end
tlength=length(t);
H=zeros(tlength,omeganum);  % initialize SBS to zero;
H1=zeros(tlength,omeganum);
H2=zeros(tlength,omeganum);
H3=zeros(tlength,omeganum);
H4=zeros(tlength,omeganum);
crack1=[0,25,50,100,150,200];    % COD of crack 1;
crack2=[0,25,50,100,150,200];    % COD of crack 2, set to zero for single-crack case;
for nn1=1:6
  n1=crack1(nn1);
  for nn2=1:6
    n2=crack2(nn2);
for m=1:tlength
  for n=1:omeganum

[H(m,n),H1(m,n),H2(m,n),H3(m,n),H4(m,n)]=integral2(omega(n),cp,ap,Dpre,D,t(m),vg,
n1,n2);
        Hre(m,n)=real(H(m,n));
        H1re(m,n)=real(H1(m,n));
        H2re(m,n)=real(H2(m,n));
```

Appendix A (Continued)

```
            H3re(m,n)=real(H3(m,n));
            H4re(m,n)=real(H4(m,n));
    end
end

for m=1:tlength
x1(m)=m*0.01;
p(m)=max(Hre(m,:));   % find the peak power of BGS at each readout location;
    q(m)=0;
     for n=1:omeganum
         if Hre(m,n)<p(m)
             n=n+1;
         else
             q(m)=n;    % find out frequency shift of the peak power at each readout location;
             break;
         end
     end
     for fr=1:51
         polyx(fr)=q(m)-26+fr;
         polyy(fr)=Hre(m,q(m)-26+fr);
     end
     factor=polyfit(polyx,polyy,2);
```

Appendix A (Continued)

```
    cf=-0.5*factor(2)/factor(1);
    cfq(m)=omega1+(cf-1);   % frequency step 1MHz   % parabolic fitting of raw data for
BFS;
    cfpower(m)=factor(3)-0.25*factor(2)*factor(2)/factor(1);    % parabolic fitting of raw
data for peak power;
    Hb(m)=0.8*cfpower(m);      %1dB drop from peak power;


    bgswidth=zeros(tlength);    %initialize BGSWD at each readout location;
    bgswidth(m)=-sqrt(factor(2)*factor(2)-4*factor(1)*(factor(3)-Hb(m)))/factor(1);   %
BGSWD from parabolic fitting;
end


% output SBS in figures at a given location.
x=omega;
y1=10*log(H1re(111,:))/log(10);
y2=10*log(H2re(111,:))/log(10);
y3=10*log(H3re(111,:))/log(10);
y4=10*log(H4re(111,:))/log(10);
y=10*log(Hre(111,:))/log(10);
figure(1);
xlabel('frequency (MHz)')
ylabel('H1')
```

Appendix A (Continued)

```
plot(x,y1);

figure(2);

xlabel('frequency (MHz)')

ylabel('H2')

plot(x,y2);

figure(3);

xlabel('frequency (MHz)');

ylabel('H3')

plot(x,y3);

figure(4);

xlabel('frequency (MHz)')

ylabel('H4')

plot(x,y4);

figure(5);

xlabel('frequency (MHz)')

ylabel('H')

plot(x,y);


% output of BFS, BGSWD and peak power along the distributed sensor;

figure(6);

plot(x1,cfq);

figure(7);
```

Appendix A (Continued)

```
plot(x1,bgswidth);
figure(8);
plot(x1,cfpower);


end
end
end
```

A.2 function integral2

```
function [h,h1,h2,h3,h4] = integral2(omega_2,cp,ap,Dpre,D,t2,vg,n1,n2)
gamma=15000000;
h1=0;
h2=0;
h3=0;
h4=0;
omegas=omega_2*6280000;
integrals1=zeros(1,100);
integrals2=zeros(1,100);
integrals4=zeros(1,100);
z2=zeros(1,100);
z3=zeros(1,100);
for k=1:100  % divide D by 100; divide Dpre by 100
```

Appendix A (Continued)

```
    z2(k)=vg*(t2-Dpre+D/100*(k-0.5))/2;
    integrals1(k)=gamma/(gamma+i*(bcf(z2(k),n1,n2)-omegas))*(1-exp(-
(gamma+i*(bcf(z2(k),n1,n2)-omegas))*(t2-Dpre+D-2*z2(k)/vg)));
    h1=h1+ap*ap*integrals1(k)*D*vg/200;  % solve for SBS term H1;
    integrals2(k)=gamma/(gamma+i*(bcf(z2(k),n1,n2)-omegas))*(1-exp(-
(gamma+i*(bcf(z2(k),n1,n2)-omegas))*(t2-2*z2(k)/vg)));
    h2=h2+ap*cp*integrals2(k)*D*vg/200; %solve for SBS term H2;
    h3=h3+ap*cp*integrals1(k)*D*vg/200;  %solve for SBS term H3;
    z3(k)=vg*(t2-Dpre+Dpre/100*(k-0.5))/2;
    integrals4(k)=gamma/(gamma+i*(bcf(z3(k),n1,n2)-omegas))*(1-exp(-
(gamma+i*(bcf(z3(k),n1,n2)-omegas))*(t2-2*z3(k)/vg)));
    h4=h4+cp*cp*integrals4(k)*Dpre*vg/200;   % solve for SBS term H4;
    h=h1+h2+h3+h4;  %solve for SBS term H;
end
end
```

A.3 <u>function bcf</u>

```
function bcfvalue = bcf( location,n1,n2 )  % BFS converted from input strain;
%strainvalue is in microstrain
%form strain here:
%if location...
%strainvalue=...;
```

Appendix A (Continued)

```
% example input for two-crack case with 50cm spacing and beta=40;
if location-0.75<0==1
   bcfvalue=(0.5*n1*40*exp(-40*(0.75-location))+0.5*n2*40*exp(-40*(1.25-
location)))*0.05*6280000;
elseif location-1.25<0==1
   bcfvalue=(0.5*n1*40*exp(-40*(location-0.75))+0.5*n2*40*exp(-40*(1.25-
location)))*0.05*6280000;
else
   bcfvalue=(0.5*n1*40*exp(-40*(location-0.75))+0.5*n2*40*exp(-40*(location-
1.25)))*0.05*6280000;
end
```

Appendix B. Estimation of cracking and ultimate loads of RC beams

Example: RC beam 1

According to ACI318-08 8.5.1, modulus of elasticity is given by Equation B.1

$$\mathrm{E_c} = 57000\sqrt{\mathrm{f_c}} = 4367.1 \text{ ksi (30.11 GPa)} \tag{B.1}$$

According to ACI318-08 9.5.2.3, rapture strength of concrete is estimated according to Equation B.2

$$\mathrm{f_r} = 7.5\sqrt{\mathrm{f_c}} = 574.6 \text{ psi (3.96 MPa)} \tag{B.2}$$

The cracking strain for concrete is estimated as

$$\varepsilon_\mathrm{t} = \frac{\mathrm{f_r}}{\mathrm{E_c}} = 131.5\mu\varepsilon \tag{B.3}$$

7% loss of cross section area is considered for main reinforcement due to surface grinding for sensor installation.

The area of reinforcement for tension (2 No.4 rebar) is

$$A_s = 2 * 0.2 * (1 - 0.07) = 0.372\ in^2\ (240mm^2) \tag{B.4}$$

The area of reinforcement for compression (2 No.3 rebar) is

$$A_s{}' = 2 * 0.11 * (1 - 0.07) = 0.2046\ in^2\ (132mm^2) \tag{B.5}$$

According to ACI318-08 8.5.2, $E_s = 200GPa$.

The gross area of the cross section is

$$A = bh + (n - 1)(\mathrm{A_s} + \mathrm{A_s'}) = 35956\ mm^2 \tag{B.6}$$

where $n = \frac{\mathrm{E_s}}{\mathrm{E_c}}$.

The moment of area is

$$W = \frac{1}{2}bh^2 + (n - 1)(\mathrm{A_s}h_s + \mathrm{A_s'}h_s{}') = 3997012\ mm^3 \tag{B.7}$$

Appendix B (Continued)

And the height of neutral axis is

$$h_{na} = \frac{W}{A} = 111.16\ mm \tag{B.8}$$

Based on h_{na} and ε_t, the cracking moment is estimated as:

$$M_{cr} = \frac{1}{3}\mathrm{bf_t}h_{na}{}^{2} + \mathrm{A_s}(\mathrm{n}-1)\mathrm{E_c}\left(1-\frac{h_s}{h_{na}}\right)\varepsilon_t(h_{na}-h_s) + \frac{1}{3}b\mathrm{f_t}\left(\frac{\mathrm{h}}{h_{na}}-1\right)(\mathrm{h}-h_{na})^2 +$$

$$\mathrm{A}_s'(\mathrm{n}-1)\mathrm{E_c}\left(\frac{h_s'}{h_{na}}-1\right)\varepsilon_t(h_s'-h_{na}) = 5301.6Nm \tag{B.9}$$

Considering the dead load of the RC beam is about $q = 0.82KN/m$, the bending moment at mid span due to the dead load is

$$M_{1.25} = \frac{1}{8}ql^2 = 0.64KNm \tag{B.10}$$

And the cracking load P_{cr} is

$$P_{cr} = 2 * \frac{(M_{cr}-M_{1.25})}{0.75} = 12430N = 2793\ lbs \tag{B.11}$$

The yield stress of the reinforcement is $f_y = 60\ kips\ (413.7MPa)$. The ultimate bending moment of the beam is calculated by equation

$$M_u = A_s f_y\left(d-\frac{x}{2}\right) = 21270Nm \tag{B.12}$$

where

$$x = \frac{A_s f_y}{\beta\ f_c b} = 21.5mm \tag{B.13}$$

and

$$\beta = 0.85 - \frac{f_c-28}{7} * 0.05 = 0.761 \tag{B.14}$$

The ultimate load of beam is

$$P = \frac{2M_u}{0.75} = 57\ KN\ \text{(12810lb)} \tag{B.15}$$

Appendix B (Continued)

The calculation of cracking load and ultimate load for RC beams 2-5 can followed the same procedure.

Appendix C. Copyright permission from OSA

Dear Dewei Meng,

Thank you for contacting The Optical Society.

Because you are the author of the source paper from which you wish to reproduce material, OSA considers your requested use of its copyrighted materials to be permissible within the author rights granted in the Copyright Transfer Agreement submitted by the requester on acceptance for publication of his/her manuscript. It is requested that a complete citation of the original material be included in any publication. This permission assumes that the material was not reproduced from another source when published in the original publication. Please let me know if you have any questions.

Kind Regards,

Susannah Lehman

Susannah Lehman

November 18, 2015

Authorized Agent, The Optical Society

VITA

NAME: Dewei Meng

EDUCATION: Ph.D. Civil Engineering
University of Illinois at Chicago. December 2015

M.Sc. Bridge Engineering
Tongji University, Shanghai, China. May 2010

B.Sc, Civil Engineering
Tongji University, Shanghai, China. June 2007

TEACHING: University of Illinois at Chicago
Teaching Assistant
2012 and 2015

PROFESSIONAL: University of Illinois at Chicago
Research Assistant
2010 to 2015

Tongji University, Shanghai, China
Research Assistant
2007-2010

HORNORS: 2014 Christopher B. and Susan S. Burke Graduate Student Award

MEMEBERSHIP: Student member of ASCE and ISHMII

PUBLICATIONS: Dewei Meng, Farhad Ansari and Xin Feng. Detection and monitoring of surface micro-cracks by PPP-BOTDA. Applied Optics. 54(16), 2015, pp.4972-4978.

Xiaoling Wang, Farhad Ansari, Dewei Meng and Tengfei Bao. Acousto-opto-mechanical theory for polarization maintaining optical fibers in Brillouin based sensing. Journal of Optical Fiber Technology. 2015, 21, pp.170-175.
Dewei Meng and Farhad Ansari. Damped fiber optic low-frequency tiltmeter for real-time monitoring of structural displacements. Measurement science and technology. Institute of Physics (IOP), 2013 24(12)

Dewei Meng and Junjie Wang. Study on Simplified Formulae for

Impact Force-indentation Relationship under Frontal Impact of Ship-bow to Rigid Wall. Journal of disaster prevention and mitigation engineering. 2011 31(2), Shanghai, China.

Dewei Meng, Junjie Wang and Lingtao Bu. Simplified dynamic analysis method of ship bridge collision: precision of simplified models. Journal of computer aided engineering. 2011 20(1), Shanghai, China.

Junjie Wang, Lingtao Bu and Dewei Meng. Simplified dynamic analysis method of ship-bridge collision: simplified models. Journal of computer aided engineering. 2011 20(1), Shanghai, China.

Junjie Wang, Dewei Meng and Bifeng Ou. Basic Impact Loading Models of Head Bow-on Collision Between a Ship and Rigid Wall. Journal of Vibration and Shock. 2010 29(11), Shanghai, China.